Measurement of Electron-Positron Asymmetry in W Decays from 1.8 TeV Proton-Antiproton Collisions

January 1992

Satoru Ogawa

Submitted in partial fulfillment of the requirements for
the Degree of Doctor of Science in
the Doctoral Program in
University of Tsukuba

Abstract

The charge asymmetry in the electron pseudo-rapidity distribution of W-boson decays was measured in 1.8-TeV proton-antiproton collisions. The lepton charge asymmetry is expected as a combined result of the V–A left-handed coupling and the proton structure. A measurement of the lepton charge asymmetry in the lepton pseudo-rapidity distributions allows us to probe the proton structure in the region of small x ($0.01 < x < 0.2$) and large Q^2 ($\sim M_W^2$). Structure functions were tested assuming the V–A coupling in W production. We found MRSB and EHLQ sets of structure function were preferable whereas DO set of structure function was ruled out at a confidence level of 90%.

Acknowledgements

My great thanks to my advisor, Koji Takikawa, for continuous encouragement during my graduate student career, for sharing his insights and for an apparently inexhaustible supply of good will. Kunitaka Kondo gave me the opportunity to collaborate with CDF. Henry Frisch suggested the topic of this thesis to me. Jay Hauser provided guidance at critical points in the analysis, encouraged me through the analysis. Claudio Campagnari, Bob Wagner, and Christo Wendt helped thinking through several subtle points in the interpretation of the data. Peter Berge, Aseet Muckerjee offered an enthusiastic help to continue the analysis. Discussions on physics with Luc Demortier, Shinghong Kim, Toshihiro Mimashi, Shigeyuki Miyashita, Itsuo Nakano, Yoshihiro Seiya, Mikio Takano, Fumihiko Ukegawa proved beneficial. Yasuo Fukui, Takashi Ino, Shunichi Kanda, Masanori Mishina, Youhei Morita, Mariko Ninomiya support my detector work. Conversations with Yoshimi Funayama, Shuichi Kunori, Shoji Mikamo, Nobuaki Oshima, Taiji Yamanouchi, Ryuji Yamada are forgettable during my stay at Fermilab. I also wish to thank to other members of the Tsukuba high energy physics group, Fumio Abe, Hiroshi Iso, Hara Kazuhiko, Kiyoshi Yasuoka, Masahiko Yokoyama and other colleagues for their constant help. The great success of the CDF experiment is a result of patient and continuous work of the CDF collaboration. In addition, there are those who built the detector, and those who built and operated the accelerator, ... It would be quite impossible to try and acknowledge in its entirety. This thesis would obviously not have been possible without everyone of them. I also wish to express appreciation to Carol Picciolo, Kyoko Kunori, Kazuko Kumashiro, Mutsumi Uenishi for their constant supports through their secretary works. Finally I would like to thank my family for their constant supports and encouragement.

This work was supported by the Ministry of Science, Culture, and Education of Japan, the U.S. Department of Energy, the U.S. National Science Foundation, the A. P. Sloan Foundation, the Instituto Nazionale di Fisica Nucleare.

The CDF Collaboration

F. Abe,[9] D. Amidei,[4] G. Apollinari,[16] M. Atac,[4] P. Auchincloss,[15] A. R. Baden,[6] N. Bacchetta,[11] M. W. Bailey,[14] A. Bamberger,[4,a] P. de Barbaro,[15] B. A. Barnett,[8] A. Barbaro-Galtieri,[10] V. E. Barnes,[14] T. Baumann,[6] F. Bedeschi,[13] S. Behrends,[2] S. Belforte,[13] G. Bellettini,[13] J. Bellinger,[21] D. Benjamin,[20] J. Bensinger,[2] A. Beretvas,[4] J. P. Berge,[4] S. Bertolucci,[5] S. Bhadra,[7] M. Binkley,[4] R. Blair,[1] C. Blocker,[2] V. Bolognesi,[13] A. W. Booth,[4] C. Boswell,[8] G. Brandenburg,[6] D. Brown,[6] E. Buckley-Geer,[17] H. S. Budd,[15] G. Busetto,[11] A. Byon-Wagner,[4] K. L. Byrum,[21] C. Campagnari,[3] M. Campbell,[3] A. Caner,[4] R. Carey,[6] W. Carithers,[10] D. Carlsmith,[21] J. T. Carroll,[4] R. Cashmore,[4,a] A. Castro,[11] F. Cervelli,[13] K. Chadwick,[4] G. Chiarelli,[5] W. Chinowsky,[10] S. Cihangir,[4] A. G. Clark,[4] D. Connor,[12] M. Contreras,[2] J. Cooper,[4] M. Cordelli,[5] D. Crane,[4] M. Curatolo,[5] C. Day,[4] F. DeJongh,[4] S. Dell'Agnello,[13] M. Dell'Orso,[13] L. Demortier,[2] B. Denby,[4] P. F. Derwent,[3] T. Devlin,[17] D. DiBitonto,[18] M. Dickson,[15] R. B. Drucker,[10] K. Einsweiler,[10] J. E. Elias,[4] R. Ely,[10] S. Eno,[3] S. Errede,[7] B. Esposito,[5] B. Flaugher,[4] G. W. Foster,[4] M. Franklin,[6] J. Freeman,[4] H. Frisch,[3] T. Fuess,[4] Y. Fukui,[9] Y. Funayama,[19] A. F. Garfinkel,[14] A. Gauthier,[7] S. Geer,[4] D. W. Gerdes,[3] P. Giannetti,[13] N. Giokaris,[16] P. Giromini,[5] L. Gladney,[12] M. Gold,[10] K. Goulianos,[16] H. Grassmann,[11] C. Grosso-Pilcher,[3] C. Haber,[10] S. R. Hahn,[4] R. Handler,[21] K. Hara,[19] R. M. Harris,[4] J. Hauser,[4] C. Hawk,[17] T. Hessing,[18] R. Hollebeek,[12] L. Holloway,[7] P. Hu,[17] B. Hubbard,[10] B. T. Huffman,[14] R. Hughes,[12] P. Hurst,[5] J. Huth,[4] J. Hylen,[4] M. Incagli,[13] T. Ino,[19] H. Iso,[19] H. Jensen,[4] C. P. Jessop,[6] R. P. Johnson,[4] U. Joshi,[4] R. W. Kadel,[10] T. Kamon,[18] S. Kanda,[19] D. A. Kardelis,[7] I. Karliner,[7] E. Kearns,[6] L. Keeble,[18] R. Kephart,[4] P. Kesten,[2] R. M. Keup,[7] H. Keutelian,[4] D. Kim,[4] S. Kim,[19] L. Kirsch,[2] K. Kondo,[19] J. Konigsberg,[6] E. Kovacs,[4] S. E. Kuhlmann,[1] E. Kuns,[17] A. T. Laasanen,[14] J. I. Lamoureux,[21] S. Leone,[13] W. Li,[1] P. Limon,[4] T. M. Liss,[7] N. Lockyer,[12] C. B. Luchini,[7] P. Lukens,[4] P. Maas,[21] K. Maeshima,[4] M. Mangano,[13] J. P. Marriner,[4] M. Mariotti,[13] R. Markeloff,[21] L. A. Markosky,[21] R. Mattingly,[2] P. McIntyre,[18] A. Menzione,[13] T. Meyer,[18] S. Mikamo,[9] M. Miller,[3] T. Mimashi,[19] S. Miscetti,[5] M. Mishina,[9] S. Miyashita,[19] Y. Morita,[19] S. Moulding,[2] J. Mueller,[17] A. Mukherjee,[4] L. F. Nakae,[2] I. Nakano,[19] C. Nelson,[4] C. Newman-Holmes,[4] J. S. T. Ng,[6] M. Ninomiya,[19] L. Nodulman,[1] S. Ogawa,[19] R. Paoletti,[13] A. Para,[4] E. Pare,[6] S. Park,[4] J. Patrick,[4] T. J. Phillips,[6] F. Ptohos,[6] R. Plunkett,[4] L. Pondrom,[21] J. Proudfoot,[1] G. Punzi,[13] D. Quarrie,[4] K. Ragan,[12] G. Redlinger,[3] J. Rhoades,[21] M. Roach,[20] F. Rimondi,[4,a] L. Ristori,[13] T. Rohaly,[12] A. Roodman,[3] W. K. Sakumoto,[15] A. Sansoni,[5] R. D. Sard,[7] A. Savoy-Navarro,[4] V. Scarpine,[7] P. Schlabach,[6] E. E. Schmidt,[4] O. Schneider,[10] M. H. Schub,[14] R. Schwitters,[6] A. Scribano,[13] S. Segler,[4] Y. Seiya,[19] M. Sekiguchi,[19] M. Shapiro,[10] N. M. Shaw,[14] M. Sheaff,[21] M. Shochet,[3] J. Siegrist,[10] P. Sinervo,[12] J. Skarha,[8] K. Sliwa,[20] D. A. Smith,[13] F. D. Snider,[8] L. Song, [12] M. Spahn,[10] R. St. Denis,[6] A. Stefanini,[13] G. Sullivan,[3]

R. L. Swartz, Jr.,[7] M. Takano,[19] F. Tartarelli,[13] K. Takikawa,[19] S. Tarem,[2] D. Theriot,[4] M. Timko,[18] P. Tipton,[4] S. Tkaczyk,[4] A. Tollestrup,[4] J. Tonnison,[14] W. Trischuk,[6] N. Turini,[13] Y. Tsay,[3] F. Ukegawa,[19] D. Underwood,[1] S. Vejcik, III,[8] R. Vidal,[4] R. G. Wagner,[1] R. L. Wagner,[4] N. Wainer,[4] J. Walsh,[12] T. Watts,[17] R. Webb,[18] C. Wendt,[21] H. Wenzel,[13] W. C. Wester, III,[10] T. Westhusing,[13] S. N. White,[16] A. B. Wicklund,[1] H. H. Williams,[12] B. L. Winer,[15] J. Wyss, [11] A. Yagil,[4] A. Yamashita,[19] K. Yasuoka,[19] G. P. Yeh,[4] J. Yoh,[4] M. Yokoyama,[19] J. C. Yun,[4] A. Zanetti,[13] F. Zetti,[13] S. Zucchelli [4,a]

(1) *Argonne National Laboratory, Argonne, Illinois 60439*

(2) *Brandeis University, Waltham, Massachusetts 02254*

(3) *University of Chicago, Chicago, Illinois 60637*

(4) *Fermi National Accelerator Laboratory, Batavia, Illinois 60510*

(5) *Laboratori Nazionali di Frascati, Istituto Nazionale di Fisica Nucleare, Frascati, Italy*

(6) *Harvard University, Cambridge, Massachusetts 02138*

(7) *University of Illinois, Urbana, Illinois 61801*

(8) *The Johns Hopkins University, Baltimore, Maryland 21218*

(9) *National Laboratory for High Energy Physics (KEK), Japan*

(10) *Lawrence Berkeley Laboratory, Berkeley, California 94720*

(11) *Universita di Padova, Instituto Nazionale di Fisica Nucleare, Sezione di Padova, I-35131 Padova, Italy*

(12) *University of Pennsylvania, Philadelphia, Pennsylvania 19104*

(13) *Istituto Nazionale di Fisica Nucleare, University and Scuola Normale Superiore of Pisa, I-56100 Pisa, Italy*

(14) *Purdue University, West Lafayette, Indiana 47907*

(15) *University of Rochester, Rochester, New York 14627*

(16) *Rockefeller University, New York, New York 10021*

(17) *Rutgers University, Piscataway, New Jersey 08854*

(18) *Texas A&M University, College Station, Texas 77843*

(19) *University of Tsukuba, Tsukuba, Ibaraki 305, Japan*

(20) *Tufts University, Medford, Massachusetts 02155*

(21) *University of Wisconsin, Madison, Wisconsin 53706*

Contents

Synopsis 1

1 Introduction 4

1.1 W boson production in $\bar{p}p$ collisions 5

1.2 $W \rightarrow \ell\nu$ decay 7

1.3 Reconstruction of W events 8

1.4 Lepton charge asymmetry in W boson decays 9

1.5 Probing $u(x)/d(x)$ 10

2 Apparatus 15

2.1 Tevatron $\bar{p}p$ collider 15

2.2 Collider Detector at Fermilab 17

2.3 CDF detector components 18

2.3.1 Beam-Beam Counters 18

2.3.2 Vertex Time Projection Chamber 18

2.3.3 Central Tracking Chamber 19

2.3.4 Central Calorimeter 20

2.3.5 Plug Calorimeter 22

2.3.6 Forward Calorimeter 24

2.3.7 Central muon detector 25

3 Common data sets **36**

3.1 Data acquisition 36

3.1.1 Level 0 37

3.1.2 Level 1 37

3.1.3 Level 2 38

3.1.4 Level 3 39

3.2 Reconstrucion of the data 39

3.2.1 Event vertex 39

3.2.2 Tracks 40

3.2.3 Calorimeter towers 40

3.2.4 Missing transverse energy 41

3.2.5 Electromagnetic calorimeter clusters 42

3.2.6 Jets 43

3.2.7 Muons 44

3.3 Reconstructed data tapes 44

4 Event selection **46**

4.1 Particle identification parameters 46

4.1.1 Central electron parameters 47

4.1.2 Plug electron parameters 51

4.2 Electron selection 54

4.2.1 Inclusive central electron sample 54

4.2.2 Inclusive plug electron sample 57

4.3 W samples 59

4.3.1 Kinematical parameters 59

4.3.2 Statistics 60

5 Energy scale and efficiency for electrons **78**

5.1 Energy scale 78
5.1.1 Momentum scale 79
5.1.2 Energy scale of the central electromagnetic calorimeter 79
5.1.3 Energy scale of the plug electromagnetic calorimeter 80
5.2 Electron identification efficiency 84
5.2.1 Off-line track finding efficiency 84
5.2.2 Trigger efficiency 88
5.2.3 Electron identification cut efficiencies 90

6 Background **99**
6.1 Background from QCD jet and heavy flavour production 99
6.1.1 Method 100
6.1.2 Background in the central W sample 102
6.1.3 Background in the plug W sample 102
6.2 Other background sources 103
6.2.1 $W \rightarrow \tau\nu$ 104
6.2.2 $Z \rightarrow ee$ 104
6.2.3 $Z \rightarrow \tau\tau$ 104

7 Asymmetry analysis **111**
7.1 Analysis of lepton charge asymmetry 111
7.2 Uncertainties 113
7.2.1 Charge dependence of the electron reconstruction efficiencies . . 113
7.2.2 Trigger efficiency in the plug 114
7.2.3 Background contamination 115
7.2.4 Misidentification of the electron charge 119
7.2.5 Dead channels 121
7.3 Summary 122

8 Results and discussion **125**

8.1 Theoretical predictions 125

8.2 Chi-square test 128

8.3 Higher order effects 129

8.3.1 Method 1 129

8.3.2 Method 2 131

8.3.3 Next-to-leading order calculation 131

8.3.4 Summary of the higher order effects 132

9 Conclusions **141**

Bibliography **143**

Appendix **147**

A.1 Dead layers and the quadrant gain constants in the plug 147

A.2 Dead channels in the plug 148

A.3 A study of the CTC track reconstruction efficiency in the plug region . 148

List of Tables

4.1 On-line trigger parameters for central electrons 56

4.2 Cut values for central electron identification parameters 56

4.3 On-line trigger parameters for plug electrons 58

4.4 Cut values for plug electron identification parameters 58

4.5 Kinematical cuts for W selection 59

5.1 Selection parameters for the central Ws for the track finding efficiency analysis 85

5.2 Selection parameters for the plug Ws for the track efficiency analysis . 86

5.3 Track selection parameters for the plug electrons. 86

5.4 Selection parameters for the central Ws for the trigger efficiency analysis 88

5.5 Selection parameters for the plug electromagnetic clusters for the track efficiency analysis 89

5.6 Selection parameters for the central Ws for the trigger efficiency analysis 90

5.7 Efficiencies for the identification parameters of the central electron . . . 91

5.8 Selection parameters for the plug Ws for the trigger efficiency analysis . 91

5.9 Efficiencies for the identification parameters of the plug electron 92

6.1 Selection parameters for two-jet background sample 100

6.2 Summary of acceptances for the W, Z and background events and the numbers of candidates 103

7.1 Pseudo-rapidity distributions of electrons and positrons and the charge asymmetry. 112
7.2 Trigger efficiency effect on the asymmetry measurement in the plug region. 115
7.3 Corrections for QCD jet and heavy flavor background corrections on the asymmetry measurement 116
7.4 The asymmetry values from $W \rightarrow \tau\nu \rightarrow e\nu\nu\nu$ decays. 117
7.5 A charge distribution of $Z \rightarrow ee$ events. 118
7.6 Charge misidentification probabilities in the plug region estimated using the CDF detector simulation. 120
7.7 Summary of the charge asymmetry and its uncertainties in the plug region. 121

8.1 Charge asymmery in the central and plug $W \rightarrow e\nu$ events. 126
8.2 Examples of the parametrization in EHLQ, DO, HMRS, and DFLM structure functions. 127
8.3 A summary of the beam, target, and probing x-Q^2 range of the deep-inelastic scattering experiments. 128
8.4 A summary of a chi-square test on various sets of structure functions. . 128

A.1 Dead planes and the quadrant gain constants in the plug calorimeter during 1988-89 run. 147
A.2 A summary of dead channels in the plug calorimeter during the 1988-1989 run. 148
A.3 Charge distributions of the tracks reconstructed by two versions of track finding algorithm. 149
A.4 A charge distribution for the combined sample of two versions of track finding algorithm. 149

List of Figures

1.1 W production in $\bar{p}p$ collisions. 12

1.2 W production cross section. 13

1.3 The ratio $d(x)/u(x)$ at $Q^2 = M_W^2$ and $0.005 < x < 0.1$. 14

2.1 Tevatron proton-antiproton collider. 26

2.2 The CDF 27

2.3 Cut-away view of the CDF 28

2.4 Beam Beam Counter. 29

2.5 Vertex Time Projection Chamber. 30

2.6 Central Tracking Chamber. 31

2.7 A wedge of the central calorimeter. 32

2.8 A cut view of a quadrant of the calorimeter. 33

2.9 A quadrant of the plug electromagnetic calorimeter. 34

2.10 A module of the central muon chamber. 35

4.1 A distribution of $Lshr$ for electrons from $W \rightarrow e\nu$ decays. 62

4.2 A distribution of χ^2_{strip} for electrons from $W \rightarrow e\nu$ decays. 63

4.3 A distribution of $E_{\rm Had}/E_{\rm EM}$ for central electrons from $W \rightarrow e\nu$ decays. 64

4.4 A distribution of E/p for central electrons from $W \rightarrow e\nu$ decays. 65

4.5 A distribution of ΔX for central electrons from $W \rightarrow e\nu$ decays. 66

4.6 A distribution of ΔZ for central electrons from $W \rightarrow e\nu$ decays. 67

4.7 A distribution of χ^2_{rmPEM} for electrons from $W \rightarrow e\nu$ decays. 68
4.8 A distribution of $E_{\rm Had}/E_{\rm EM}$ for plug electrons from $W \rightarrow e\nu$ decays. . . 69
4.9 A distribution of E/p for plug electrons from $W \rightarrow e\nu$ decays. 70
4.10 A distribution of $\Delta\phi$ for plug electrons from $W \rightarrow e\nu$ decays. 71
4.11 A distribution of ΔR for plug electrons from $W \rightarrow e\nu$ decays. 72
4.12 A distribution of *VTPC-hit-occupancy* for plug electrons from $W \rightarrow e\nu$ decays. 73
4.13 Electron $E_{\rm T}$ and $\not{E}_{\rm T}$ distributions for the central Ws. 74
4.14 A transverse mass distribution for the central Ws. 75
4.15 Electron $E_{\rm T}$ and $\not{E}_{\rm T}$ distributions for the plug Ws. 76
4.16 A transverse mass distribution for the plug Ws. 77

5.1 An invariant mass distribution for two-muon system near the J/ψ mass. 93
5.2 An invariant mass distribution for the central-plug Z candidates. 94
5.3 A transverse mass distribution for the plug W candidates. 95
5.4 A transverse mass distribution for W candidates with a low momentum track. 96
5.5 Trigger efficiency curves for central electrons. 97
5.6 Trigger efficiency curves for plug electrons. 98

6.1 Schematic diagram of signal regions for the W event and the background. 106
6.2 Isolation distributions for a two-jet background sample in the central. . 107
6.3 An isolation distribution for the central W sample. 108
6.4 An isolation distributions for a two-jet background sample in the plug. 109
6.5 An isolation distribution for the plug W sample. 110

7.1 Charge asymmetry distribution without corrections. 123

7.2 Number of CTC wire hits in super-layer 2 used for the track reconstruction in the plug region. 124

8.1 Lepton charge asymmetry distribution. 133

8.2 Next-to-leading order diagrams for the W boson production. 134

8.3 Distributions of the transverse momentum of the underlying events. . . 135

8.4 The parallel and perpendicular components of the transverse momentum of the underlying events. 136

8.5 The effect of the underlying events on lepton charge asymmetry. 137

8.6 An effect of the underlying events on the electron pseudo-rapidity distribution. 138

8.7 A predicted effect of the parton jet on lepton charge asymmetry by Papageno Monte Carlo. 139

8.8 A predicted distribution of the lepton charge asymmetry as a function of lepton pseudo-rapidity at next-to-leading order calculation. 140

Synopsis

We measured the charge asymmetry in the pseudo-rapidity distribution of decay leptons from W bosons produced in proton-antiproton collisions at $\sqrt{s} = 1.8$ TeV. Electrons favor to decay in the proton momentum direction in the W rest-frame as a result of the V–A left-handed coupling, while positrons favor to decay in the antiproton momentum direction. Imbalanced momenta of partons involved in the W production boost W^-s against the proton momentum direction, and W^+s against the anti-proton momentum direction. A charge asymmetric pseudo-rapidity distribution of the decay leptons is described as a combined result of the V–A coupling and the parton momentum distribution. A measurement of the lepton charge asymmetry in the lepton pseudo-rapidity distributions allows us to probe into the proton structure in the region of small x ($0.01 < x < 0.2$) and large Q^2 ($\sim M_W^2$).

The data were collected by the Collider Detector at Fermilab (CDF) during the run from June of 1988 to May of 1989. With an integrated luminosity of 4.1 pb^{-1}, we observed about 4500 events of the $p\bar{p} \rightarrow WX \rightarrow e\nu X$ interaction.

The CDF is a general purpose detector composed of a set of tracking detectors and a set of calorimeters, which are described in Chapter 2. Electrons and neutrinos are efficiently detected and reconstructed in the CDF. The events were selected by a coarse reconstruction of the particles of interest and recorded on data tapes. This selection process was performed by four levels of the event trigger system. The final reconstruction was performed on the data on tapes and the data were reduced based on the particle identification and the higher transverse energy thresholds. The data reduction procedures are described in Chapter 3. The $W \rightarrow e\nu$ event is identified by the existence of an electron with high transverse energy and a neutrino with a high missing transverse energy. We used W event sample whose electrons were found in a

pseudo-rapidity region $0 < |\eta| < 1.7$. The identification parameters for $W \rightarrow e\nu$ events are described in Chapter 4.

The energy scale calibration and electron identification efficiencies are discussed in Chapter 5. The energy scale of the calorimetry for electrons was carefully studied and the corrections were applied to ensure the final energy measurement of electrons. The efficiencies for the electron reconstruction and identification were studied focusing on the difference between electrons and positrons, which affects the asymmetry measurement. The efficiencies for every identification parameters were found to more than 90% and no significant difference between electrons and positrons was observed. The trigger efficiency was 97% for the electrons and positrons in the central region ($0 < |\eta| < 1.1$). In the plug region ($1.32 < |\eta| < 2.22$), the trigger was not efficient enough near the transverse energy threshold. It was measured as a function of the transverse energy.

Background contamination in the $W \rightarrow e\nu$ event sample is estimated in Chapter 6. Sources of background contaminations include QCD jets and heavy flavor productions, and W/Z boson decays $W \rightarrow \tau\nu$, $Z \rightarrow ee$ and $Z \rightarrow \tau\tau$. The contaminations due to QCD jets and heavy flavor events were measured to be less than 0.7% for the central region and less than 2.4% for the plug region. The $W \rightarrow \tau\nu$ contamination was estimated to be 3.7% for the central region and 1.0% for the plug region. The $Z \rightarrow ee$ and $Z \rightarrow \tau\tau$ contaminations were found to be less than 1% for the central and the plug region.

The analysis of the lepton charge asymmetry is described in Chapter 7. Systematic uncertainties due to the electron and positron identifications and the background contaminations were found to make a negligibly small contribution to the asymmetry measurement in the central region. The asymmetry value in the plug region was slightly corrected by the trigger efficiency factor, and small uncertainty from the background contamination was added.

The measured asymmetry is compared with theoretical predictions in Chapter 8. A

set of the proton structure functions provides a pseudo-rapidity distribution of decay leptons, assuming the V–A coupling responsible for the lepton distribution in the W rest frame. A comparison of the measured and predicted charge asymmetries allows us to resolve a proper structure function with our data. We found HMRS, EHLQ and DFLM sets showed consistency among well-known sets of structure function widely used today. The DO sets were ruled out at a confidence level of 90%. The effects from the next-to-leading order diagrams were small compared to the statistical uncertainties.

Chapter 1

Introduction

Discovery of the W and Z vector bosons, carriers of the weak force [1] is one of the major achievements of the high energy physics experiments in 1980s using proton-antiproton colliders. The discovery supports the standard model of the particle physics. The standard model and a set of proton structure functions are standard tools to describe various events in the proton-antiproton collisions. In other words, precise knowledge of the standard model parameters and the proton structure functions might reveal the limit of standard model and would allows us to go beyond the standard model.

The Collider Detector at Fermilab (CDF) accumulated an integrated luminosity of 4.1 pb^{-1} in proton-antiproton collisions at $\sqrt{s} = 1.8$ TeV during the run from June of 1988 to May of 1989. The CDF collected 4500 $W \rightarrow e\nu$ events. Standard model parameters, the W mass (M_W) [2] and the Z mass (M_Z) [3] and the Weinberg angle (θ_W) [4] have already been measured by the CDF:

$$M_W = 79.92 \pm 0.45 \text{ GeV}/c^2 \tag{1.1}$$

$$M_Z = 90.9 \pm 0.3 \pm 0.2 \text{ GeV}/c^2 \tag{1.2}$$

$$\sin^2\theta_W = 0.2317 \pm 0.0075 \tag{1.3}$$

These values compares to the measurements of $M_W = 80.49 \pm 0.49$ GeV and $\sin^2\theta_W = 0.2202 \pm 0.0095$ by another proton-antiproton collider experiment at CERN Sp$\bar{p}$S Collider [5], and the Z mass value compares to the measurement of $M_Z = 91.161 \pm 0.031$ GeV by the electron-positron colliders, SLC and LEP experiments [6]. High statistics of W events produced in proton-antiproton collisions enable us to measure detailed properties of the W production and decay.

1.1 W boson production in $\bar{p}p$ collisions

Currently the $W^{\pm}$ bosons are produced only in hadron colliders. The W boson is created by an annihilation of quark parton and antiquark parton in $\bar{p}$p collisions, whose diagram is shown in Figure 1.1. Approximately 85% of the Ws are produced by valence-quark and valence-quark annihilations or valence-quark and sea-quark annihilations at the Tevatron energy [7]. Rest of 15% are produced by sea-quark and sea-quark annihilations. The W production cross section is shown in Figure 1.2 as a function of a center-of-mass energy. The differential cross-section for W^+ production in $\bar{p}$p collisions is written as:

$$\frac{d\sigma}{dy}(\bar{p}p \to W^+X) = K\frac{2\pi G_F}{3\sqrt{2}}x_1x_2\left\{u(x_1)d_c(x_2) + \bar{d}_c(x_1)\bar{u}(x_2)\right\}, \tag{1.4}$$

where x_1 and x_2 are evaluated at

$$x_{1,2} = \frac{M_W}{\sqrt{s}}e^{\pm y}, \tag{1.5}$$

and

$$d_c(x) = d(x)\cos\theta_c + s(x)\sin\theta_c, \tag{1.6}$$

and y, K, G_F, and θ_c denote the rapidity of W, the K factor, the weak coupling constant, and the Cabibbo angle, respectively. The factor K is associated with higher order contributions, real gluon radiation, the vertex correction and the Compton scattering ($qg \rightarrow q'W$). The functions $u(x)$, $d(x)$ and $s(x)$, represent densities of up-quark (u-quark), down-quark (d-quark) and strange-quark (s-quark) with a momentum fraction x of proton. In Equation 1.4, partons from protons carry a momuntum fraction x_1 and partons from antiprotons carry a momentum fraction x_2. Antiquark parton density in the antiproton is replaced by quark parton density in the proton by means of the invariance under the charge conjugation,

$$q(x) \equiv q^p(x) = \bar{q}^{\bar{p}}(x) \tag{1.7}$$

where $q^p(x)$ represents quark density in the proton and $\bar{q}^{\bar{p}}(x)$ represents antiquark density in the antiproton. The quark density $q(x)$ is defined as a sum of the valence and sea quark densities:

$$q(x) \equiv q_v(x) + q_s(x), \tag{1.8}$$

where $q_v(x)$ represents valence-quark density and $q_s(x)$ represents sea-quark density.

The W^+ boson acquires a longitudinal momentum

$$x_{W^+} = x_1 - x_2 = \frac{2M_W}{\sqrt{s}} \sinh y \tag{1.9}$$

into the direction of the proton momentum. The u_v-quark in the proton has higher average momentum than d_v-quark [8]. Since the majority of W^+ productions are originated by the annihilation of u-quark in the proton and $\bar{d}$-quark in the antiproton, W^+ bosons tend to have a longitudinal momentum into the proton momentum direction.

Interchanging x_1 and x_2 in Equation (1.4), one obtains the differential cross-section

for the W^- production. The W^- boson acquires a longitudinal momentum

$$x_{W^-} = x_2 - x_1 = \frac{2M_W}{\sqrt{s}} \sinh(-y) \tag{1.10}$$

into the direction of the proton momentum. Therefore W^- bosons favor the antiproton momentum direction, contrary to W^+ bosons.

1.2 $W \to \ell\nu$ decay

The W boson decays in accordance with the V–A coupling in the standard model. First evidence of the V–A coupling is observed in β-decay in 1957 [9]. Angular distribution of electrons from beta-decays were in agreement with the V–A theory proposed by Marshak and Sudarshan and by Feynman and Gell-Mann. The V–A theory was a satisfactory description of all weak interaction data. Recent precise $\mu \to e\nu\nu$ decay experiment [10] is still consistent with V–A theory. Charged current interaction is believed to have a pure V–A form in the standard model.

The differential cross section for the parton-level process $u\bar{d} \to W^+ \to \ell^+\nu$ is written as follows:

$$\frac{d\hat{\sigma}}{d\cos\hat{\theta}}(u\bar{d} \to W^+ \to l^+\nu) = \frac{|V_{ud}|^2}{8\pi}\left(\frac{G_F M_W^2}{\sqrt{2}}\right)^2 \frac{\hat{s}(1-\cos\hat{\theta})^2}{(\hat{s}-M_W^2)^2 + (\Gamma_W M_W)^2} \tag{1.11}$$

where $\hat{\theta}$ is the polar angle of the lepton momentum with respect to the direction of the proton momentum in the W-rest frame and $\hat{s}$ is a square of the center-of-mass energy of the u-$\bar{d}$ system. As a result of the helicity suppression, the angular distribution of the decay lepton ℓ^+ in the W rest frame has a peak at $\hat{\theta} = 180°$, that is, in the opposite direction of the W^+-boson boost. The differential cross section for $d\bar{u} \to W^- \to l^-\nu$ is proportional to $(1+\cos\hat{\theta})^2$. The ℓ^- from W^- bosons favor the proton momentum

direction contrary to the W^--boson boost.

By combining Equation (1.4) and Equation (1.11), the pseudo-rapidity distribution of lepton ℓ^+ is represented as a sum of the rapidity distribution of W^+ and the angular distribution of lepton ℓ^+ in the W-rest frame:

$$\frac{d\sigma^+(\eta_\ell)}{d\eta_\ell} = \frac{1}{3}\int_0^1 dx_1 \int_0^1 dx_2 \left\{u(x_1)d_c(x_2) + \bar{d}_c(x_1)\bar{u}(x_2)\right\} \left[\frac{d\hat{\sigma}}{d\cos\hat{\theta}} \sin^2\hat{\theta}\right] \quad (1.12)$$

where η_ℓ is the pseudo-rapidity of decay lepton and $\hat{\theta}$ is the polar angle of lepton ℓ^+ in the W rest frame. The pseudo-rapidity of lepton, η_ℓ, is related to $\hat{\theta}$ as follows:

$$\eta_\ell = -\ln\left(\tan(\frac{\hat{\theta}}{2})\right) + \frac{1}{2}\ln(\frac{x_1}{x_2}). \quad (1.13)$$

The lepton pseudo-rapidity distribution, therefore, essentially reflects the V–A coupling and the W rapidity distribution.

1.3 Reconstruction of W events

Complete reconstruction of the $W \to \ell\nu$ events enables us to measure the $(1+q(\cos\hat{\theta}))^2$ distribution of leptons and the rapidity distribution of W bosons independently. Here q is a charge of the lepton. Experimentally three momenta of electron are well measured. The transverse mometum of neutrino is measured as missing transverse momentum. Invariant mass of the W boson constraints the longitudinal momentum of neutrino as follows:

$$p_L^\nu = \frac{2(M_W^2 + 2(\vec{p_T^e} \cdot \vec{p_T^\nu}))p_L^e \pm \sqrt{D}}{4{p_T^e}^2} \quad (1.14)$$

here,

$$D = 4E_e^2(M_W^2 - M_{tr}^2)(M_W^2 - M_{tr}^2 + 4|p_T^e||p_T^\nu|) \quad (1.15)$$

where M_W, M_{tr}, E_ℓ, p_T^ℓ and p_L^ℓ denote the W boson mass, the transverse mass of the W, the energy of the lepton, the transverse momentum of the lepton and the longitudinal momentum of the lepton. We have two solutions for the W rapidity corresponding to two solutions of the longitudinal neutrino momentum. At the Sp$\bar{p}$S energy $\sqrt{s}$ = 560 GeV, this ambiguity was solved by taking the smaller W rapidity solution in $\sim$ 70% of the events and one solution was unphysical in 6.2% of the events [11]. At the Tevatron energy $\sqrt{s}$ = 1.8 TeV, taking the smaller solution of the W rapidity chooses a right solution with about 60% probability from a Monte Carlo study. In our analysis, therefore, we measure the W rapidity distribution indirectly via the pseudo-rapidity distribution of the charged leptons.

1.4 Lepton charge asymmetry in W boson decays

We introduce a lepton charge asymmetry (A_ℓ) by

$$A_\ell(M_{tr}^{th}, \eta_\ell) \equiv \frac{N_{\ell^+}(\eta_\ell) - N_{\ell^-}(\eta_\ell)}{N_{\ell^+}(\eta_\ell) + N_{\ell^-}(\eta_\ell)}, \tag{1.16}$$

where $N_{\ell^\pm}(\eta_\ell)$ is the number of charged leptons observed at pseudo-rapidity η_ℓ in the laboratory system and M_{tr} is a transverse mass threshold.

$N_{\ell^\pm}(\eta_\ell)$ is given by

$$N_{\ell^\pm}(\eta_\ell) = \epsilon(\ell^\pm) \cdot Ac(W^\pm) \cdot \left\{ \int_{\eta_\ell - \Delta\eta/2}^{\eta_\ell + \Delta\eta/2} \left(\frac{d\sigma^\pm(\eta)}{d\eta} \right) d\eta \right\} \cdot \int \mathcal{L} dt, \tag{1.17}$$

where ϵ denotes the detection efficiency of leptons, Ac denotes the acceptance for $W \to \ell\nu$ events and $\int \mathcal{L} dt$ represents the integrated luminosity. The integration over η extends over a bin width $\Delta\eta$ about the pseudo-rapidity point η_ℓ where we count the number of leptons. The efficiency $\epsilon(\ell^\pm)$ may have pseudo-rapidity dependence in

practice because the detector does have non-uniform construction in η. The luminosity measurement in the CDF has about 7% uncertainty [12]. The measurement of the lepton pseudo-rapidity distribution is influenced by these uncertainties. By virtue of taking a ratio in the definition (1.16), the luminosity factor cancels out in the asymmetry A_ℓ. The efficiency factor also cancels out if the efficiency for positrons is equal to that for electrons, that is, $\epsilon(\ell^+) = \epsilon(\ell^-)$. These are the reasons why we measure the asymmetry distribution instead of the lepton pseudo-rapidity distribution itself. The asymmetry distribution provides similar information as the lepton pseudo-rapidity distribution, but is less sensitive to systematic uncertainties.

1.5 Probing $u(x)/d(x)$

At the Tevatron energy $\sqrt{s} = 1.8$ TeV, we can probe the small x region $0.01 < x < 0.2$ corresponding to the W repidity region $-1.5 < y < +1.5$ by Equation 1.5, at large Q^2 ($\sim M_W^2$) using the W events. The lepton charge asymmetry comes from the asymmetric $(1+q\cos\theta)^2$ distribution of leptons in the W rest frame and the asymmetric W rapidity distribution, as described above. The asymmetry in the W rapidity distribution [13] is defined as follows:

$$\begin{aligned} A_{W^+}(y) &= A_{W^-}(-y) \\ &\equiv \frac{d\sigma_{W^+}/dy - d\sigma_{W^+}/dy}{d\sigma_{W^+}/dy + d\sigma_{W^+}/dy} \end{aligned} \tag{1.18}$$

where $d\sigma_{W^+}/dy$ is defined in Equation 1.4. Using the quark densities $u(x)$ and $d(x)$, A_{W^+} is expressed as:

$$A_{W^+} \cong \frac{1}{D(\sqrt{s}, y)} \left[\frac{u(x_1) - d(x_1)}{u(x_1) + d(x_1)} - \frac{u(x_2) - d(x_2)}{u(x_2) + d(x_2)} \right] \tag{1.19}$$

where we assume SU(2)-symmetric sea-quark densities: $\bar{u}(x) = \bar{d}(x)$. Here

$$D(y) = 1 - \frac{u(x_1) - d(x_1)}{u(x_1) + d(x_1)} \cdot \frac{u(x_2) - d(x_2)}{u(x_2) + d(x_2)} + \frac{\bar{u}(x_1) - \bar{d}(x_1)}{u(x_1) + d(x_1)} \cdot \frac{\bar{u}(x_2) - \bar{d}(x_2)}{u(x_2) + d(x_2)}. \quad (1.20)$$

In the region of x_1 and x_2 of interest at the Tevatron energy, and with the rapidity range $-1 < y < 1$, the function $D(y)$ is fairly constant, with $D(y) \cong 1.1$. Then we find the A_{W^+} is now given as a function of the ratio $d(x)/u(x)$. Using a linear approximation, $d(x)/u(x) = 1 - ax$, appropriate for the limited range of x of interest to us, we derive

$$A_{W^+}(y) \cong a\frac{M_W}{\sqrt{s}} \sinh y, \quad (1.21)$$

where we use an apploximation,$ad(x)/u(x) \ll 2$. Measuring $A_{W^+}(y)$ therefore determines the effective slope a. The x dependence of the ratio $d(x)/u(x)$ is shown in Figure 1.3 for the four well-known sets of structure function (HMRS, DFLM, EHLQ, DO). The lepton charge asymmetry measurement is also sensitive to the ratio $d(x)/u(x)$.

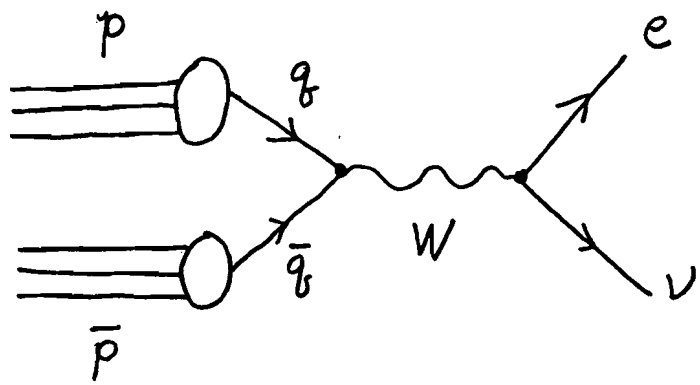

Figure 1.1: Leading order diagram for the W production in $\bar{p}p$ collisions.

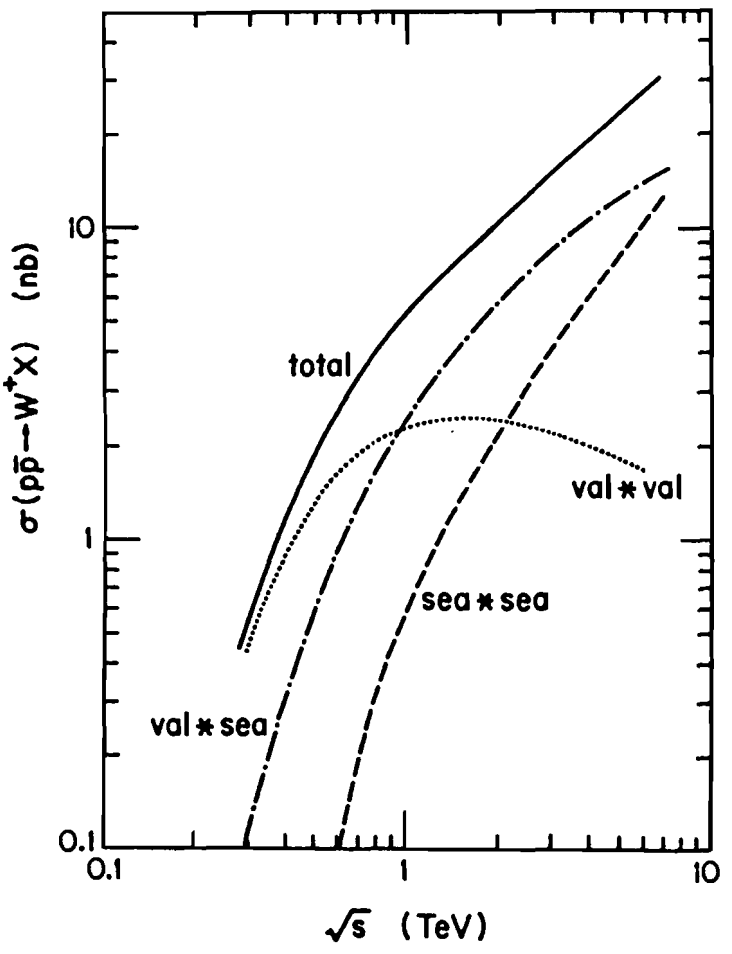

Figure 1.2: W production cross sections in $\bar{p}p$ collisions are shown as a function of the center of mass energy.

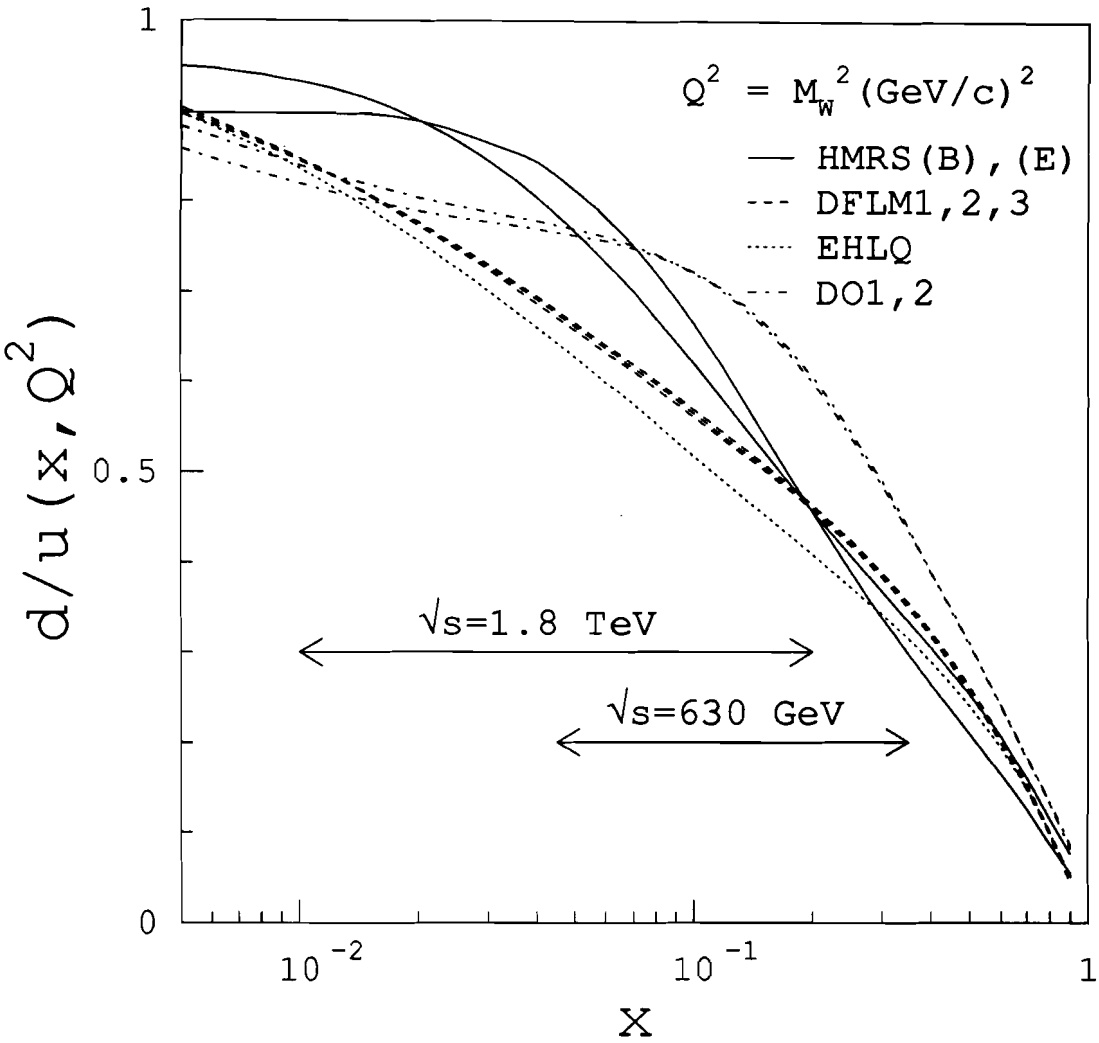

Figure 1.3: The ratio $d(x)/u(x)$ at $Q^2 = M_W^2$ and $0.005 < x < 0.1$ for the HMRS(B),(E) (solid), DFLM1,2,3 (dashed), EHLQ (dotted), DO (dot-dashed), sets of structure function.

Chapter 2

Apparatus

2.1 Tevatron $\bar{p}p$ collider

The Tevatron Collider at Fermilab has provided the highest energy protons (900 GeV) and anti-protons (900 GeV) colliding at a center-of-mass energy of 1.8 TeV since 1985. The Tevatron consists of five stage accelerators as illustrated in Figure 2.1. First negatively ionized hydrogen ions are injected to DC voltage accelerator (Cockcroft-Walton electrostatic accelerator). They are accelerated up to 750 keV, then passed to 500-foot-long linear accelerator. During the acceleration in the linac electrons bound on hydrogen ion are removed and then protons acquire 200 MeV. The protons are transfered to the booster ring, a synchrotron with a diameter of 500 feet, where they are accelerated to 8 GeV. The protons are then injected to the main ring, a synchrotron with a diameter of two kilometers, which is composed of water-cooled magnets. The protons are accelerated to 150 GeV in the main ring, are finally transferred to the Tevatron ring, a synchrotron with a diameter of two kilometers, composed of superconducting magnets, where they are accelerated to 900 GeV.

Protons accelerated to 150 GeV are also used to initiate production of the anti-protons. The main ring provides 10^{10} protons per bunch, which strike a tungsten

target and produce 10^4 anti-protons. The anti-protons are collected in the debuncher ring which is operated at 8 GeV. The captured beam of anti-protons, circulating the Debuncher ring, is then made more dense by a process called stochastic cooling. The anti-protons are then transferred to the accumulator ring where the anti-protons are merged into a single beam, cooled further and stored over a period of hours or even a day until the number reaches 10^{10}.

Major achievements of the Tevatron are not only the beam energy, but also its luminosity. The product of luminosity and cross section gives the number of events produced.

$$N = L \cdot \sigma \tag{2.1}$$

If we aim at a rare event, high luminosity is necessary to observe it. Luminosity is written down as follows.

$$L = \frac{N_p N_{\bar{p}} f B}{\epsilon \beta} \tag{2.2}$$

N_p	:	number of protons per bunch
$N_{\bar{p}}$	:	number of anti-protons per bunch
f	:	revolution frequency
B	:	number of bunches
ϵ	:	emittance
β	:	beta

A large number of particles in a bunch or small beam size provide a large luminosity. The Tevatron provided an instantaneous luminosity of $L \sim 10^{30}\mathrm{cm}^{-2}\mathrm{s}^{-1}$ during the 1988-1989 run.

The run started in June of 1988 and ended in May of 1989. Integrated luminosity of $\int Ldt = 4.1\,\mathrm{pb}^{-1}$ has been collected by the CDF. The Tevatron provided 9.8 pb^{-1}. The event trigger system lost about 20% of events at the peak luminosity because of the

dead time which was used for a trigger decision. Hardware and software problems lost a portion of luminosity. Mistakes of the manipulation of the system also lost luminosity. Overall efficiency of the CDF was 42%.

2.2 Collider Detector at Fermilab

The Collider Detector at Fermilab (CDF) is a general purpose detector located on the Tevatron ring, where collisions between proton and anti-proton beams travelling in opposite direction are observed. A perspective view of the CDF detector is shown in Figure 2.2 and the cut-away view in Figure 2.3 shows the location of each detector component. Each detector component is designed to look into the collision point in order to capture the decay products in $\bar{p}p$ collisions. The tracking chambers, the vertex time projection chamber (VTPC), the central tracking chamber (CTC) and the central drift tube (CDT), are azimuthally symmetric surrounding the beam axis. They are located inside of the cylindrical superconducting solenoid, which generates 14 kG magnetic field along the beam axis. Low-mass design of the inner chamber allows the particles to traverse the tracking volume with a minimum energy loss. The solenoid is surrounded by calorimeters with thick material. They are the central electromagnetic and hadronic calorimeters (CEM, CHA), the endwall hadronic calorimeter (WHA), the plug electromagnetic and hadronic calorimeters (PEM, PHA), and the forward electromagnetic and hadronic calorimeters (FEM, FHA). Those calorimeters are a sampling type calorimeter. While most of the particles stop within the calorimeters, muons and neutrinos escape from them. The muon detectors (CMU, FMU) which are composed of several layers of drift chambers are placed outside of the calorimeter in order to detect muons. A complete description can be found in [14] and references therein. Detectors used in this analysis briefly reviewed in the following sections.

The origin of the CDF coordinate system is at the center of the detector. The z-axis

points in the proton beam direction, from west to east. The y-axis points vertically upward and the x-axis points radially out of the Tevatron ring, so as to make a right-handed coordinate system. The azimuthal angle ϕ is measured from the positive x-axis to the positive y-axis. The polar angle θ is measured from the proton beam direction. The pseudo-rapidity $\eta \equiv -\ln(\tan\theta/2)$ is often used instead of θ. The radius r is measured from the beam axis which is in x-y plane.

2.3 CDF detector components

2.3.1 Beam-Beam Counters

The beam-beam counter system (BBC) consists of two planes of scintillation counters placed at a distance of 5.91 m on the front face of each of the forward and the backward shower counters [14]. A beam's eye view of one of the BBC is shown in Figure 2.4. They cover the angular region from 0.32° to 4.47°, corresponding to a pseudo-rapidity range of 3.24 to 5.90. The BBC provides a minimum-bias trigger initiating the data acquisition for the detector and is also used as the primary luminosity monitor. The minimum-bias trigger is defined by the requirement that at least one counter fires in each BBC plane within a 15 ns window centered on 20 ns after the beam-crossing time. The timing resolution of the counters is less than 200 ps.

2.3.2 Vertex Time Projection Chamber

The vertex time projection chamber (VTPC) consists of eight octagonal time proportional chambers surrounding the beam pipe [15]. The VTPC extends 1.4 m on each side of the center of the detector. Each module has an octagonal cross section with a diameter of 55.4 cm. Electric field is applied along the beam axis. A central high voltage grid partitions each module into two 15.25 cm long drift regions (Figure 2.5),

which permits the maximum drift time to be less than the beam-beam crossing time of 3.5 μsec with the drift velocity of 46 μm/ns. Each drift region is terminated with the end cap at both ends of each module, which has 24 sense wires and 24 cathode pads.

The electrons drift away from the center grid until they pass through a cathode grid and enter one of the two proportional chamber endcaps. The sense wires and the cathode pads are instrumented with FASTBUS TDC and an analog pulse height readout using flash analog to digital converters (FADCs). The arrival time of the electrons at the sense wires gives a picture of the event in r-z plane. The pulse height information on the cathode pads gives ϕ information.

The VTPC determines the location of the $\bar{p}p$ interaction point, by finding the point of convergence of all the reconstructed r-z tracks in the event. The resolution on the z coordinate of this measurement is about 1 to 2 mm, depending on the track multiplicity. Collision points have a gaussian distribution with a sigma of 35 cm, thus well within the VTPC.

2.3.3 Central Tracking Chamber

The central tracking chamber (CTC) is a cylindrical chamber with a length of 3.2 m and an outer diameter of 2.76 m, and an inner diameter of 0.55 m [16]. The CTC surrounds the VTPC and fits inside the superconducting solenoid which provides a 1.4 T axial magnetic field. The chamber contains 84 layers of sense wire, arranged into nine super-layers (see Figure 2.6). Sense wires in each super-layer form a cell with tilt angle 45 degrees with respect to the radial direction. Potential wire cells interleaved with sense wire cells have same tilt angle. In five of these super-layers, the axial super-layers, the wires are parallel to the beam axis. Each cell of the axial super-layer contains twelve sense wires. The axial super-layers are interleaved with four stereo super-layers, in which the wires make $\pm 3^\circ$ angle with respect to the beam

axis. Each cell of the stereo super-layer contains six sense wires.

Leading electrons drift into the azimuthal direction with a maximum drift distance being less than 40 mm, corresponding to a drift time of 800 ns. The axial super-layer signals give a picture of the event in r-ϕ plane. The stereo super-layer signals give a picture of the event in r-z plane. The CTC wire signal passes pre-amplifier and amplifier-shaper-discriminator (ASD), then it is transmitted to FASTBUS TDC card. Tracks pass close at least one sense wire in every super-layer because of large tilt angle of the sense wire cells. These fast wire signals for radial (i.e. high p_T) tracks can be used to generate a fast trigger signal. The hardware track processor, the central fast tracker (CFT), provides a fast trigger signal for a radial track.

The transverse momentum resolution of the CFT track reconstruction is $\delta p_T/p_T = 0.035 p_T$ where p_T is in GeV/c. In the offline track reconstruction using all the nine super-layer hits, the resolution is improved to $\delta p_T/p_T = 0.0017 p_T$. By adding the beam position to the r-ϕ fit of a track, the resolution is improved to $\delta p_T/p_T = 0.0011 p_T$.

2.3.4 Central Calorimeter

The central calorimeter covers a polar angle region of $39° < \theta < 141°$ (i.e. $|\eta| < 1.1$). It is azimuthally segmented into 15° wedges mounted surrounding the solenoid. There are 48 wedges in all, 24 on each side of the $z = 0$ plane. A perspective view of one central calorimeter wedge is shown in Figure 2.7. Each wedge has an electromagnetic calorimetry part and a hadronic calorimetry part. Each wedge is subdivided along the z-axis into ten projective towers, numbered from 0 to 9, where tower 0 is at 90° polar angle. The size of the central tower is approximately 15° in ϕ and 0.11 units in η.

The central calorimeter uses a light wave-length shifter for light collection, which absorbs blue light and emits green light. The light from the scintillator layers is redirected by two light wave-length shifters on two sides up through the light guide into

the two photo-multiplier tubes (PMTs) per tower. The PMT multiplies the green light signal by a factor of 10^5 followed by a charge sensitive amplifier in the RABBIT system [17], a standard analog-signal readout system employed by the CDF.

Central electromagnetic calorimeter

The central electromagnetic calorimeter (CEM) consists of 21-31 layers of 5 mm polystyrene scintillator interleaved with 20-30 layers of 1/8 inch lead [18]. Total thickness of the CEM module is approximately eighteen radiation length, including one radiation length from the solenoid. The CEM has $48\,(\text{wedges}) \times 10\,(\text{towers}) \times 2\,(\text{PMTs}) - 4 = 965$ PMTs to be read out, excluding notched towers for the "chimney" to access the CDF superconducting solenoid. The energy resolution for electrons is well fit by the function [3]:

$$\left(\frac{\sigma}{E}\right)^2 = \left(\frac{13.5\%}{\sqrt{E\sin\theta}}\right)^2 + (1.7\%)^2 \tag{2.3}$$

where E is in GeV and the $\sin\theta$ factor reflects increased sampling thickness seen by electrons entering the calorimeter at an angle.

Proportional strip chamber is embedded between the eighth lead layer and the ninth scintillator layer, near the location of shower maximum. This proportional chamber is referred to as the Central Electromagnetic Strip chamber (CES). It contains 128 strips aligned in ϕ and 64 wires along z-axis. It determines the electron hit position within $\pm 2\,mm$ for 50 GeV/c electrons.

Central and Endwall hadronic calorimeter

The central hadronic calorimeter (CHA) consists of 32 layers of 10 mm plastic scintillator interleaved with 32 layers of 25 mm iron [19]. The endwall hadronic calorimeter (WHA) consists of 15 layers of 10 mm plastic scintillator interleaved with 15 layers of 50 mm iron. Total material thickness is 4.7 units of absorption length for the CHA

and 4.5 units for the WHA. The CHA has 9 projective towers numbered from 0 to 8 along z-axis. The WHA has 6 projective towers numbered from 6 to 11 along z-axis and shadowed by the same numbered tower of the central calorimeter (Figure 2.8).

The CHA has 48(wedges) $\times$ 9(towers) $\times$ 2(PMTs) = 768 PMTs. The energy resolution is approximately $\sigma/E = 80\%/\sqrt{E \sin\theta}$ where E is in GeV.

2.3.5 Plug Calorimeter

The plug calorimeter covers a polar angle region of $10° < \theta < 36°$ (i.e. $1.1 < |\eta| < 2.4$). The plug calorimeter consists of layers of gas proportional chamber made of conductive plastic tubes as sampling medium. Each sampling layer consists of arrays of the proportional tubes. Employing a gas proportional tube allows the operation in strong magnetic field and tolerance to radiation, and achieves good hermeticity and fine granularity. The plug calorimeter is segmented into projective towers, whose size is 5° in ϕ and 0.09 units in η.

One face of the tube array is glued on a PC board with pad patterns and the other face is glued on a PC board for the ground plane. Electric signal is induced on both the anode wire and the cathode pad. Pad signals are gathered within a projective tower and are amplified by a charge sensitive amplifier card called CARROT at the front end of the RABBIT system. The trigger system uses fast-out analog signals fanned out from the charge sensitive amplifier cards.

Plug electromagnetic calorimeter

The plug electromagnetic calorimeter (PEM) consists of 34 layers of gas proportional tubes, numbered 0 to 33 where layer 0 faces the center of the detector, alternated with 34 layers of 2.69 mm thick lead absorber [20]. It closes both ends of the superconducting solenoid leaving a concentric conical hole with an opening angle of 10° with respect

to the beam axis in either direction. The PEM is enclosed in a cylindrical gas vessel, which occupies a volume with an outer diameter of 280.7 cm and a depth of 53 cm between 173 cm and 226 cm in z-coordinate. Total thickness of materials is 18.2 units of radiation length. The module which covers the positive pseudo-rapidity region is named East module and the other module is named West module. One module is divided into four fan-shaped quadrants (Figure 2.9). The quadrants in the west module are named TSW (Top South West), TNW (Top North West), BSW (Bottom South West) and BNW (Bottom North West) in order where the quadrant TSW covers from 0° to 90° in azimuthal angle. The quadrants in the east module are named TSE, TNE, BSE and BNE in order where quadrant TSE is at 0° azimuthal angle. One quadrant is segmented into 18 towers in azimuthal angle and 14 towers in pseudo-rapidity. Each tower is subdivided into three depth segments. The first depth segment contains 0th to 4th layer, the second depth segment contains 5th to 23rd layer and the third depth segment contains 24th to 33rd layer.

The PEM has $14\,(\text{in}\,\eta) \times 72\,(\text{in}\,\phi) \times 3\,(\text{in depth}) \times 2\,(\text{modules}) - 72 \times 2 \times 2 =$ 5760 channels to be read out subtracting nonexistent third segments of two outer annuli. The trigger decision uses the signals from the second depth segments. The 34 signals of anode layers are also read out. They provide a longitudinal picture of the electromagnetic shower development.

The energy resolution for electrons is well fit by the function:

$$\left(\frac{\sigma}{E}\right)^2 = \left(\frac{28.0\%}{\sqrt{E}}\right)^2 + (2\%)^2 \tag{2.4}$$

where E is in GeV. The constant term of 2% is deduced from the invariant-mass width measurement of Z bosons assuming the resolution of $28.0\%/\sqrt{E}$ and the Z mass width of 3.8 GeV [3].

For the 6th-15th layer, strip electrodes are etched in place of the ground plane. This

strip chamber is referred to as the Plug Electromagnetic Strip chamber (PES). The PES covers from 1.2 to 1.84 in pseudo-rapidity. Odd-numbered layers have arc-shaped strips, whose size is 0.02 units in pseudo-rapidity and 30 degrees in azimuthal angle. Even-numbered layers have radial strips, whose size is 0.64 in pseudo-rapidity and 1 degree in azimuthal angle. Strip signals are merged among odd-numbered layers and even-numbered layers.

Plug hadronic calorimeter

The plug hadronic calorimeter (PHA) has 20 layers of gas proportional tubes interleaved with 20 layers of 50.0 mm thick steel absorber. The PHA is enclosed in a gas vessel, which has an outer concentric conical wall with an opening angle of 30° and an inner concentric conical wall with an opening angle of 10° with respect to the beam axis. It is placed behind the plug electromagnetic calorimeter module. Total thickness of materials is 6.5 units of absorption length. One PHA module consists of 12 fan-shaped stacks, whose size is 30 degrees in azimuthal angle. Each stack is segmented into 6 towers in azimuthal angle and 14 towers in pseudo-rapidity.

Pad signals of 20 layers are merged into one signal of a projective tower. The PHA has $12\,(\text{in}\,\eta) \times 72\,(\text{in}\,\phi) \times 2\,(\text{modules}) = 1728$ channels to be read out. The energy resolution for jets is approximately $\sigma/E = 120\%/\sqrt{E}$ where E is in GeV.

2.3.6 Forward Calorimeter

The forward calorimeter covers a polar angle range of $2° < \theta < 10°$ (i.e. $2.2 < \eta < 3.4$). It is placed 6.5 m away from the center of the detector along the beam axis on both sides. The forward calorimeter consists of layers of gas proportional chambers as sampling medium. The forward calorimeter module is segmented into projective towers, whose size is 5° in ϕ and 0.1 units in η. The forward electromagnetic

calorimeter (FEM) has 30 sampling layers interleaved with 30 lead layers of 0.8 units radiation length [21]. Total thickness is 25.5 units of radiation length. The FEM has $20\,(\text{in}\ \eta) \times 72\,(\text{in}\ \phi) \times 2\,(\text{depths}) \times 2\,(\text{ends}) = 5760$ channels to be read out. The energy resolution for electrons is well fit by the function: $\sigma/E = 25\%/\sqrt{E} + 0.5\%$.

The forward hadronic calorimeter (FHA) has 27 sampling layers alternated with 27 lead layers of 51 mm iron plate [22]. The FHA has $20\,(\text{in}\ \eta) \times 72\,(\text{in}\ \phi) \times 2\,(\text{ends}) = 2880$ channels to be read out. The energy resolution is approximately $\sigma/E = 120\%/\sqrt{E}$.

2.3.7 Central muon detector

The central muon detector (CMU) is embedded in the central calorimeter wedge locating after the central hadron calorimeter of 4.9 units of absorption length at 3.47 m away from the beam axis [23]. The CMU is segmented into three modules of 4.2° in azimuthal angle. Each of the three modules in a wedge consists of four layers of four rectangular drift cells. Each module is 2260 mm long along the beam axis covering a pseudo-rapidity region of $|\eta| < 0.63$. Cross section of a module of the central muon chamber is shown in Figure 2.10.

The signals are read out by the muon TDC card [24] in the RABBIT system. The timing signal is sent to the level 1 trigger card sitting in the same RABBIT crate. The signal location in z-coordinate is also provided by a charge division method.

The position resolution is 250 μm in azimuthal direction and 1.2 mm along the sense wire in one sigma.

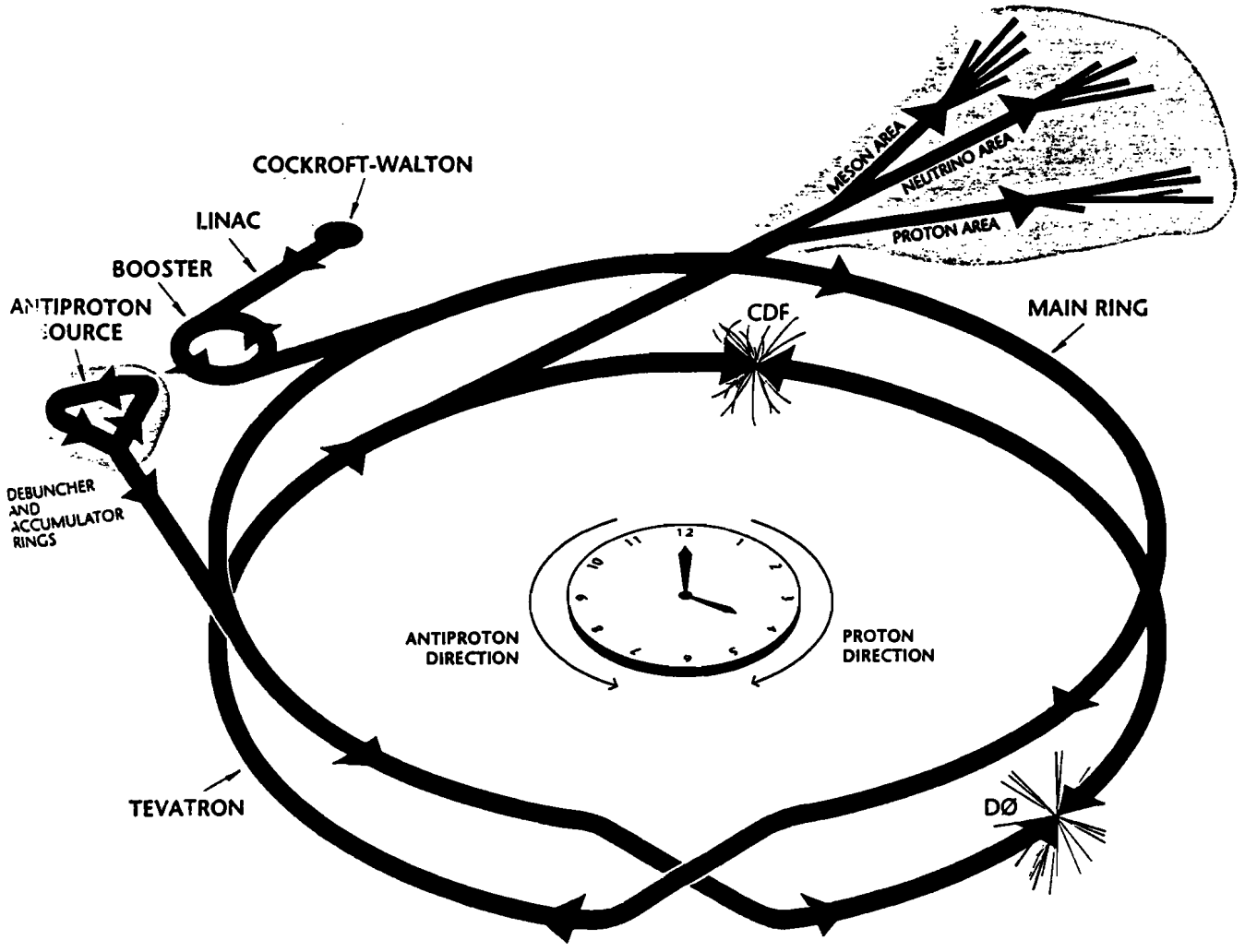

Figure 2.1: Perspective view of the Tevatron proton-antiproton collider at Fermi national accelerator laboratory.

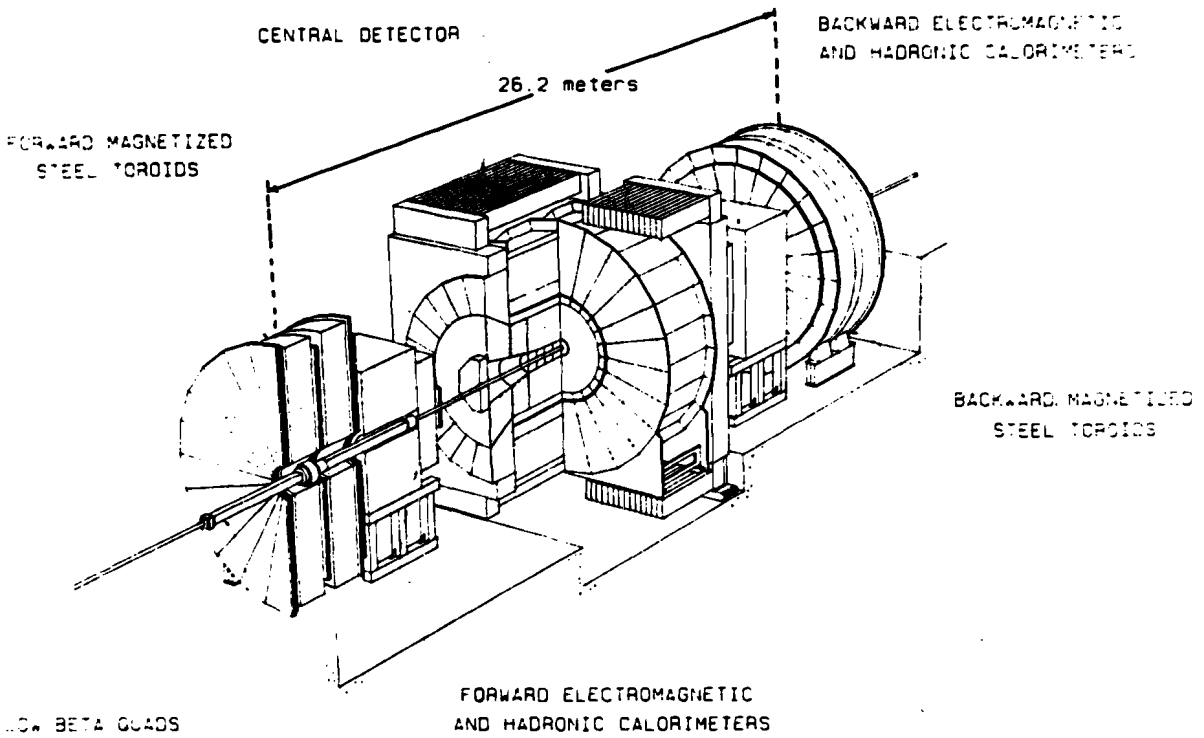

Figure 2.2: Perspective view of the Collider Detector at Fermilab.

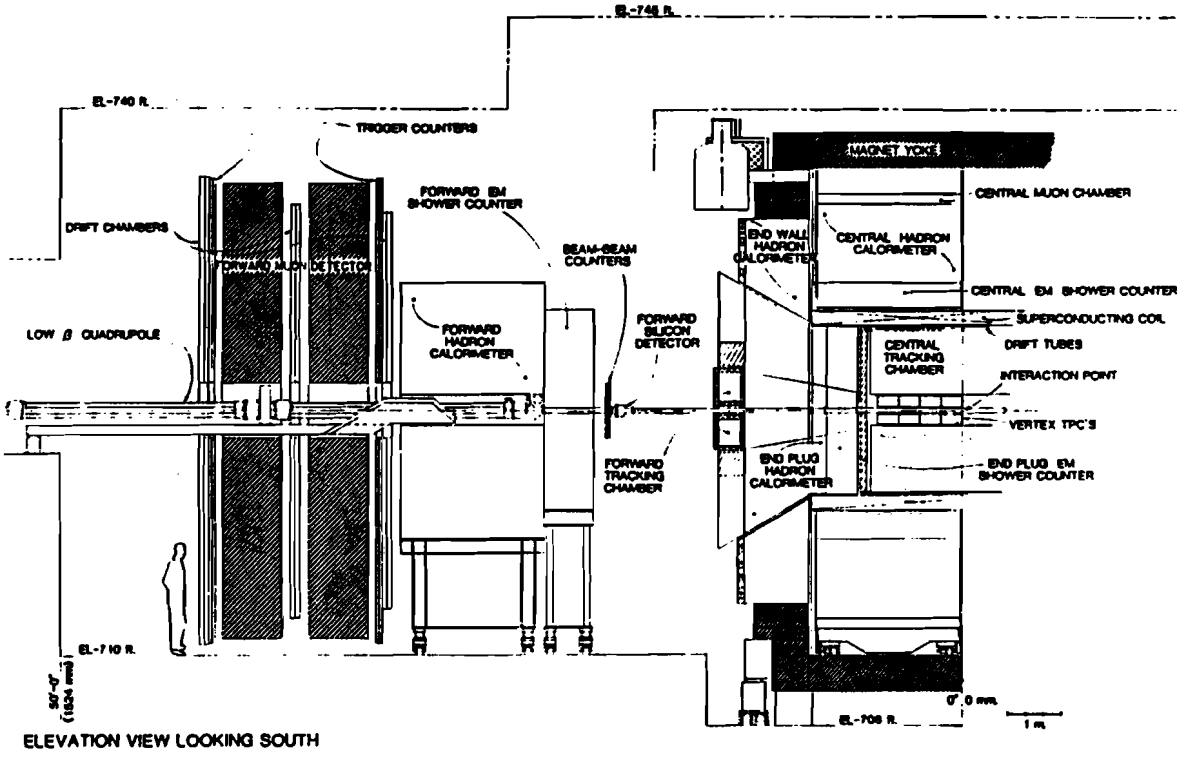

Figure 2.3: Cut-away view through the forward half of CDF. The detector is forward-backward symmetric about the interaction point.

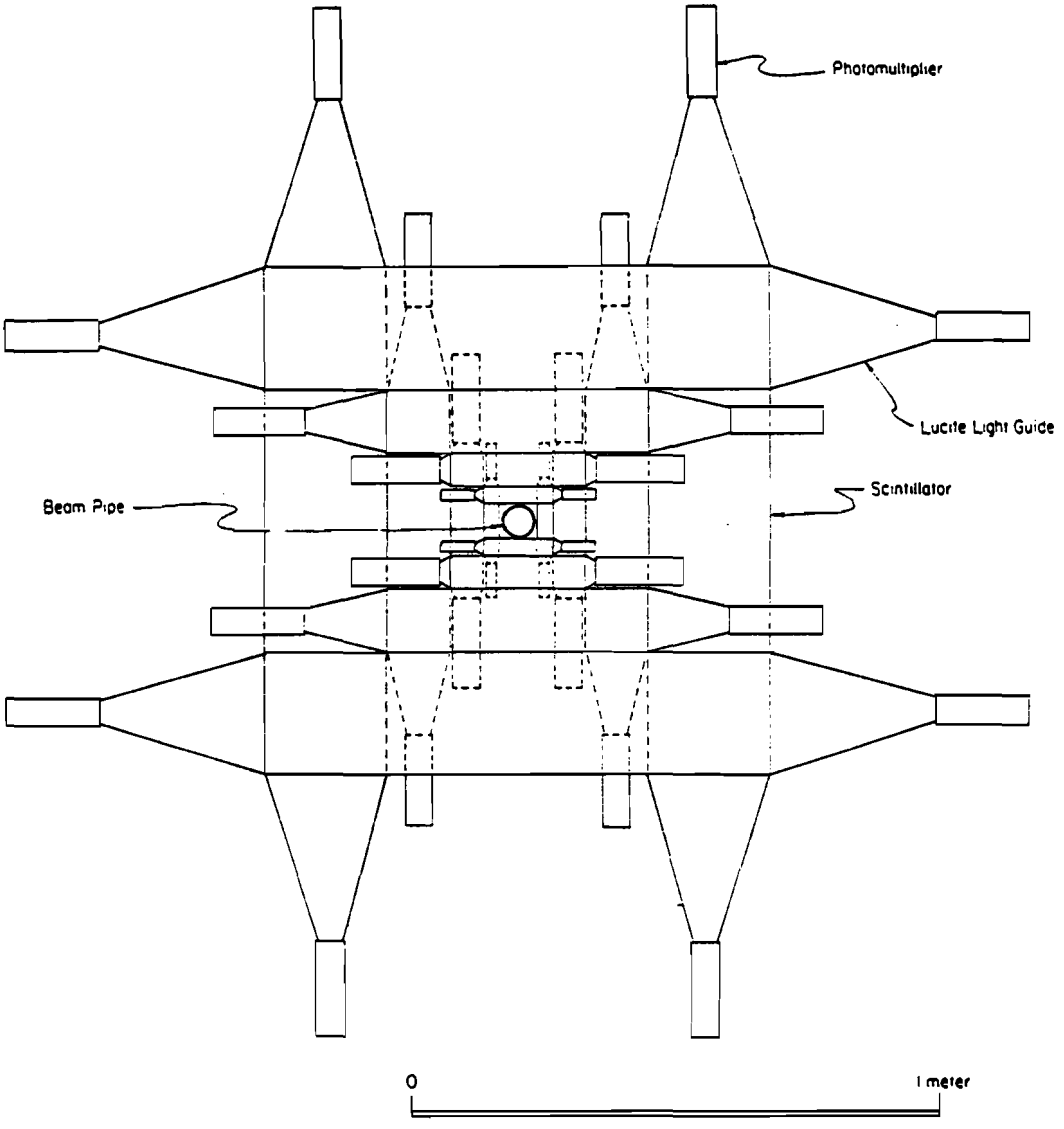

Figure 2.4: Beam's-eye view of one of the beam-beam counter planes.

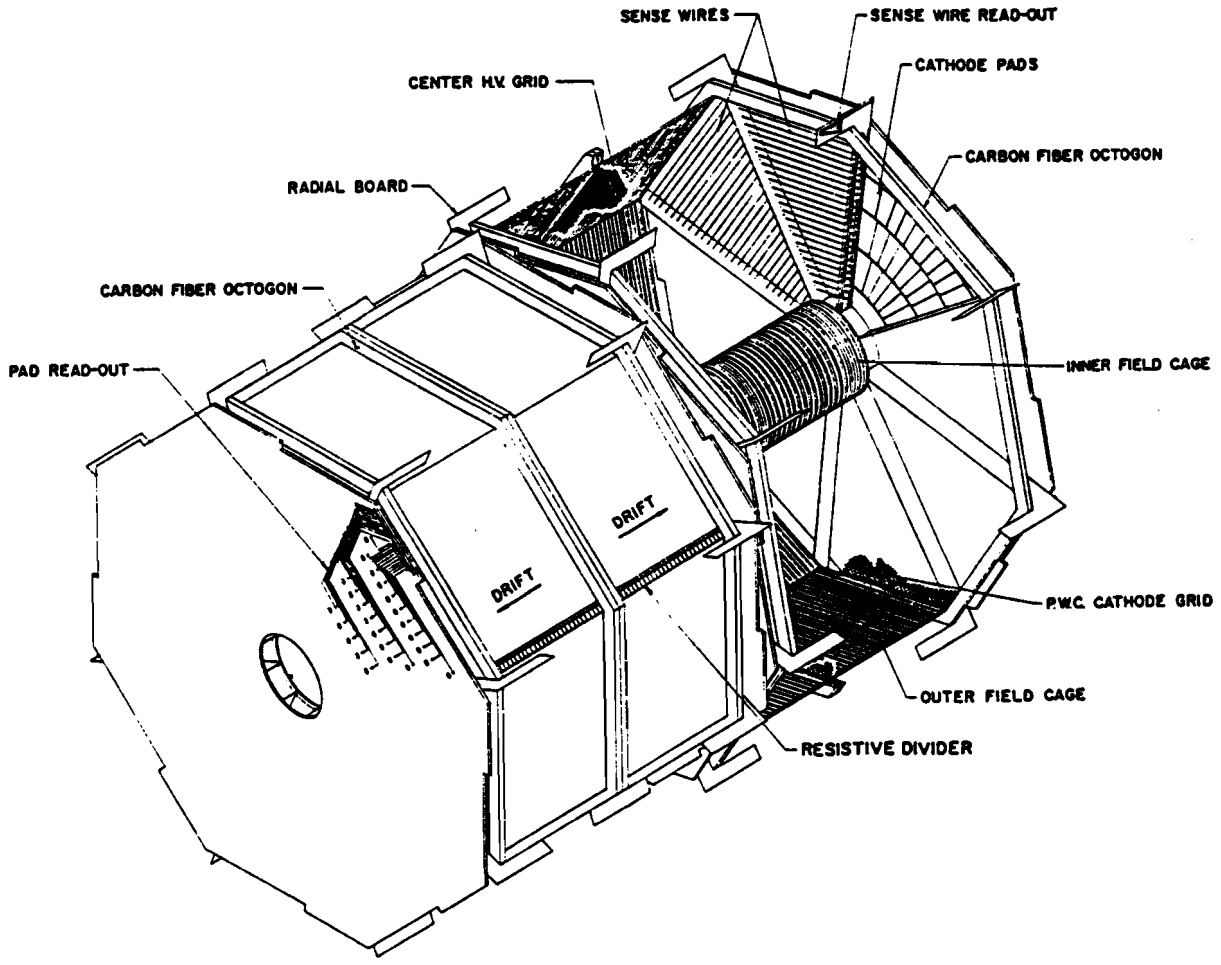

Figure 2.5: Isometric view of two VTPC modules. They are rotated in ϕ by 11.3° with respect to each other.

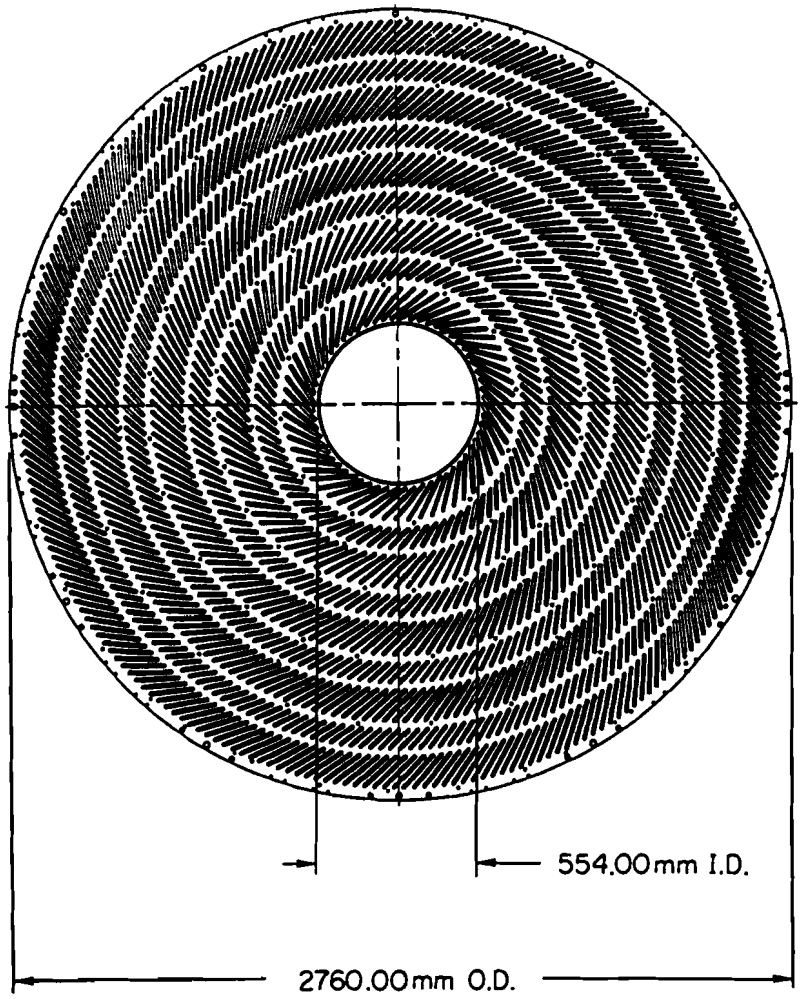

Figure 2.6: End view of the Central Tracking Chamber showing the location of the slots in the aluminum end-plates.

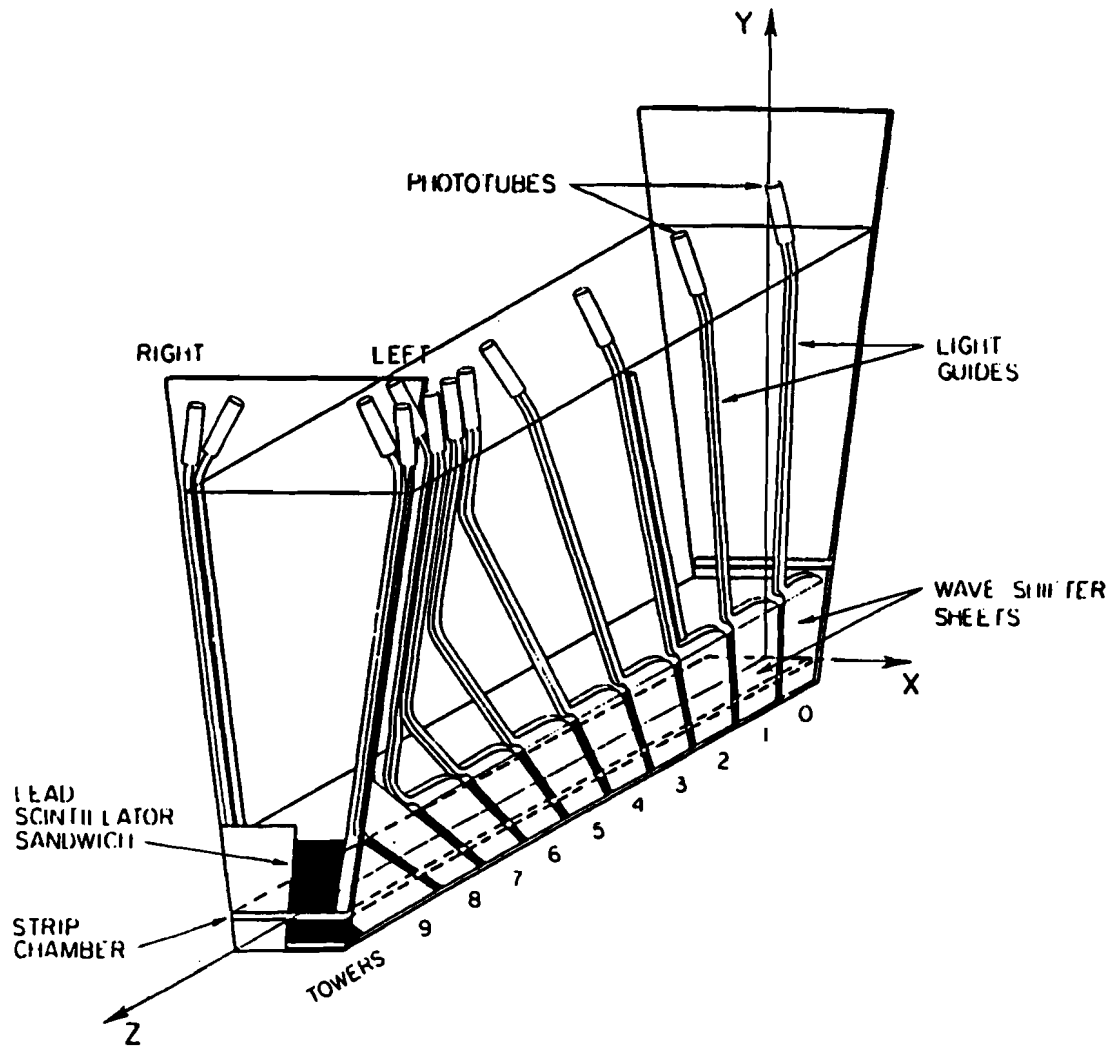

Figure 2.7: A central calorimeter wedge, showing the layout of the light-gathering system.

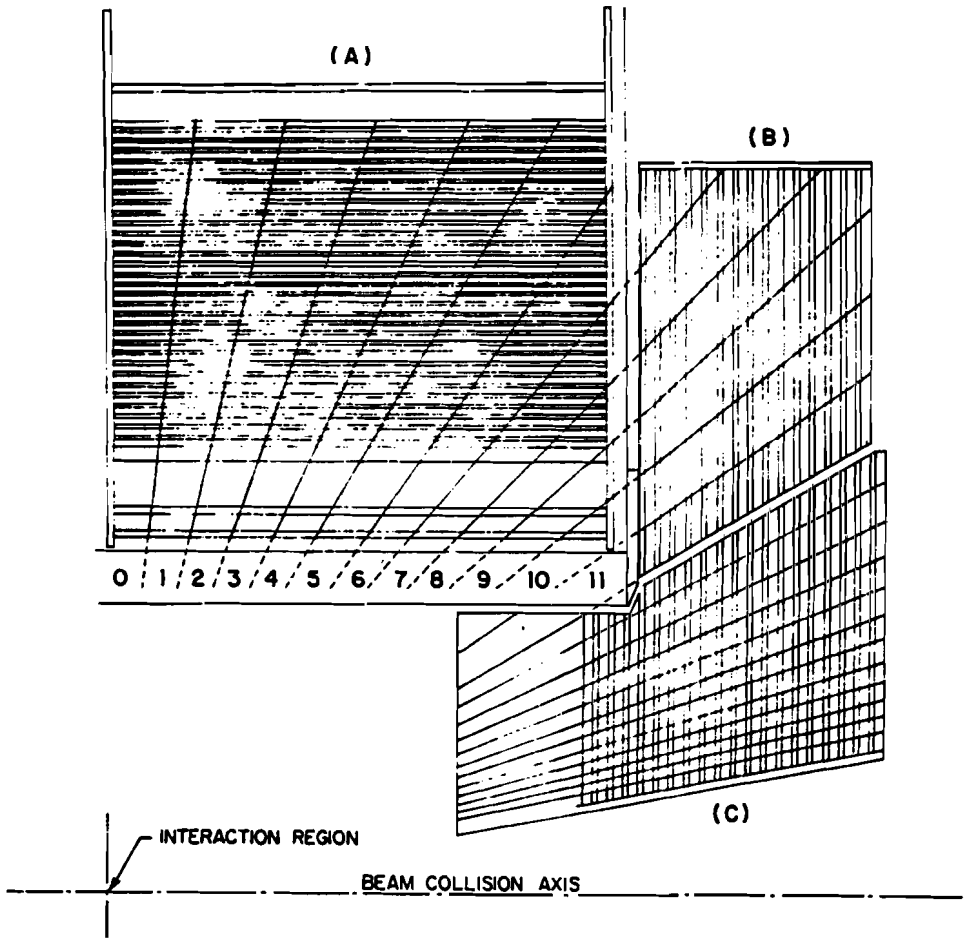

Figure 2.8: Quadrant of the calorimeter where A, B, C show central, endwall and endplug respectively. Towers are numbered from 0 (at 90° in polar direction)to 11(last tower of endwall modules). Hadronic towers 6,7 and 8 are shared between central and endwall calorimeter.

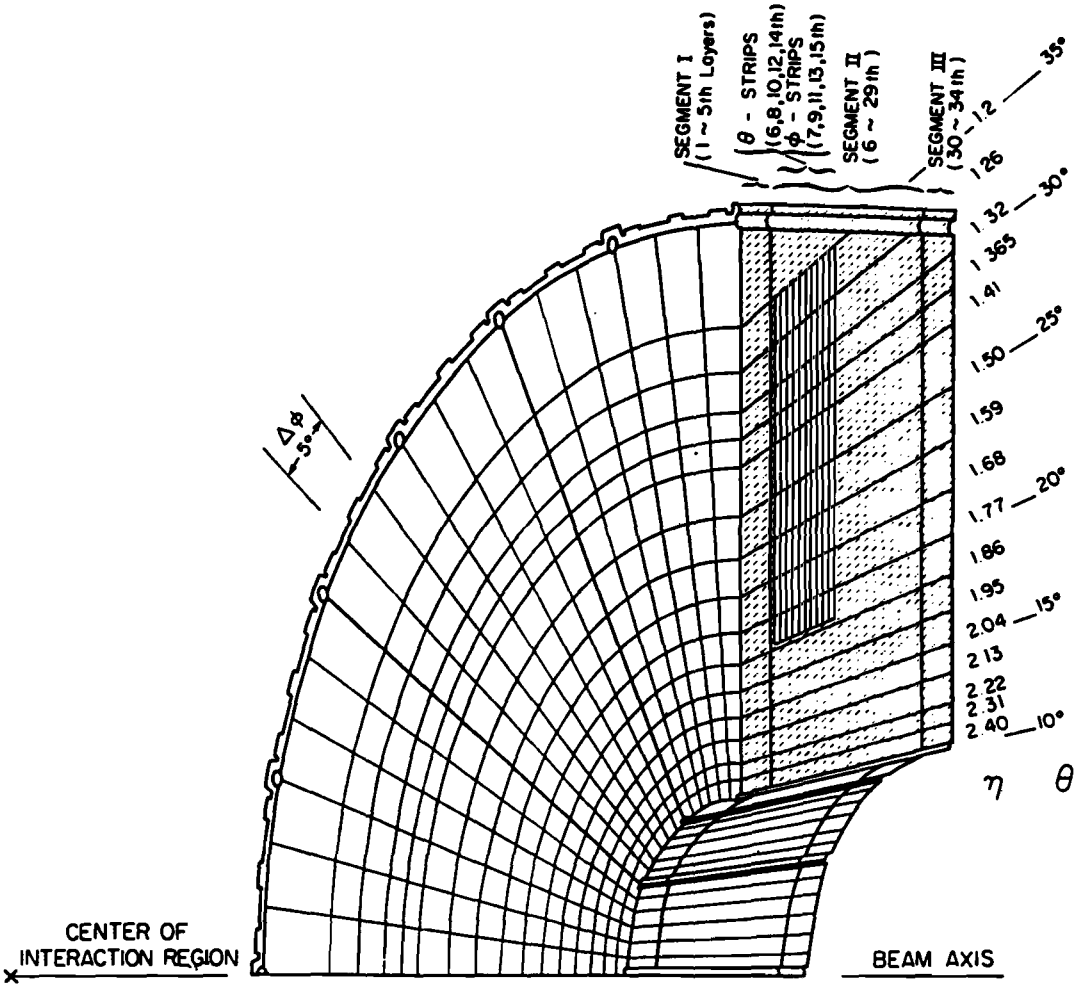

Figure 2.9: Isometric view of a quadrant of the plug electromagnetic calorimeter, showing the projective pad tower structure and the longitudinal layers.

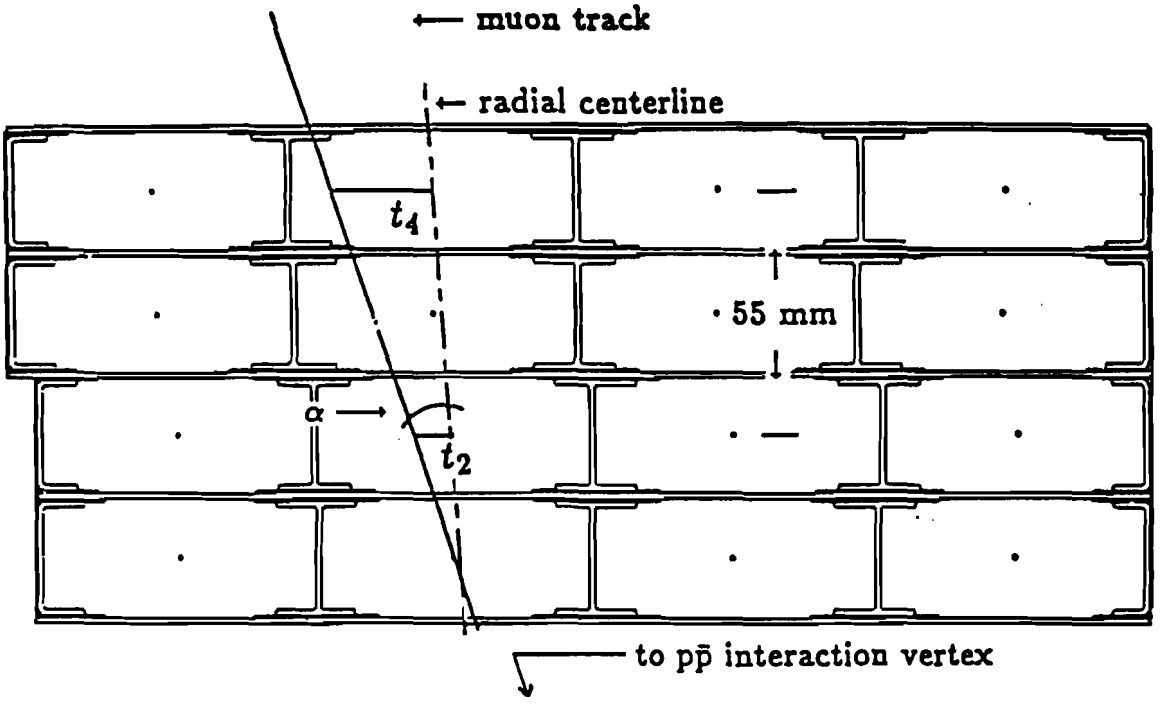

Figure 2.10: Cross section of a single muon chamber, showing drift times t_i and the track angle α.

Chapter 3

Common data sets

Proton anti-proton collision data are collected by the trigger system and recorded on the nine-track tapes. On-line data acquisition is described in Section 3.1. Following that, off-line data reconstruction is described in Section 3.2.

3.1 Data acquisition

In the Tevatron a proton bunch and an anti-proton bunch is crossing every 3.5 μsec or at a rate of 300 kHz. The proton and anti-proton cross section is measured to be (71.5 ± 5.0) mb [12]. It is composed of 55 mb of the inelastic cross section and 16.5 mb of the elastic cross section. Out of 55 mb, 46.8 mb is an effective cross section measured by the beam-beam counters which was described in Section 2.3.1. At a luminosity of $10^{30}\,\mathrm{cm}^{-2}\mathrm{s}^{-1}$, proton and anti-proton interactions occur at a rate of (71.5 ± 5.0) kHz and 46.8 kHz is triggered by the BBC. The rate at which events can be written to magnetic tape is around 1 Hz. The trigger system selects the events of physics interest and reduces the rate of the data to tape. The CDF employs four levels of trigger stage, numbered 0 to 3.

3.1.1 Level 0

The level 0 trigger initiates data aquisition by a coincidence between the east and west beam-beam counters. This is the minimum-bias trigger described in Section 2.3.1. The level 0 trigger outputs trigger signals at a rate of 20 to 40 kHz. If the level 0 trigger accepts an event, data taking is inhibited during the next beam crossing, 3.5 μs later.

3.1.2 Level 1

The level 1-2 triggers use fast fan-out signals from the front-end amplifiers in the RABBIT system. Those signals are the calorimetry signals merged into trigger tower cells and the muon TDC signals [24]. The momentum information from the hardware track processor, the Central Fast Tracker (CFT) [25], is also used. The decision is made by a hardware trigger processor.

The size of a trigger cell is 15° in azimuthal angle and 0.2 units in pseudo-rapidity; it groups two towers in the central calorimeter and six towers in the plug and forward calorimeters. The energy E of each trigger cell is converted to the transverse energy E_{T} by weighting with $\sin\theta$: $E_{\mathrm{T}} \equiv E \sin\theta$, where θ is the polar-angle of the cell centroid with respect to the center of the detector (i.e. z=0). The processor separately computes electromagnetic and total (electromagnetic + hadronic) transverse energy sums over trigger cells above a programmable threshold. The processor also computes six E_{T} sums over trigger cells belong to six calorimeter sections, those are, the east and west central calorimeters, the east and west plug calorimeters and the east and west forward calorimeters. These are named crate sum E_{T} because each calorimeter section belongs to one FASTBUS crate.

The angle α between a trajectory in the muon detector and a reference plane containing beam axis, is related to the curvature of the track in the magnetic field, and hence to its transverse momentum (see Figure 2.10). For a small angle α, it is approx-

imately given as follows:

$$\alpha \approx \frac{126\,\mathrm{mrad} \cdot \mathrm{GeV}/c}{p_{\mathrm{T}}}. \tag{3.1}$$

The muon trigger processor identifies muon trajectories in the muon detector and estimates their transverse momentum, using muon TDC signals.

The CFT identifies prompt axial hits in the CTC and compares them with predetermined hit patterns in a look-up table. At level 1, it signals the presence of a track with a transverse momentum above a programmable threshold.

3.1.3 Level 2

The rate of level 1 output going into level 2 is of the order of 1 kHz. The trigger processor identifies clusters of calorimeter energy and computes their electromagnetic and total transverse energy, their centroid position and their width and also p_{T} of tracks pointing to them [26]. It also identifies the CFT tracks pointing to the trajectories in the muon detector formed in the level 1 trigger. The level 2 trigger decision is based on a coarse identification of physical objects such as electrons, muons, tau leptons, photons, neutrino's and jets. The trigger accepts the event if either of those objects are identified.

Electrons, for instance, are selected on the basis of their transverse energy and width of the calorimetry cluster, their ratio of electromagnetic to hadronic energy deposition. For the central electrons, the presence of a high p_{T} CFT track pointing to the cluster is also required. Muons are selected on the basis of the presence of a track in the muon detector and, optionally, the amount of energy deposited in the associated calorimeter cell.

If the level 2 trigger accepts an event, it initiates an analog-to-digital conversion process of the entire analog signals, which is handled by the EWE modules in the RABBIT system [17]. This takes about 1 ms.

3.1.4 Level 3

Output rate of the level 2 into the level 3 is a few Hz. At the level 3, all the digitized data for a given event is available. The level 3 trigger system is a farm of parallel processors capable of executing algorithms written in FORTRAN [27]. It identifies physical objects in more sophisticated way, which is equivalent to the way used in the offline reconstruction described in Section 3.2. The electron and muon identification parameters, described in Section 4.1, are available in the level 3. The level 3 rejects approximately 50% of the events processed.

3.2 Reconstrucion of the data

The events recorded on raw data tapes consist of the run conditions, the trigger information, and the detector signal information. Most of the physics parameters used in the off-line analysis are calculated and stored in bank-formatted data. Reconstruction process is controlled by "Analysis Control", which enable us to build a tree of the offline program modules. Elements of the event properties described in the following sub-sections are reconstructed in corresponding program modules. Raw and reconstructed data are recorded on new data tapes.

3.2.1 Event vertex

The event vertex position in z-coordinate is measured by the vertex time projection chamber (VTPC), which is described in Section 2.3.2. All of the two-dimensional tracks in r-z plane view are reconstructed as the first step of the event reconstruction. The event vertex in z-coordinate is found as the point of convergence of all the reconstructed VTPC tracks in the event. Collision points thus determined and showed a Gaussian distribution with a sigma of 35 cm.

3.2.2 Tracks

The tracks in the central tracking chamber (CTC) are reconstructed using all the hits in axial super-layers and stereo super-layers. The CTC was described in Section 2.3.3. The CTC tracks are identified by pattern recognition processes. Most of the radial tracks (i.e. high p_T) are reconstructed as three-dimensional tracks, which have azimuthal and polar angle information. The CTC track data bank contains the azimuthal and polar angle information, the curvature and the impact parameter for every reconstructed tracks, where the impact parameter is defined as the closest distance from the track to the beam axis in r-ϕ plane. The momentum resolution is $\delta p_T/p_T = 0.0017 p_T\,(\mathrm{GeV}/c)$ using all the nine super-layer hits. By adding the beam position constrained to the r-ϕ fit of a track, the resolution is improved to $\delta p_T/p_T = 0.0011 p_T\,(\mathrm{GeV}/c)$.

In this analysis, the small polar angle tracks pointing to a pseudo-rapidity range of $1.32 < |\eta| < 1.6$ are used for the electron identification in the plug region. For the track which pass the first three super-layers (i.e. $1.32 < |\eta| < 1.6$), the transverse momentum resolution is $\delta p_T/p_T = 0.005 p_T\,(\mathrm{GeV}/c)$ with the beam position constrained fit.

3.2.3 Calorimeter towers

The calorimeter tower signals are converted to energy using the constants determined in the test beam. Detector-noise signals are removed during the conversion. The size of a calorimeter tower is 15° in azimuthal angle and 0.1 units in pseudo-rapidity for the central calorimeter, and 5° in azimuthal angle and 0.09 units in pseudo-rapidity for the plug and forward calorimeters. The polar-angle positions of the calorimeter towers are determined with respect to the event vertex position in z-coordinate. The transverse energy of each calorimeter cell is calculated as $E_T \equiv E \sin\theta$, where E is the energy of the calorimeter tower and θ is the polar-angle of the tower centroid with respect

to the measured event vertex measured by the VTPC. The electromagnetic tower centroid is taken halfway in the two detector polar angles of the tower boundaries at the depth of ten radiation length (i.e. shower maximum). The hadronic tower centroid is taken halfway in the two detector polar angles of the tower boundaries at the depth of three absorption length. The calorimeter tower bank contains the electromagnetic and hadronic transverse energy for every calorimeter tower.

3.2.4 Missing transverse energy

The missing transverse energy vector ($\vec{\not{E}}_{\mathrm{T}}$) is defined as minus the sum of transverse energies deposited in calorimetry towers over the pseudo-rapidity range $|\eta| < 3.6$:

$$\vec{\not{E}}_{\mathrm{T}} \equiv -\sum_{tower} \vec{E}_{\mathrm{T}}^{\,tower} \tag{3.2}$$

where $\vec{E}_{\mathrm{T}}^{\,tower}$ is two-dimensional vector pointing from the event vertex to the tower centroid. For a tower included in the sum, its energy content must be above a given threshold. The threshold is 0.1 GeV in the central electromagnetic and hadronic calorimeters, 0.3 GeV in the plug electromagnetic calorimeter, 0.5 GeV in the plug hadronic and forward electromagnetic calorimeters, and 0.8 GeV in the forward hadronic calorimeter. These thresholds are in energy, not in transverse energy. The data bank of the missing transverse energy contains x-y components of the missing transverse energy, the scalar sum of the transverse energy.

The resolution of the missing transverse energy measurement is approximated by a constant times a square root of the total scalar transverse energy observed in the event. The resolution over the range of $\sum |\vec{E}_{\mathrm{T}}|$ covered by the W decay candidates is

written as follows [2]:

$$\sigma(\not{E}_{\mathrm{T}\ x,y}) = (0.47 \pm 0.03)\sqrt{\sum |\vec{E}_{\mathrm{T}}|}(GeV^{1/2}) \tag{3.3}$$

where $\not{E}_{\mathrm{T}\ x,y}$ are x and y components of the missing transverse energy.

In $W \rightarrow e\nu$ events, the transverse energy of the underlying event, the calorimeter activity except for the electron, is measured as follows:

$$\vec{E_{\mathrm{T}}}^{UL} = \sum_{tower} \vec{E_{\mathrm{T}}}^{tower} - \vec{E_{\mathrm{T}}}^{ele} \tag{3.4}$$

where $\vec{E_{\mathrm{T}}}^{UL}$ denotes the transverse energy vector of the underlying event and $\vec{E_{\mathrm{T}}}^{ele}$ denotes the transverse energy of the electron. In order to compensate for nonlinearities in the calorimeter energy response for low energy hadrons, we multiply $\vec{E_{\mathrm{T}}}^{UL}$ by a factor of 1.4 [2]. The missing transverse energy is recalculated using the corrected $\vec{E_{\mathrm{T}}}^{UL}$:

$$\vec{\not{E}_{\mathrm{T}}}^{corr} = -(1.4\vec{E_{\mathrm{T}}}^{UL} + \vec{E_{\mathrm{T}}}^{ele}). \tag{3.5}$$

3.2.5 Electromagnetic calorimeter clusters

The energetic clusters are identified in the calorimetry tower bank. A clustering algorithm looks for seed towers containing at least 3 GeV of transverse energy. The neighboring towers are added to the corresponding cluster if their transverse energy is greater than 0.1 GeV. In the central region, the clustering algorithm is restricted within one wedge, that is, it is not applied beyond the azimuthal boundary, because the electromagnetic shower does not spread across the ϕ boundary. The maximum electromagnetic cluster size is 3×1 towers in the central region, 5×5 towers in the plug, and 7×7 towers in the forward region.

For the electromagnetic cluster, the transverse energy of the cluster is required to be

greater than 5 GeV, and the ratio of the hadronic to electromagnetic transverse energy is to be less than 0.125. The transverse energy of the cluster and the cluster centroid are written in the electromagnetic cluster bank. These clusters contain electrons, photons, and neutral pions.

The electron identification parameters, described in Section 4.1, are calculated and stored in the electron object bank. The electron identification algorithm also finds the three-dimensional CTC track pointing to the cluster. The track information is also written in the electron object bank.

3.2.6 Jets

Jets are identified in the calorimeter tower bank by finding seed towers, forming pre-clusters, and finally arbitrating overlap regions between clusters. The clustering algorithm starts by listing all the seed towers, the towers above a transverse energy threshold of 1 GeV. Seed towers adjacent to each other, either at a corner or on a side, are grouped into pre-clusters. This is done in such a way that in any pre-cluster, tower E_{T}'s are monotonically decreasing as one moves from the highest E_{T} tower to the edge of the pre-cluster.

Pre-clusters are expanded into the clusters by a fixed cone iterative algorithm. It computes the E_{T} weighted η-ϕ centroid of the pre-clusters. A cluster is defined as the set of towers containing more than 100 MeV of E_{T}, and within an η-ϕ radius of 0.7 from the centroid. The cluster centroid is recomputed, and its set of towers redefined accordingly. This process is repeated until the set of towers no longer changes. The initial pre-cluster towers are always kept in the cluster regardless of their distance to the centroid. This prevents the centroid from shifting too far away in pathological situations.

If a cluster is completely contained in another cluster, the cluser with the smaller

energy is dropped. If two clusters share a subset of towers, they are merged if the total E_T in the common towers is more than 75% of the E_T in the smaller cluster. Otherwise, the towers in the overlap region are divided between the two clusters according to their proximity to the cluster centroids. The centroids are subsequently recomputed, and disputed towers reassigned, until a stable configuration is reached.

The jet object bank contains the jet transverse energy, the centroid of the cluster and the electromagnetic energy fraction to the total energy (E_{EM}/E_{Tot}).

3.2.7 Muons

The momentum of a muon is determined from the CTC track which matches best with the track segment in the muon detector. The muon identification algorithm search the best CTC track. In order to reduce contamination to the prompt muons by cosmic rays and by muons coming from decays in flight of kaons and pions, the CTC track is required to pass close to the event vertex. The algorithm also calculates the muon identification parameters, those are, the position matching parameters between the muon detector signal and the CTC track, the energy deposition in the calorimeter tower where the muon track points. The parameter values and the three-momentum of muons are written in the muon object bank.

3.3 Reconstructed data tapes

The CDF group provided two types of reconstructed data tape. One was an express process named *Spin Cycle* and the other one was named *Full Production* where all the raw data were reprocessed. In the *Spin Cycle*, the events were pre-selected on the basis of the level 2 trigger information. As described in Section 3.1.3, a coarse identification of physical objects is performed on the level 2 trigger. The trigger data bank has the information of which trigger requirement the event has been passed. For the inclusive

electron sample, for instance, the events fired by the electron triggers were selected. The *Spin Cycle* data were used for a fast analysis.

In either of the two reconstruction processes, the number of events were reduced by a final identification of physical objects. A reconstruction process contains several parallel streams of event reconstruction. Either of the streams have specific event filters, which produce specific event samples. Those are the inclusive lepton and photon samples, the missing E_T sample, the inclusive jet sample, etc. The CDF recorded about 5500 nine-track tapes of raw data. Either of the reconstruction streams produced 100 to 1000 nine-track tapes depending on the event samples. The inclusive central electron sample is about 170 tapes and the inclusive plug electron sample is about 140 tapes.

Chapter 4

Event selection

The Central W sample, which had an electron in the central region, was selected from the inclusive electron sample of the *Spin Cycle*. The plug W sample, which had an electron in the plug region, was selected from the inclusive electron sample of the *Full Production*. The *Spin Cycle* and the *Full Production* were described in Section 3.3.

4.1 Particle identification parameters

Electron in the $W \rightarrow e\nu$ decay is identified using the parameters described below. Most of the identification parameters are available in the electron object bank described in Section 3.2.5. The threshold values are determined to keep the lepton finding efficiency more than 90% and keep the background contamination minimum. The CDF identifies electrons using information of their shower profile and the associated track.

Isolation

Most of electrons in $W \rightarrow e\nu$ decays are isolated from other activities in $\bar{p}p$ collisions.

The isolation variable $Iso(R)$ is defined as

$$Iso(R) = \frac{E_{\mathrm{T}}(R) - E_{\mathrm{T}}^{cl}}{E_{\mathrm{T}}^{cl}} \tag{4.1}$$

where $E_{\mathrm{T}}(R)$ denotes a sum of electromagnetic and hadronic transverse energy within a cone radius R from the cluster centroid defined in η-ϕ plane and E_{T}^{cl} denotes the transverse energy of the electron cluster. Misidentified electrons fragmented from QCD jets and electrons from semi-leptonic decays of heavy quarks are not isolated (i.e., they have large $Iso(R)$). The isolation variable is used to estimate these backgrounds (see Section 6.1). We set a threshold value $Iso(R) < 0.1$ for $R = 0.4$ in order to supress the background contamination with keeping high efficiency for electrons from W decay.

4.1.1 Central electron parameters

Electron identification parameters in the central region are described below.

Lateral shower profile

Electrons develop compact shower in a dense material while QCD jets fragment broadly and leave broad shower signal. The lateral sharing of energy between the calorimeter towers gives a criterion to identify electrons. For the central electrons, we use a parameter $Lshr$ to describe the energy sharing among adjacent towers in a wedge. The $Lshr$ is defined as follows:

$$Lshr \equiv 0.14 * \sum_i \frac{E_i^{meas} - E_i^{pred}}{\sqrt{0.14^2 * E^{cl} + (\Delta E_i^{pred})^2}} \tag{4.2}$$

where the sum runs over the two towers adjacent to the seed tower in the same azimuthal wedge, E_i^{meas} is the energy deposition in tower i, E_i^{pred} is the energy expected in tower i, and E^{cl} is the cluster energy. The expected energy is calculated from test-beam

measurements. The denominator represents a normalization that takes into account the finite resolution ($0.14\sqrt{E}$) of the CEM energy measurement. The ***Lshr*** depends on the seed tower energy and the shower impact point in the strip chamber. The energy fluctuation ΔE_i^{pred}, therefore, contains the error in E_i^{meas} associated with a 1 cm error in the measurement of shower impact point and also the error of the fractional energy measurement. A distribution of ***Lshr*** for electrons from $W \rightarrow e\nu$ decays is shown in Figure 4.1.

As described in Section 2.3.4, the gas strip chamber (CES) is embedded at the shower maximum in the central electromagnetic calorimeter. The CES determines the shower centroid and qualifies the cleanliness of electron signal. The lateral shower profiles across the strips and the wires are separately fitted to parameterizations derived from 50 GeV/c test-beam electron data. In the strip view, for instance, the fitting procedure obtains the z-coordinate of the shower centroid, $Z_{\rm CES}$, and the strip cluster energy E by minimizing the function:

$$\chi^2(z,E) \equiv \sum_{i=1}^{n} \frac{(E_i^{meas} - Eq_i^{pred}(z))^2}{\sigma_i^2(z)} \tag{4.3}$$

where the sum extends over $n = 11$ channels, E_i^{meas} is the measured energy in channel i, $q_i^{pred}(z)$ is predicted fractional energy in channel i normalized to 1, E is the strip cluster energy. Fluctuations in a single channel response are taken as

$$\sigma_i^2(z) = (0.026)^2 + (0.096)^2 q_i^{pred}(z), \tag{4.4}$$

which has been obtained from 10 GeV/c test-beam electron data.

In order to test a single electron or single photon hypothesis, we introduces the variable:

$$\chi^2_{strip} \equiv \sum_{i=1}^{n} \frac{1}{4} \left(\frac{E_{\rm CEM}}{10}\right)^{0.747} \frac{(q_i^{meas} - q_i^{pred}(Z_{\rm CES}))^2}{\sigma_i^2(Z_{\rm CES})} \tag{4.5}$$

where q_i^{meas} is the measured strip fractional energy in channel i normalized to 1 and $E_{\rm CEM}$ is the cluster energy measured by the central electromagnetic calorimeter. Since the energy resolution and the location of shower maximum both vary with energy, the variance of single channel response (i.e. σ_i^2) shows energy dependence. The $E_{\rm CEM}$-dependent factor in front of the sum compensates this energy dependence of σ_i^2. A distribution of χ^2_{strip} for electrons from $W \rightarrow e\nu$ decays is shown in Figure 4.2.

The shower profile in the wire view is treated analogously to that in the strip view. It consists in calculating the local x-coordinate, $X_{\rm CES}$, of the shower centroid and the corresponding goodness of fit variable χ^2_{wire}.

Longitudinal shower profile

Hadrons leave large energy deposition in the hadronic calorimeter, while electron showers are mostly confined within the electromagnetic calorimeter. The energy deposition in the hadronic calorimeter behind the electron cluster is measured. Its ratio to the electron cluster energy, $E_{\rm Had}/E_{\rm EM}$, gives a criterion to distinguish electrons from hadrons. In the central region, $E_{\rm Had}/E_{\rm EM}$ has slight energy dependence because total material thickness is relatively thin ($18X_0$). We use an energy-dependent threshold:

$$E_{\rm Had}/E_{\rm EM} < 0.055 + 0.045 \times E/(100\,{\rm GeV}) \tag{4.6}$$

where E is the electromagnetic cluster energy. A distribution of $E_{\rm Had}/E_{\rm EM}$ for electrons from $W \rightarrow e\nu$ decays is shown in Figure 4.3 togather with a distribution for backgrounds.

Track

Neutral pions and photons, which are mostly produced by QCD processes, leave simi-

lar signals as electrons on the calorimeter. Electron leaves a track in the CTC, which allows the momentum measurement. The ratio of the electron energy to the track momentum, $E/p \equiv E_{\mathrm{T}}/p_{\mathrm{T}}$, gives a criterion to distinguish electrons from hadrons. A distribution of E/p for electrons from $W \rightarrow e\nu$ decays is shown in Figure 4.4.

In order to verify that the electron track points to a region reasonably close to the shower centroid, two matching parameters are used:

$$\Delta X = X_{track} - X_{\mathrm{CES}} \tag{4.7}$$

$$\Delta Z = Z_{track} - Z_{\mathrm{CES}} \tag{4.8}$$

where X_{track} and Z_{track} are the coordinates of the extrapolated position of the track at the radius of the strip chamber, X_{CES} and Z_{CES} are the coordinates of the shower centroid measured by the CES. Distributions of ΔX and ΔZ for electrons from $W \rightarrow e\nu$ decays are shown in Figures 4.5 and 4.6.

The CTC and VTPC track informations are used to identify the electrons from photon conversions. The conversions within the VTPC volume leave tracks in both the VTPC and the CTC. The conversions at the inner wall of the CTC leave tracks in the CTC. We use two parameters to identify the conversions. One is the VTPC hit occupancy defined in Section 4.1.2. Conversion electrons originating from outside of VTPC are identified by the condition that the VTPC hit occupancy is less than 0.2. For the conversion within the VTPC volume, CTC tracks with an opposite sign to the electron track are picked up within $\pm 90°$ cone of the electron track. We calculate the invariant mass at the intersection of the two tracks and find a track with the minimum mass. The conversion electron is identified by setting a maximum mass threshold of 500 MeV.

4.1.2 Plug electron parameters

Electron identification parameters in the plug region are described below.

Lateral shower profile

Energy density $\rho(r)$ about a shower centroid for electron in the plug calorimeter is known [50] to obey the exponential function:

$$\rho(r) = \frac{E}{2\pi\lambda} e^{-r/\lambda} \tag{4.9}$$

where r is a radius from the shower centroid and E is the electron energy. The width parameter λ characterizes the lateral shower size. We got $\lambda = 1.6$ cm for electrons from the test-beam data.

Most part of the electron shower is confined within three by three physical towers. In order to test a single electron hypothesis, we introduce the variable:

$$\chi^2_{\rm PEM} \equiv \left(\sum_i^{3\times3} \left(\frac{E_i^{meas} - E_i^{pred}}{\Delta E_i^{meas}} \right)^2 \right) /9 \tag{4.10}$$

where i runs over three by three calorimeter towers about the shower centroid, E_i^{meas} is the measured energy deposition in the ith tower and E_i^{pred} is the predicted energy of the ith tower calculated using Equation 4.9. The η, ϕ coordinates of the shower centroid is measured by calculating the weighted mean of tower energies over five by five adjacent towers about the shower centroid:

$$\phi_{\rm PEM} = \left\{ \sum_i^5 (\sum_j^5 E_{ij}^{tower}) \phi_i \right\} / \sum_{i,j}^{5\times5} E_{ij}^{tower} \tag{4.11}$$

$$\eta_{\rm PEM} = \left\{ \sum_j^5 (\sum_i^5 E_{ij}^{tower}) \eta_j \right\} / \sum_{i,j}^{5\times5} E_{ij}^{tower} \tag{4.12}$$

where i runs in azimuthal direction, j runs in pseudo-rapidity direction, and ϕ_i and η_i denote the azimuth and pseudo-rapidity coordinates of the tower center of the i-th tower. The calculation of $\rho(r)$ uses these values of $\phi_{\rm PEM}$ and $\eta_{\rm PEM}$ coordinates of the cluster centroid. The $\chi^2_{\rm PEM}$ varies by energy because it is divided by a constant variance: $\Delta E_i^{meas} = 0.1 E_i^{meas}$. Figure 4.7 shows the $\chi^2_{\rm PEM}$ distribution for the $W \rightarrow e\nu$ events where the distributions for 40 and 120 GeV/c electron data from the test beam are also presented. Higher energy gives a slightly smaller value of $\chi^2_{\rm PEM}$ because energy resolution becomes better at higher energy. Even though $\chi^2_{\rm PEM}$ has a small energy dependence, $\chi^2_{\rm PEM}$ holds high efficiency 94% for electrons from $W \rightarrow e\nu$ decays, whose energy range is typically 80–200 GeV.

Longitudinal shower profile

The ratio of the hadronic and electromagnetic calorimeter energy, $E_{\rm Had}/E_{\rm EM}$, is used also in the plug region. In the plug region, the total material thickness is 18.5–21.0X_0 depending on the incident polar angle of the electron. The thickness is relatively thicker than the cantral electromagnetic calorimeter. A fixed threshold value is used in the plug region:

$$E_{\rm Had}/E_{\rm EM} < 0.05. \tag{4.13}$$

A distribution of $E_{\rm Had}/E_{\rm EM}$ for electrons from $W \rightarrow e\nu$ decays is shown in Figure 4.8 togather with a distribution for backgrounds.

Track

In the plug region, CTC tracks are required to pass the following cuts:

1. $D < 10$ cm
2. $p_{\rm T} > 1$ GeV/c

3. $R < 25$ cm

4. $R_{exit} > 62.2$ cm

where D is the impact parameter, a closest distance of the track to the beam axis in r-ϕ plane, R is the distance between the shower centroid and the extrapolated position of the track on z=184.5 cm plane, R_{exit} is the distance between the point where the track exits the CTC volume at the end-plate and the beam axis. The last condition guarantees the electron pass at least first three super-layers of the CTC, as described in Section 3.2.2. The condition restricts the analysis region to $|\eta| < 1.6$ as long as we use the CTC track quality cuts. The track with the highest transverse momentum is chosen for a candidate of the electron track within a fixed cone radius of $R = 25$ cm from the cluster centroid.

The E/p parameter, as described in Section 4.1.1, is also used in the plug region. A distribution of E/p for electrons from $W \rightarrow e\nu$ decays is shown in Figure 4.9.

The coordinates of the extrapolated CTC track on z=184.5 cm plane is compared with the coordinates of the cluster centroid. Two matching variables are used:

$$\Delta\phi = \phi_{\rm PEM} - \phi_{track} \tag{4.14}$$

$$\Delta R = R_{\rm PEM} - R_{track} \tag{4.15}$$

where ϕ is the azimuthal angle, R is the distance from the beam axis on z=184.5 plane, $\phi_{\rm PEM}$ and $R_{\rm PEM}$ are the coordinates of the cluster centroid, and ϕ_{track} and R_{track} are the coordinates of the extrapolated position of the track on $z = 190.0$ cm plane. Distributions of $\Delta\phi$ and $\Delta\eta$ for electrons from $W \rightarrow e\nu$ decays are shown in Figure 4.10 and 4.11.

VTPC track information is also used for the plug electron identification. Electron leaves a track along the line connecting the event vertex and the cluster centroid.

Assuming a cylindrical road along the line, we measure the number of sense-wire hits found in the road. We define a parameter, VTPC-hit-occupancy R_{hits}^{VTPC}:

$$R_{hits}^{VTPC} = \frac{N_{hits}}{N_{exp}} \tag{4.16}$$

where N_{hits} is the number of sense-wire hits found in the road and N_{exp} is the expected number of hits. The N_{exp} is 24 in the sensitive region of the VTPC, but it becomes small near a radial board which separates the octants. We assume a road radius of 5 mm . A distribution of VTPC-hit-occupancy for electrons from $W \rightarrow e\nu$ decays is shown in Figure 4.12 togather with a distribution for backgrounds.

4.2 Electron selection

Inclusive electron samples are selected from the common data sets, described in Section 3.3, using the identification parameters described in Section 4.1.1.

4.2.1 Inclusive central electron sample

The inclusive central electron sample is selected from the inclusive electron common data set of the *Spin Cycle* data tapes (see Section 3.3), where the level 2 central electron trigger has been required.

Trigger requirements

The level-1 trigger (see Section 3.1.2) requires that a trigger cell in the central electromagnetic calorimeter contains at least 6 GeV of the transverse energy. The level-1 trigger also requires the crate sum E_{T} for the central electromagnetic calorimeter to be greater than 6 GeV.

At level 2 (see Section 3.1.3), a hardware processor finds seed trigger cells, whose

transverse energy is above 4 GeV. Four trigger cells adjacent to a seed cell are added to the cluster if their transverse energy is greater than 3.6 GeV. Each cluster cell becomes a seed to which neighboring cells are attached if their transverse energy is greater than the same E_T threshold. This process is continued until no more cells can be added. The total cluster E_T is computed by summing the electromagnetic and hadronic E_T over all the cells in a cluster. The central fast tracker finds tracks matched in azimuth with the cluster. The level-2 trigger requires the electromagnetic cluster E_T to be greater than 12 GeV, with a ratio to the total electromagnetic E_T (E_{Tot}/E_{EM}) less than 1.125, and also requires an associated CTC track with the transverse momentum greater than 6 GeV/c.

The level-3 trigger executes the same clustering algorithm used in off-line, as described in Section 3.2.5. Tracks are reconstructed with a resolution $\delta p_T/p_T = 0.0017 p_T$ (GeV/c). The level-3 trigger requires that the electromagnetic cluster E_T is greater than 12 GeV, with a ratio of the hadronic and electromagnetic energy (E_{Had}/E_{EM}) less than 0.125, and also an associated track with transverse momentum greater than 6 GeV. The electron cluster with 12 GeV $< E_T <$ 20 GeV must satisfy the additional cut $Lshr < 0.5$ where $Lshr$ is defined by Equation (4.2).

The trigger requirements for the central electrons are summarized in Table 4.1.

Off-line identification

The electron identification parameters described in Section 4.1.1 select final electron candidates. The threshold values for the identification parameters are given in Table 4.2. The distributions for the electron identificaiton parameters are shown in Figures 4.1 to 4.6. The electron sample used in those figures is $W \rightarrow e\nu$ candidates selected by the criteria given in Table 5.6. The arrows in the figures indicate where the cuts are made.

Trigger level	Variables	threshold
Level 0	BBC	
Level 1	Single trigger cell E_T	6.0 GeV
	Single crate sum E_T	6.0 GeV
Level 2	Seed trigger cell E_T	4.0 GeV
	Neighbor cell E_T	3.6 GeV
	Cluster E_T	12.0 GeV
	CFT track p_T	6.0 GeV/c
	E_{EM}/E_{Tot}	1.125
Level 3	Seed tower E_T	3.0 GeV
	Neighbor tower E_T	0.1 GeV
	Cluster E_T	12.0 GeV
	CTC track p_T	6.0 GeV/c
	E_{Had}/E_{EM}	0.125

Table 4.1: On-line trigger parameters for central electrons

Variable		Cut value
$Lshr$	$<$	0.2
χ^2_{strip}	$<$	15
E_{Had}/E_{EM}	$<$	$0.055 + 0.045 \times E/100$ GeV
E/p	$<$	1.5
$\lvert\Delta X\rvert$	$<$	1.5 cm
$\lvert\Delta Z\rvert$	$<$	3.0 cm

Table 4.2: Cut values for central electron identification parameters

Fiducial region

Fiducial cuts are applied on electron clusters to avoid insensitive regions in the detector and to ensure shower containment in the calorimeter large enough for reliable energy measurement. The central fiducial region is defined as follows:

1. The seed tower of the electron cluster must not be one of the ninth towers, the outermost towers, of the central calorimeter wedges. It must not be the seventh tower of the "chimney" module, which has two notched towers to allow access to the CDF superconducting solenoid.

2. The position of the strip chamber cluster must be at least 2.5 cm away from azimuthal boundary between the central calorimeter wedges.

3. The position of the strip chamber cluster must be at least 9 cm away from the $z = 0$ plane, the boundary of the east and west wedges.

4. In order to ensure measurements of the tracks in the CTC and VTPC, the z-coordinate of the event vertex (z_{vert}) must be within $|z_{vert}| < 60$ cm.

4.2.2 Inclusive plug electron sample

The inclusive plug electron sample is selected from the inclusive electron common data set from the *Full production* data tapes (see Section 3.3), where the entire raw data has been reprocessed.

Trigger requirements

The level-1 trigger requires the same criteria for plug electrons as for central electrons. It requires that a trigger cell in the plug electromagnetic calorimeter contains at least 4 GeV of the transverse energy, which is slightly lower than in the central calorimeter reflecting the finer physical tower size. The level 1 trigger also requires the crate sum E_{T} for the plug electromagnetic calorimeter to be greater than 6 GeV.

At level 2, a hardware processor applies the clustering algorithm with 4-GeV E_{T} threshold for a seed trigger cell and 3.6-GeV E_{T} threshold for neighbor trigger cells. The level-2 trigger requires the electromagnetic cluster E_{T} to be greater than 23 GeV, with a ratio of the total to electromagnetic cluster E_{T} less than 1.125. No track requirement is used for plug electrons.

The level-3 trigger requires that the electromagnetic cluster E_{T} is greater than 23 GeV, and that a ratio of the hadronic to electromagnetic E_{T} is less than 0.125.

The trigger requirements for plug electrons are summarized in Table 4.3.

Trigger level	Variables	threshold
Level 0	BBC	
Level 1	Single trigger cell E_T	4.0 GeV
	Single crate sum E_T	6.0 GeV
Level 2	Seed trigger cell E_T	4.0 GeV
	Neighbor cell E_T	3.6 GeV
	Cluster E_T	23.0 GeV
	E_{Tot}/E_{EM}	1.125
Level 3	Seed tower E_T	3.0 GeV
	Neighbor tower E_T	0.1 GeV
	Cluster E_T	23.0 GeV
	E_{Had}/E_{EM}	0.125

Table 4.3: On-line trigger parameters for plug electrons

Variable		Cut value
χ^2_{PEM}	$<$	15
$E_{\mathrm{Had}}/E_{\mathrm{EM}}$	$<$	0.05
E/p	$<$	2.5
$\lvert\Delta\phi\rvert$	$<$	0.04 radian
$\lvert\Delta R\rvert$	$<$	10.0 cm
VTPC-hit-occupancy	$>$	0.5

Table 4.4: Cut values for plug electron identification parameters

Offline identification

The final electron candidates are selected using the electron identification parameters described in Section 4.1.2. The cut values for the identification parameters are given in Table 4.4. The distributions for the electron identificaiton parameters are shown in Figures 4.7 to 4.12. The electron sample used in those figures is $W \rightarrow e\nu$ candidates selected by a missing E_T selection criterion given in Table 5.8. The arrows in Figures 4.7 to 4.12 indicate where the cuts are made.

Fiducial region

The plug fiducial region is defined as follows:

Variable		Cut value
Electron E_T	>	20 GeV (25 GeV)
Electron isolation (R=0.4)	<	0.1
$\not{E}_T$	>	20 GeV (25 GeV)
M_{tr}	>	50 GeV/c^2 (60 GeV/c^2)
No other jet with E_T greater than 10 GeV		

Table 4.5: Kinematical cuts for W selection

1. The position of the cluster centroid must not be in three outer tower annuli nor in two inner tower annuli. That is, it must be in a pseudo-rapidity range of $1.32 < \eta < 2.22$.

2. The position of the cluster centroid must be at least 5 degrees away from azimuthal boundaries between the quadrants.

3. In order to ensure measurements of the tracks in the CTC and the VTPC, the z-coordinate of the event vertex (z_{vert}) must be within $|z_{vert}| < 60$ cm.

4.3 W samples

W events are selected from the inclusive electron samples described in Section 4.2.1 and 4.2.2.

4.3.1 Kinematical parameters

In the decay $W \rightarrow e\nu$, both neutrino and electron acquire a momentum of about half the W mass. Neutrino leaves no energy deposition in the calorimeter. It creates large imbalance in the transverse plane view of energy deposition in the calorimetry. This imbalance is called the missing transverse energy (the missing E_T). If we take a vector sum of the transverse components of the calorimeter energy deposition, it gives

the direction and the magnitude of the missing E_{T}. The measurement of the missing E_{T} is described in Section 3.2.4.

The W mass is partially reconstructed using the transverse energy vector of the electron ($\vec{E_{\mathrm{T}}}$) and the missing E_{T} vector ($\vec{\not{E}_{\mathrm{T}}}$). The transverse mass is defined as follows:

$$M_{tr} \equiv \sqrt{2\{|\vec{\not{E}_{\mathrm{T}}}||\vec{E_{\mathrm{T}}}| - (\vec{\not{E}_{\mathrm{T}}} \cdot \vec{E_{\mathrm{T}}})\}} \tag{4.17}$$

where the second component in square-root represents inner product of two vectors.

W events are identified by imposing condition of the existence of a high E_{T} electron and large missing E_{T}. Higher transverse mass threshold removes more background contamination, because background events, which are generally with small missing E_{T}, give a smaller transverse mass than W events.

We select events containing an electrons, which passed the trigger requirements, the electron identification, and the fiducial cuts described in Section 4.2. The electron E_{T} is required to be greater than 20 GeV for central electrons and 25 GeV for plug electrons. The transverse mass between the electron $\vec{E_{\mathrm{T}}}$ and the $\vec{\not{E}_{\mathrm{T}}}$ is required to be greater than 50 GeV/c^2 for central Ws and 60 GeV/c^2 for plug Ws. Kinematical cuts for the W event selection are summarized in Table 4.5. Note that we require the W event contains no jet. This reduces the level of background as well as a kinematical uncertainty due to W + jet event contamination.

4.3.2 Statistics

In the central region, we have 2944 W candidates on which one electron and large missing E_{T} are required. The central electron trigger and fiducial region requirements cut 20% events. We now have 2342 W candidates. A no-jet requirement cuts another 20% events. Finally we have had 1752 events of W candidates.

In the plug region, we have 1843 W candidates on which one electron and large miss-

ing E_T are required. The plug electron trigger and fiducial region requirements cut 25% events. We now have 1388 candidates. High transverse mass threshold (60 GeV/c^2) rejects another 25% events. We now have 942 candidates. A no-jet requirement cuts another 20% events. The sample is now 731 candidates. Finally the CTC track requirement to restrict a measurement in the lower pseudo-rapidity region ($|\eta| < 1.6$) reduces the sample to 262 candidates.

Note that the higher transverse mass thresold in the plug region cuts more events than in the central. This is required to get rid of an uncertainty due to reduced trigger efficiency for the events in a low transverse mass region. The CTC track requirement also cuts many events in the plug region. Because the CTC coverage where a good momentum measurement is allowed is much smaller than the coverage of the plug calorimeter.

The distributions of the transverse energy, the missing E_T and the transverse mass are shown in Figures 4.13–4.16 for the cantral and plug W samples with no jet.

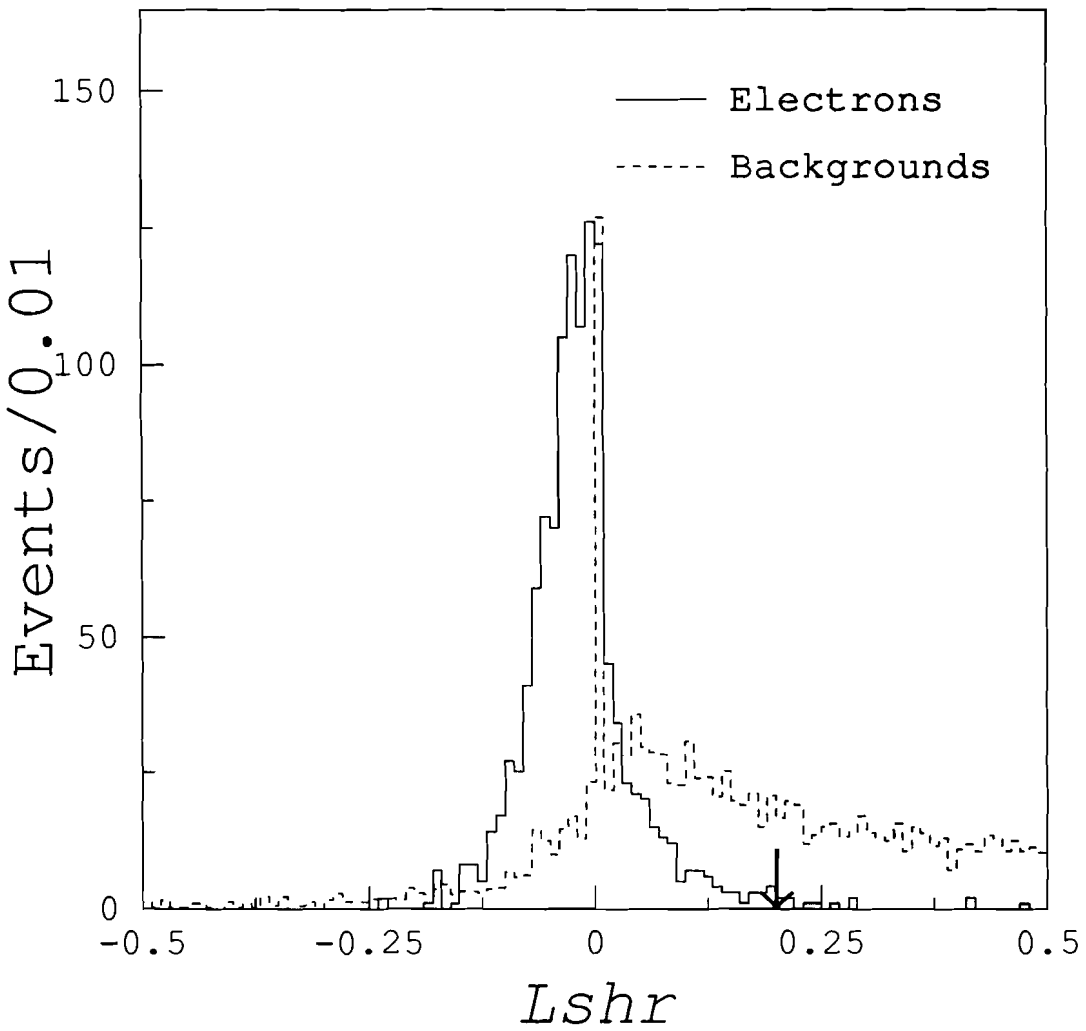

Figure 4.1: A distribution of *Lshr* for electrons from $W \rightarrow e\nu$ decays (solid line), passing the identification cuts listed in Table 5.6. The distribution for the electromagnetic clusters in the inclusive jet sample (dashed line) is overlaid.

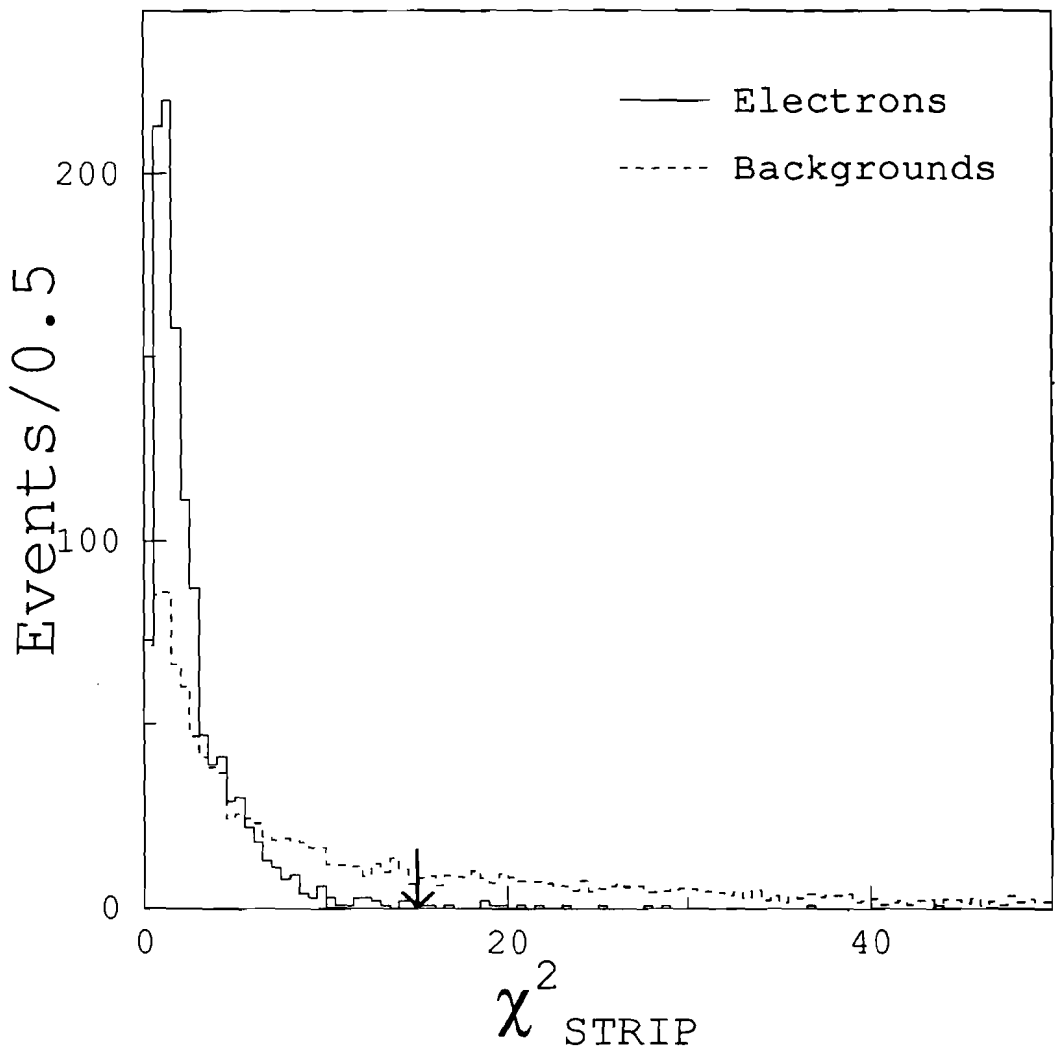

Figure 4.2: A distribution of χ^2_{strip} for electrons from $W \rightarrow e\nu$ decays (solid line), passing the identification cuts listed in Table 5.6. The distribution for the electromagnetic clusters in the inclusive jet sample (dashed line) is overlaid.

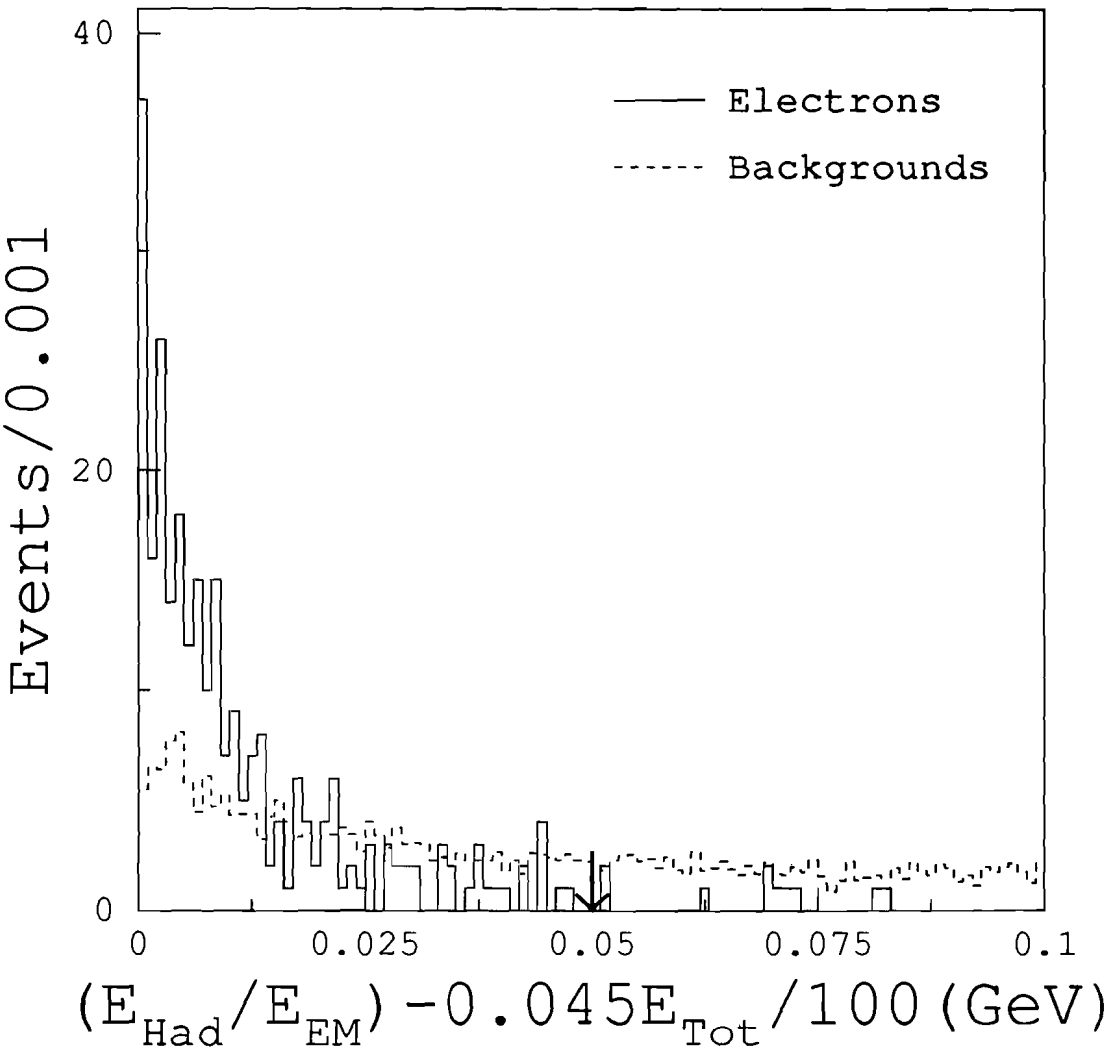

Figure 4.3: A distribution of $E_{\rm Had}/E_{\rm EM}$ for central electrons from $W \rightarrow e\nu$ decays (solid line), passing the identification cuts listed in Table 5.6. The distribution for the electromagnetic clusters in the inclusive jet sample (dashed line) is overlaid.

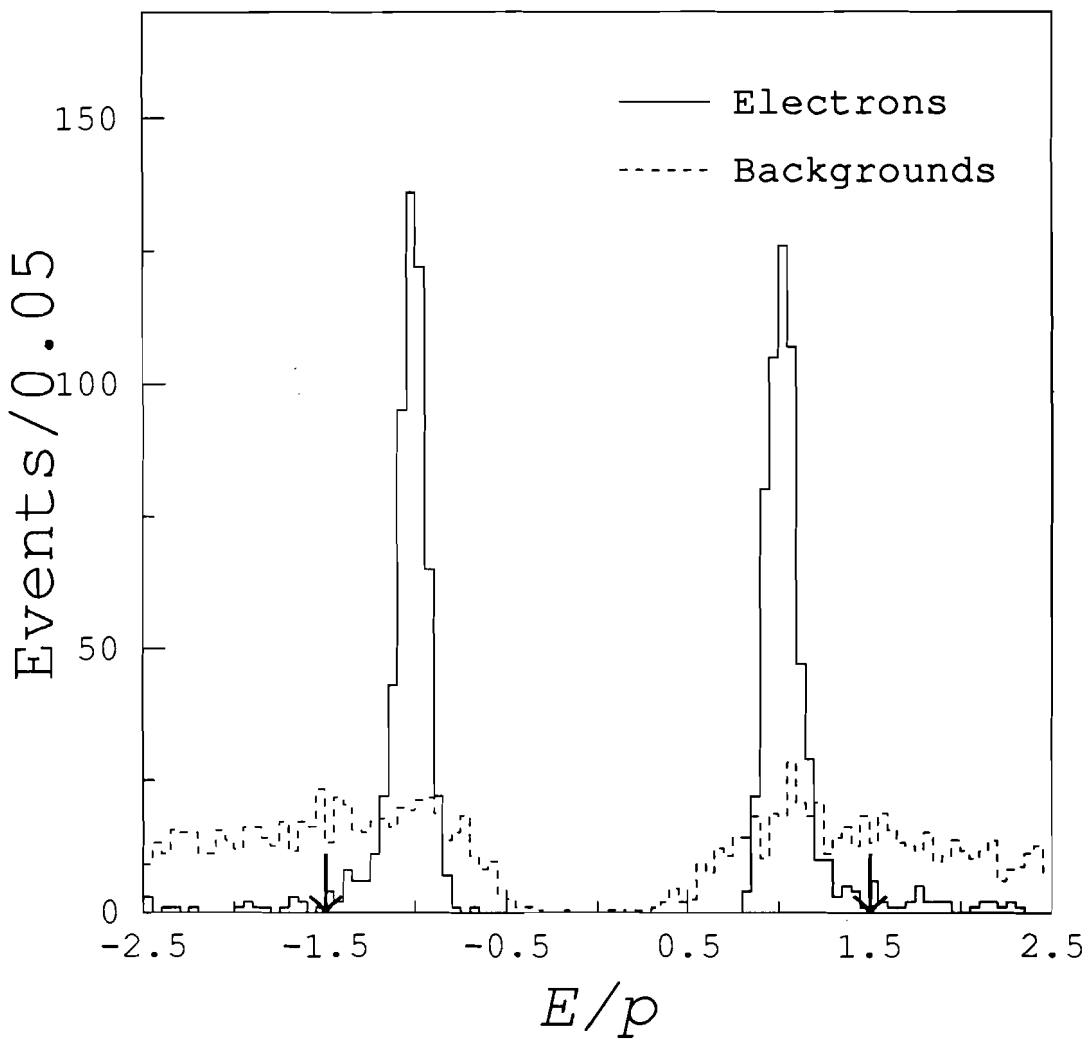

Figure 4.4: A distribution of E/p for central electrons from $W \rightarrow e\nu$ decays (solid line), passing the identification cuts listed in Table 5.6. The distribution for the electromagnetic clusters in the inclusive jet sample (dashed line) is overlaid.

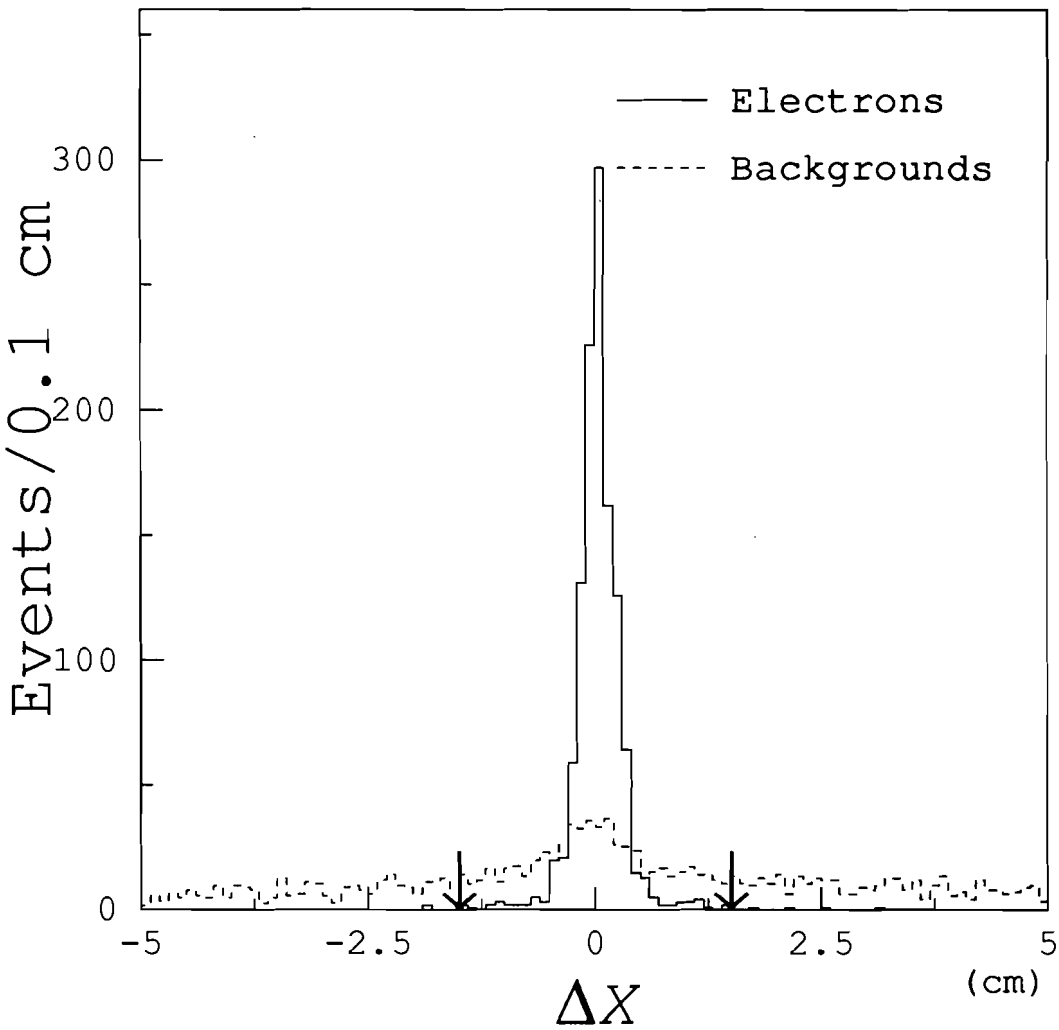

Figure 4.5: A distribution of ΔX for central electrons from $W \rightarrow e\nu$ decays (solid line), passing the identification cuts listed in Table 5.6. The distribution for the electromagnetic clusters in the inclusive jet sample (dashed line) is overlaid.

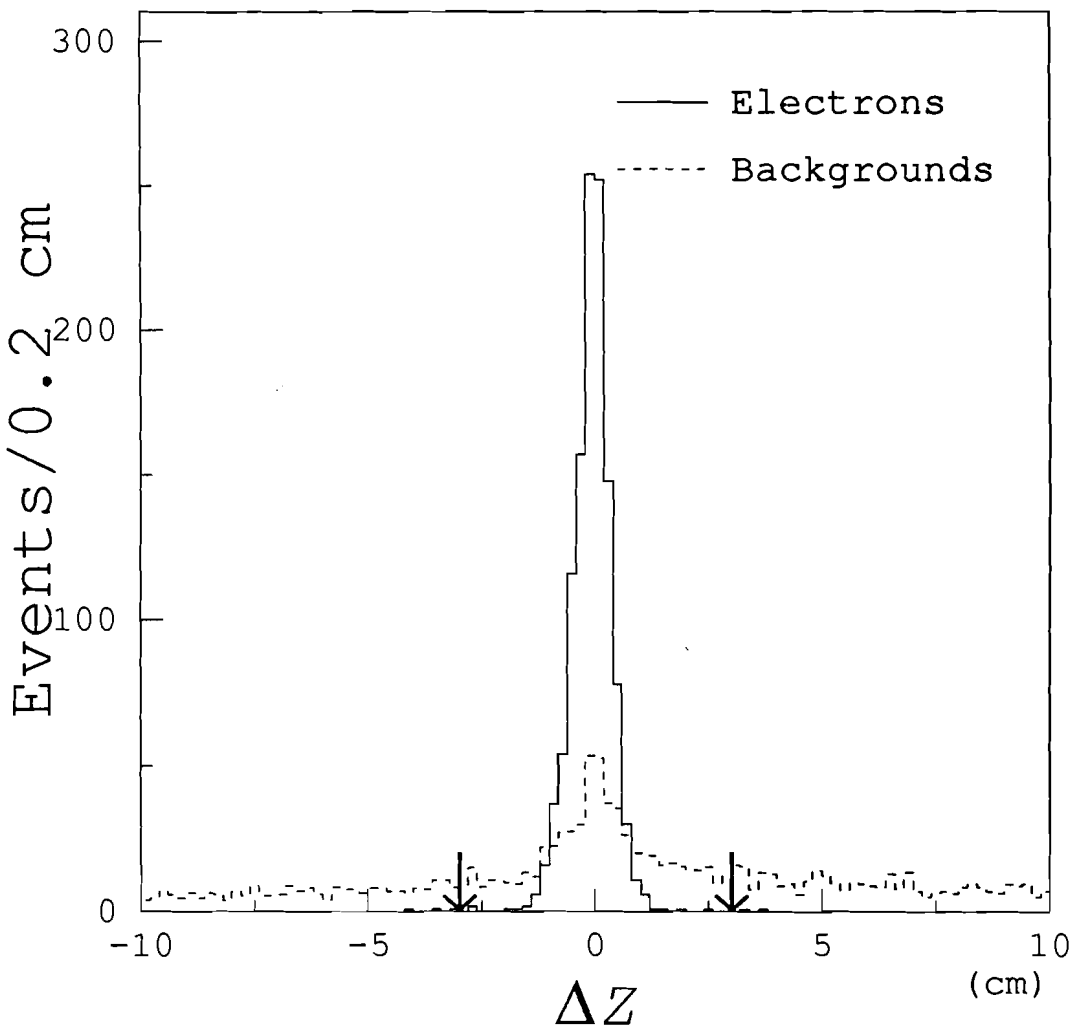

Figure 4.6: A distribution of ΔZ for central electrons from $W \rightarrow e\nu$ decays (solid line), passing the identification cuts listed in Table 5.6. The distribution for the electromagnetic clusters in the inclusive jet sample (dashed line) is overlaid.

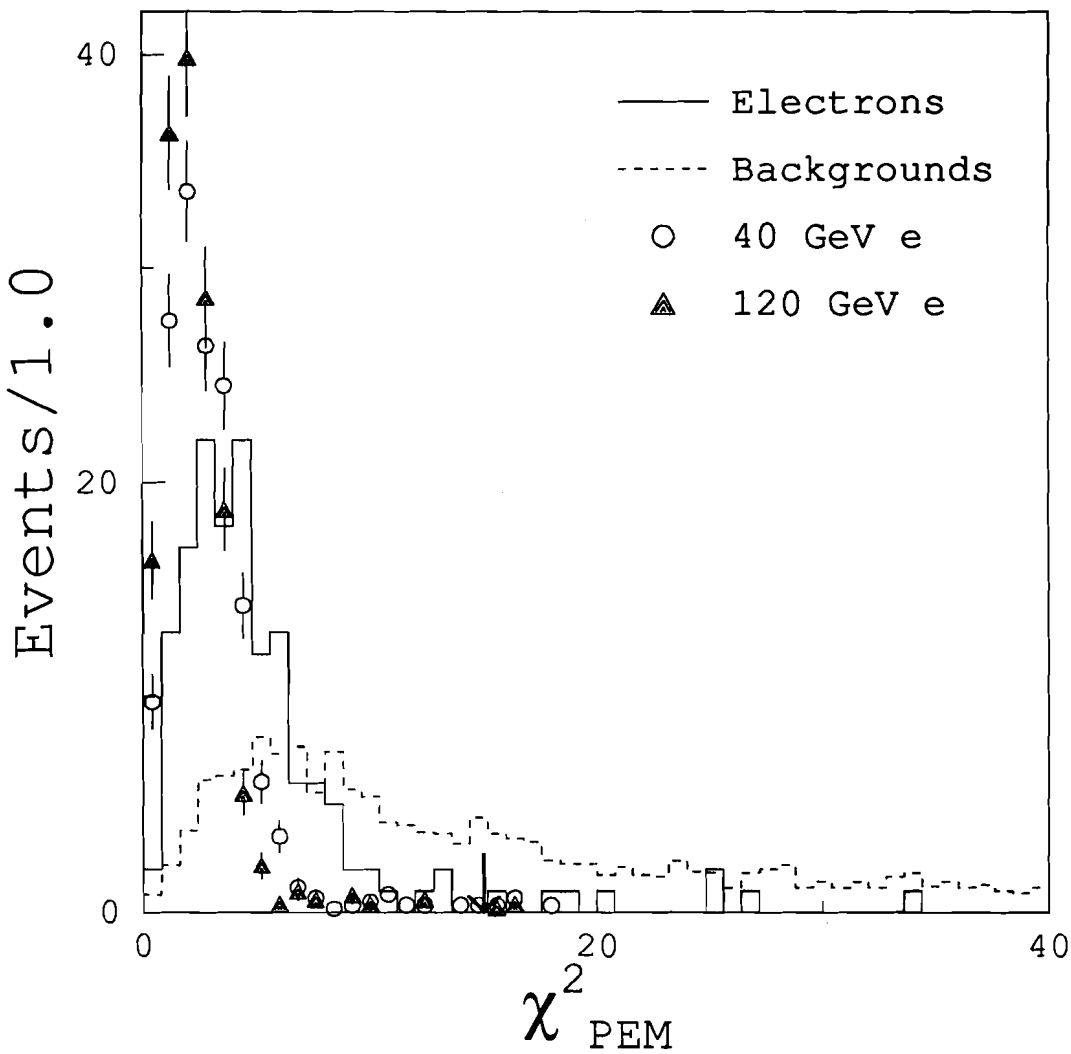

Figure 4.7: A distribution of $\chi^2_{\rm PEM}$ for electrons from $W \rightarrow e\nu$ decays (solid line), passing the identification cuts listed in Table 5.8. The distribution for the electromagnetic clusters in the inclusive jet sample (dashed line) is overlaid. The distributions for 40 and 120 GeV/c electrons from 1985 test beam data are also presented.

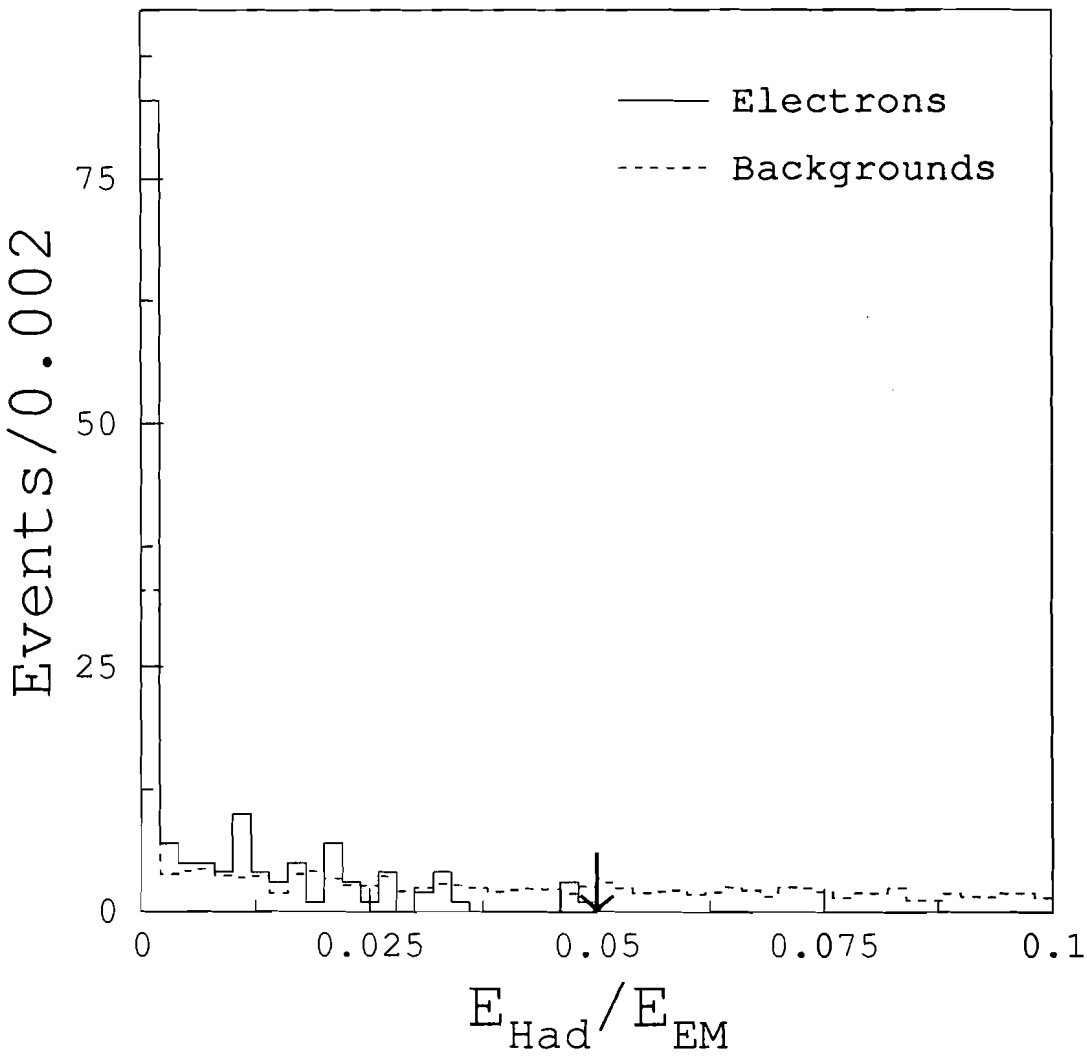

Figure 4.8: A distribution of $E_{\rm Had}/E_{\rm EM}$ for plug electrons from $W \rightarrow e\nu$ decays (solid line), passing the identification cuts listed in Table 5.8. The distribution for the electromagnetic clusters in the inclusive jet sample (dashed line) is overlaid.

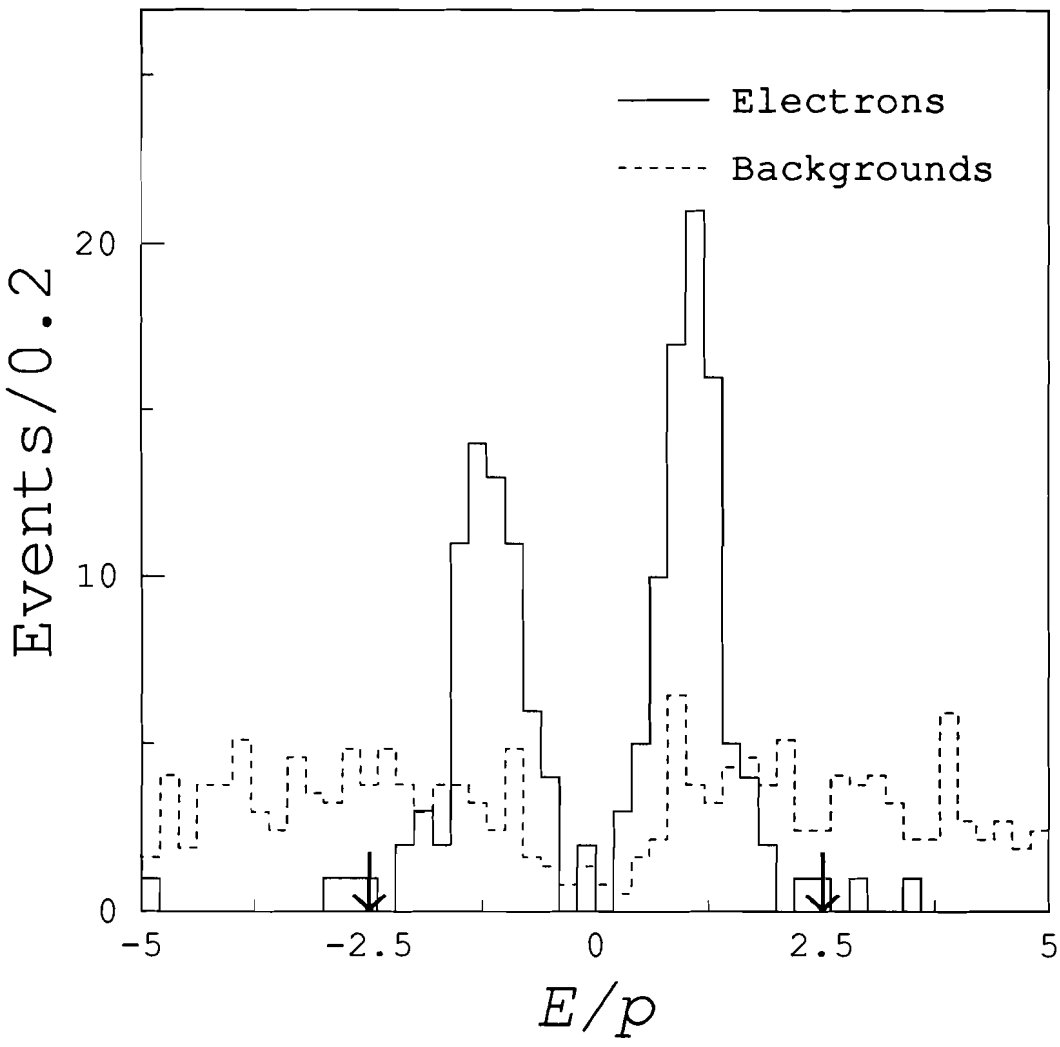

Figure 4.9: A distribution of E/p for plug electrons from $W \rightarrow e\nu$ decays (solid line), passing the identification cuts listed in Table 5.8. The distribution for the electromagnetic clusters in the inclusive jet sample (dashed line) is overlaid.

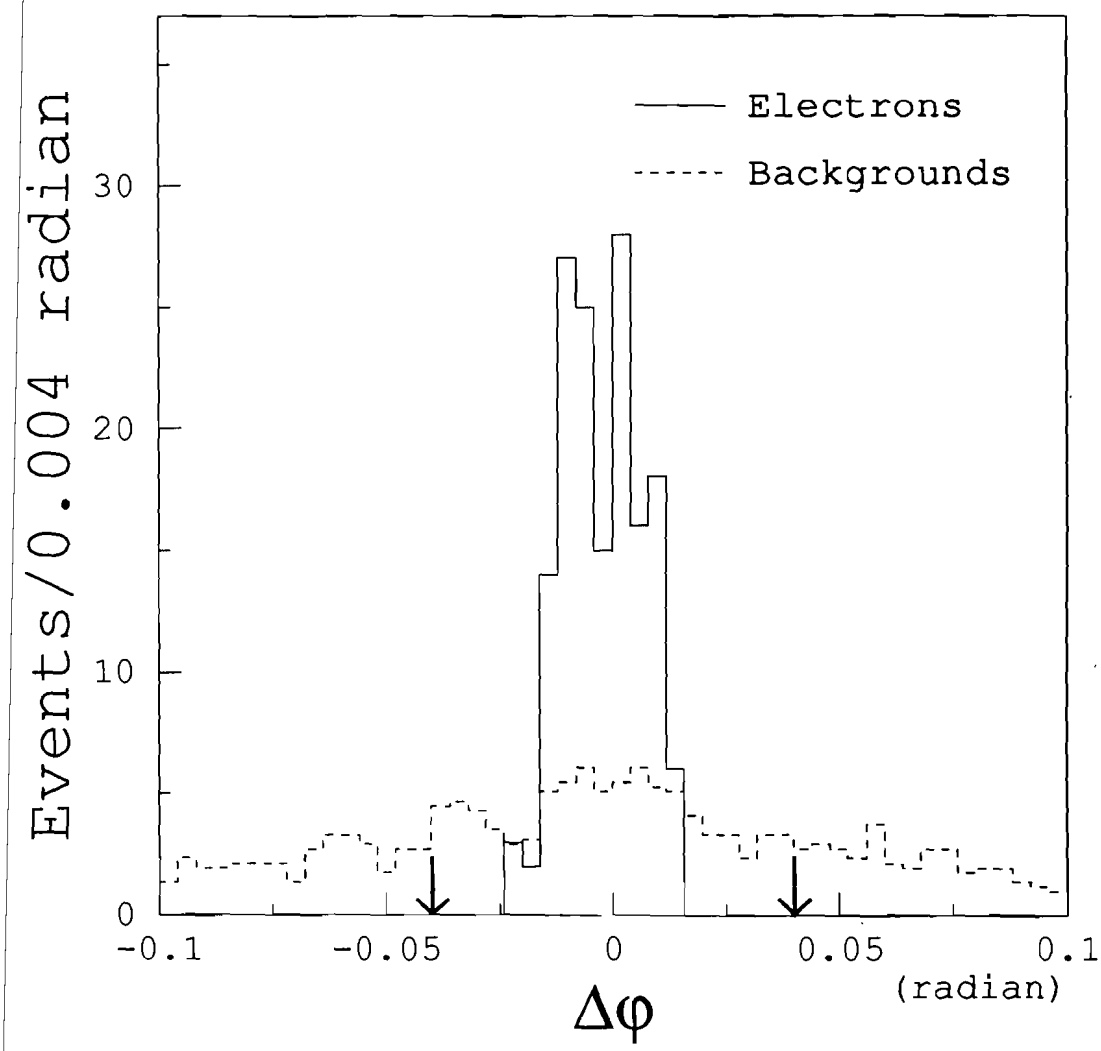

Figure 4.10: A distribution of $\Delta\phi$ for plug electrons from $W \rightarrow e\nu$ decays (solid line), passing the identification cuts listed in Table 5.8. The distribution for the electromagnetic clusters in the inclusive jet sample (dashed line) is overlaid.

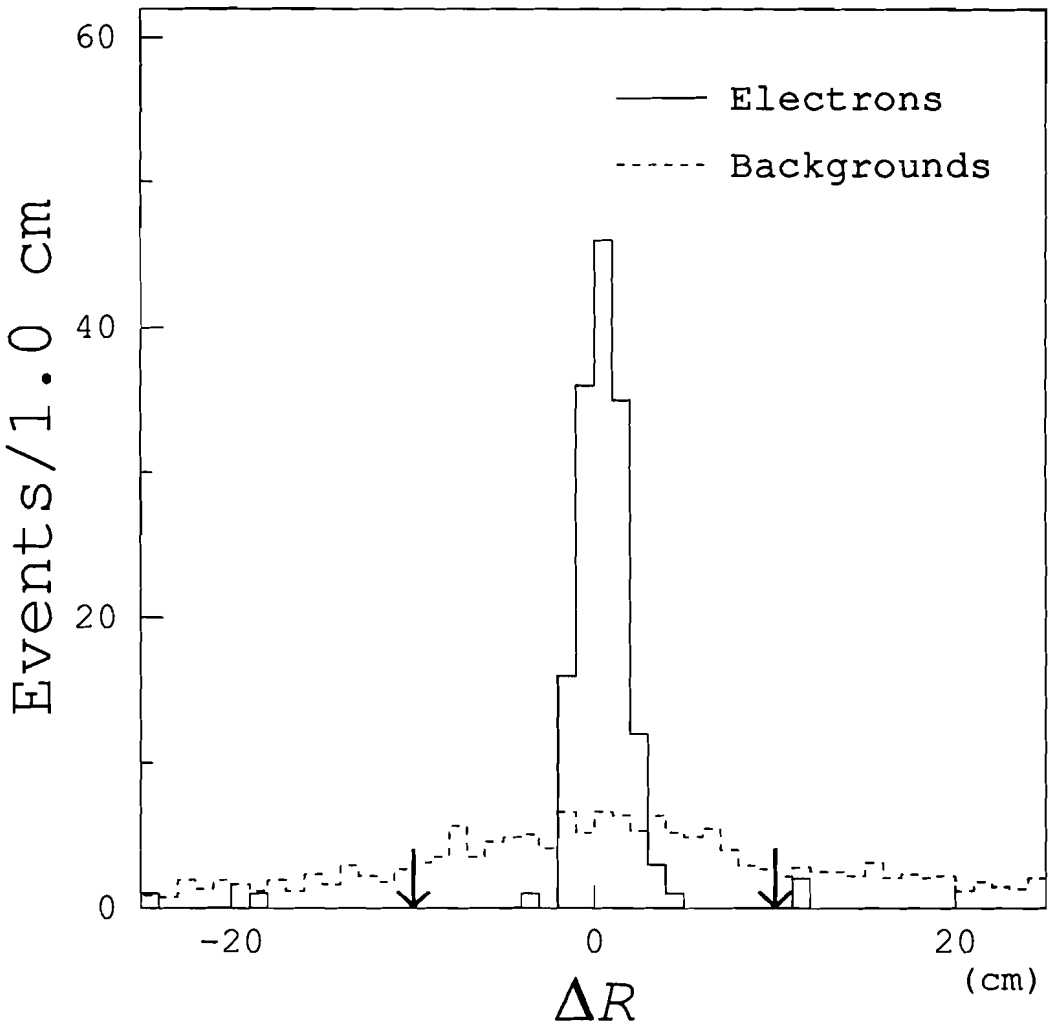

Figure 4.11: A distribution of ΔR for plug electrons from $W \rightarrow e\nu$ decays (solid line), passing the identification cuts listed in Table 5.8. The distribution for the electromagnetic clusters in the inclusive jet sample (dashed line) is overlaid.

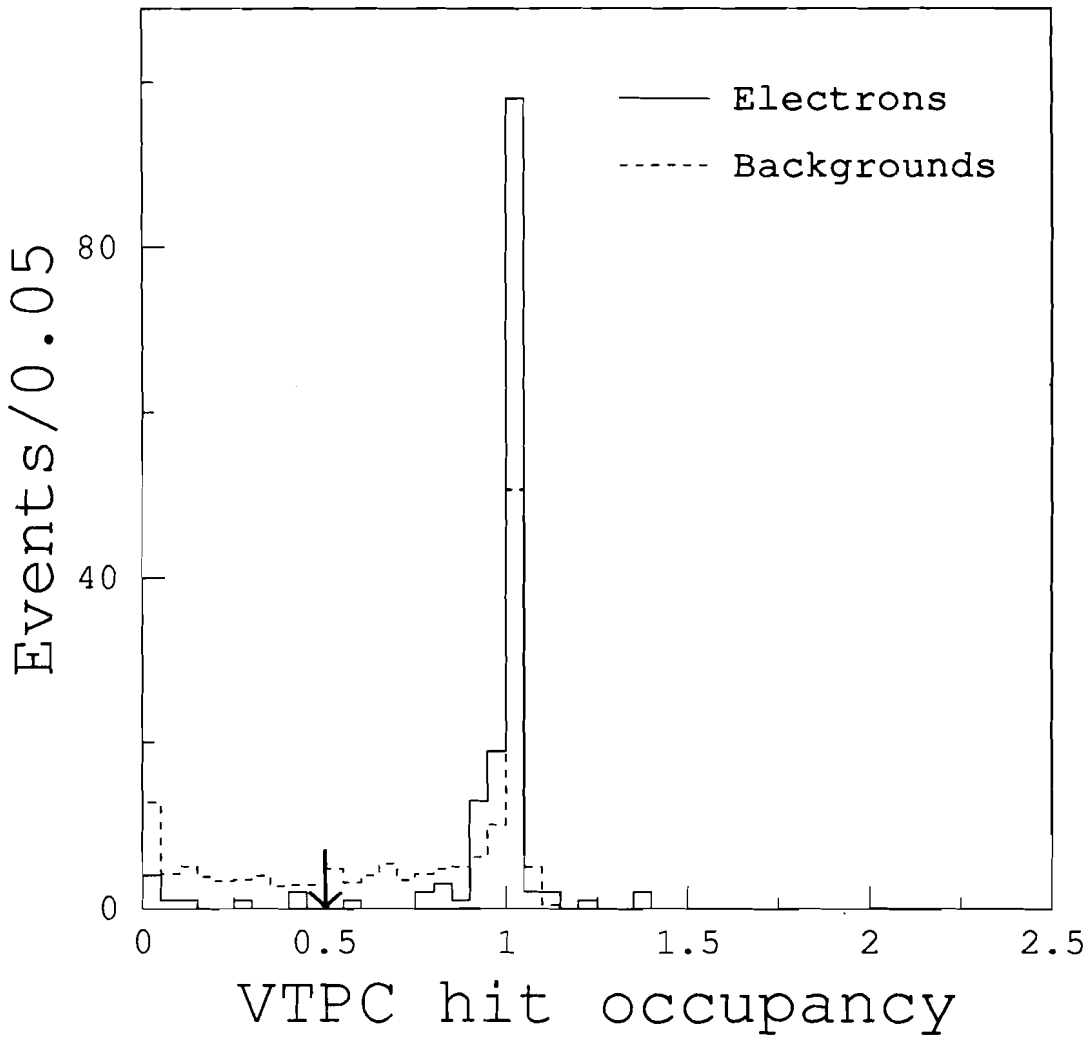

Figure 4.12: A distribution of VTPC-hit-occupancy for plug electrons from $W \rightarrow e\nu$ decays (solid line), passing the identification cuts listed in Table 5.8. The distribution for the electromagnetic clusters in the inclusive jet sample (dashed line) is overlaid.

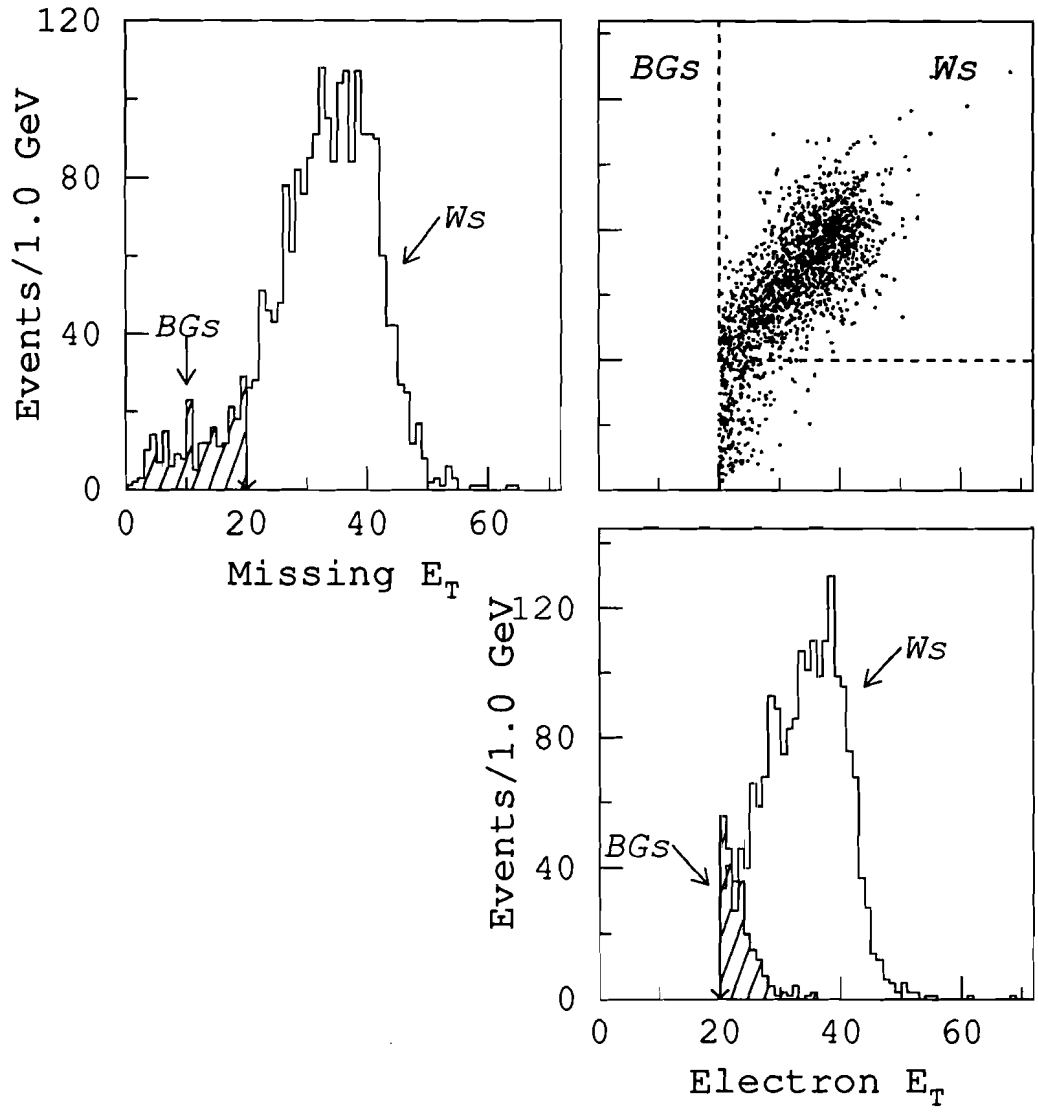

Figure 4.13: Electron E_T and $\not{E}_T$ distributions for the inclusive central electron sample. No jet in the event is required. The W and background (shadowed histogram) candidates are separately projected.

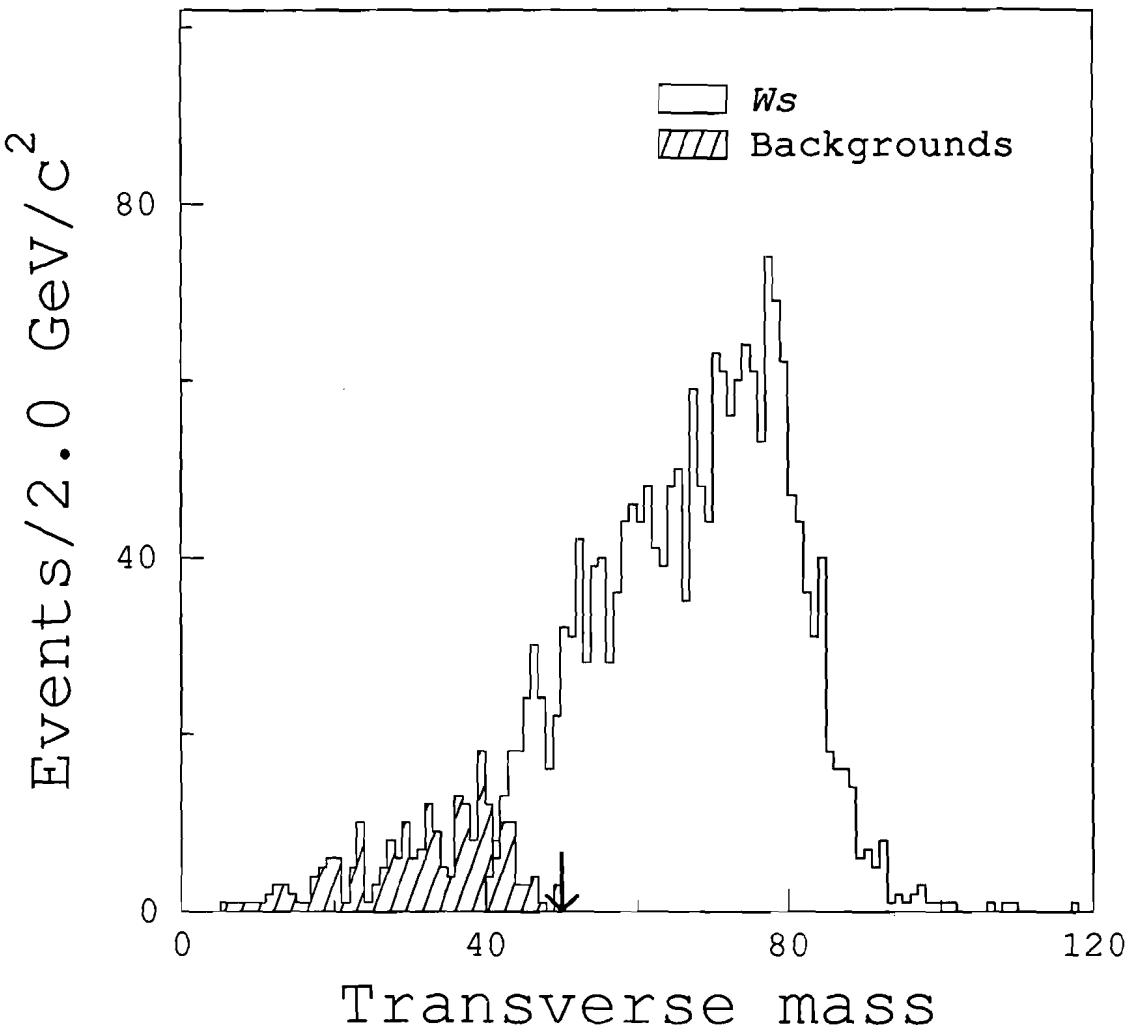

Figure 4.14: A transverse mass distribution for the central Ws. No jet in the events is required. The distribution for background candidates is also presented (shadowed histogram).

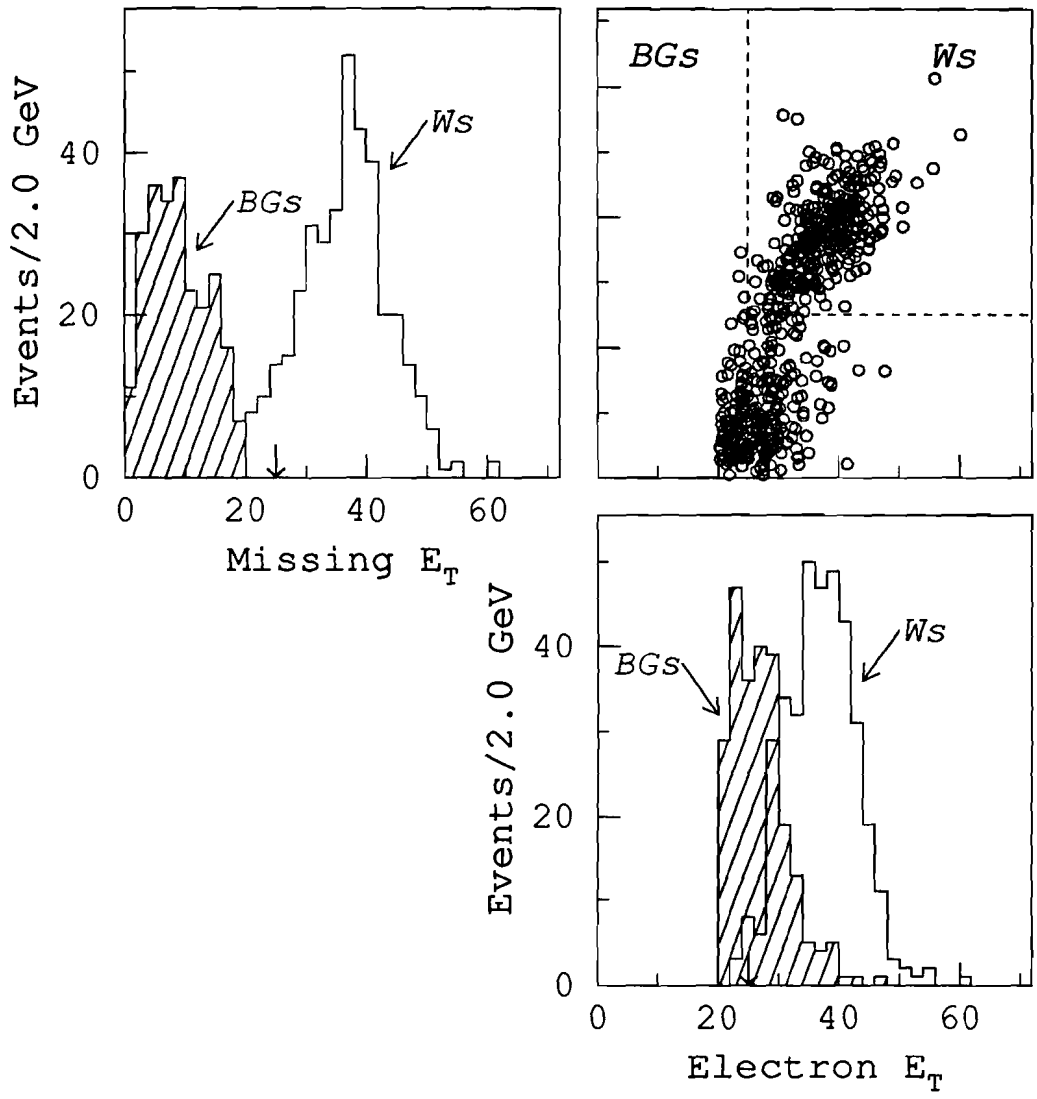

Figure 4.15: Electron E_T and $\not{E}_T$ distributions for the inclusive plug electron sample. No jet in the event is required. The W and background (shadowed histogram) candidates are separately projected.

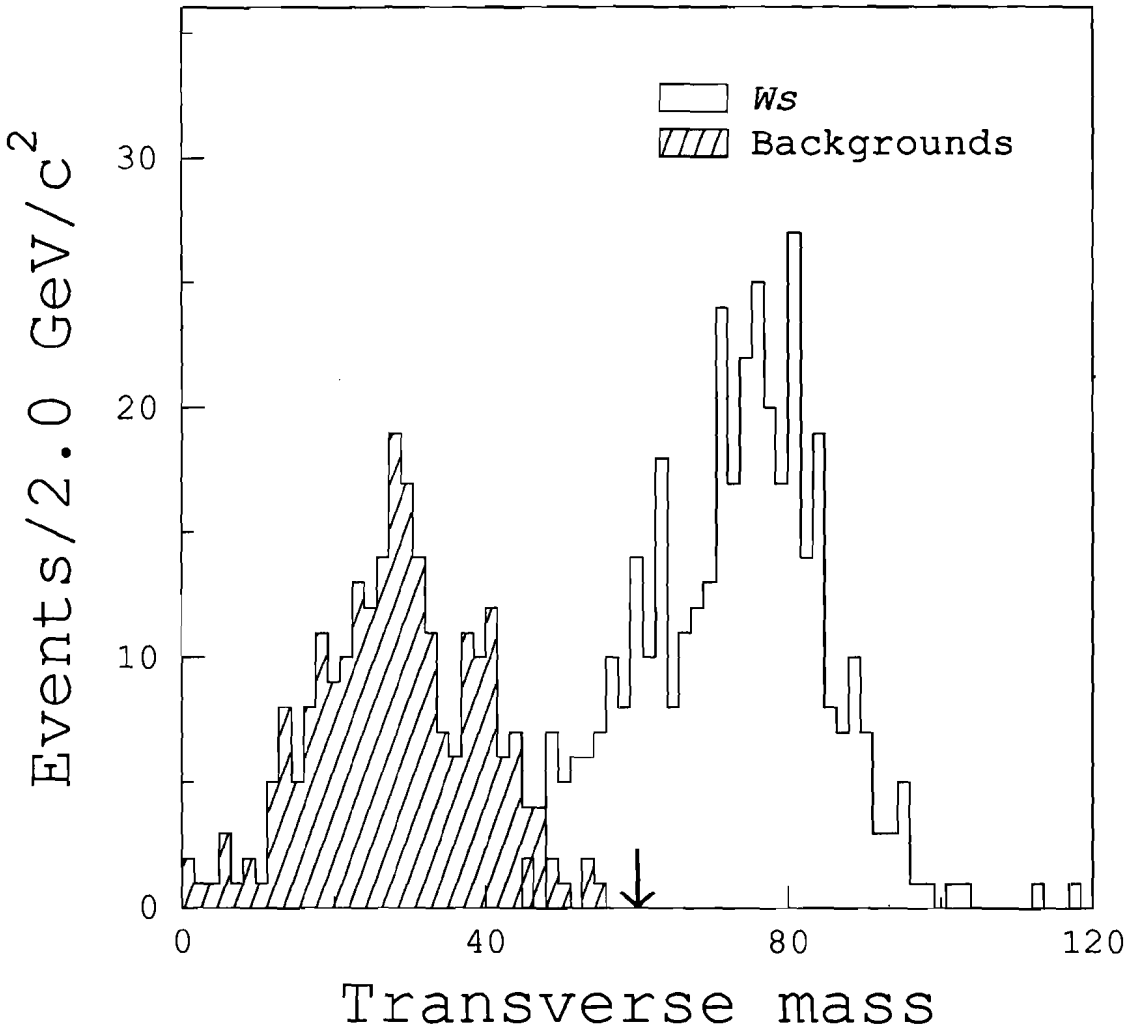

Figure 4.16: The transverse mass distribution for the plug Ws. No jet in the event is required. The distribution for background candidates is also presented (shadowed histogram).

Chapter 5

Energy scale and efficiency for electrons

Lepton charge asymmetry measurement in the $W \rightarrow e\nu$ decay is influenced by a transverse mass threshold, electron and positron selection efficiency and background which will be described in Chapter 7. Transverse mass measurement depends on the measurements of electron energy and missing transverse energy.

5.1 Energy scale

Precise momentum measurement by the central tracking chamber helps not only the electron identification but also the energy scale determination. Energy calibration of the central electromagnetic calorimeter is described elsewhere [2], and briefly summarized below. Energy calibration of the plug electromagnetic calorimeter is described in Section 5.1.3.

5.1.1 Momentum scale

Momentum scale of the track measured by the central tracking chamber is ensured using a resonance of two-muon events, J/ψs. The sample is selected from the inclusive muon sample of the *Spin Cycle* data (see Section 3.3). Momentum scale of the CTC track is verified by the invariant mass peak of J/ψs, which is shown in Figure 5.1. The mean value (3.0963 ± 0.0005) GeV/c^2 [2] from a fit to the data is consistent with the world average of (3.0969 ± 0.0001) GeV/c^2 [29]. We conclude that the tracking chamber is absolutely calibrated to 0.1%.

5.1.2 Energy scale of the central electromagnetic calorimeter

Three successive corrections are applied to the energy measurement of the central electrons. The verified momentum scale of the central tracking chamber is used to determine the energy scale of the central electromagnetic calorimeter.

Difference of the energy response within one tower, which depends on the electron hit position, is corrected using the test-beam data [30]. This correction accounts for light attenuation, the effect of cracks, and lateral shower leakage. The electron hit position is determined by the strip chambers. The accuracy is $\pm 1\%$ over the fiducial region defined in Section 4.2.1.

Tower-to-tower energy response is calibrated using 17000 electrons from the central inclusive electron sample. The sample was selected from the *Spin Cycle* data tapes (see Section 3.3), which was mostly triggered by the trigger conditions shown in Table 4.1. Each tower has about 35 electron candidates. Mean values of E/p for each tower are constrained to 1.0. This constraint allows us to make mutual calibration among 478 CEM towers. The resulting relative tower gains have an average statistical accuracy of 1.7%.

Absolute energy scale of the central electromagnetic calorimeter is determined by

comparing the E/p distribution for W electrons to the prediction that includes radiative effects. Two sources of the photon emission are taken into account. Electron radiates when they pass through material, lowering the observed momentum. The W decay may also have associated internal radiation. While the calorimeter measures most of the radiated photon energy, the tracking chamber measures only the momentum of the charged track. Thus we expect $E/p > 1$ on average. The simulation predicts this mean should be shifted by 1.74%. Uncertainties of this value is as follows. The CTC is calibrated to 0.1%. The shift of the peak is assigned a systematic error of 0.1%, reflecting the uncertainty of material inside the CTC. Additional systematic uncertainty due to sensitivity to a choice of fitting window, resolution, and data selection is 0.11%. Statistical uncertainty for 1700 W electron candidates is 0.16%. Overall uncertainty is 0.24%. We correct the energy of the central electron by a factor of 1.0174 with systematic uncertainty of 0.24%.

5.1.3 Energy scale of the plug electromagnetic calorimeter

Four kinds of corrections are applied to the energy measurement of the plug electrons.

1. Tower map correction
2. Non-linearity correction
3. Dead layer correction
4. Quadrant gain correction

In order to make tower-to-tower energy calibration, 2304 towers of the plug calorimeter were exposed to 100 GeV electrons in 1985 test beam [20]. A gain correction

factor a_i of the ith tower was calculated by minimizing χ^2 defined as follows:

$$\chi^2 = \sum_k \left(\sum_i a_i A_{ik} + \sum_j A_{jk} - M \right)^2 \tag{5.1}$$

where i runs over towers in a quadrant, A_{ik} is the signal of the ith tower for the kth event, and M is the ideal gain constant. In the equation, the ideal gain constant M compares to the energy sum in a quadrant, $\sum_j A_{jk}$. In an ideal detector, a_i is all zero because M is always equal to $\sum_j A_{jk}$. The electron energy is corrected by these tower-map factors a_i. Magnitude of the correction is roughly $\pm 5\%$ with an error of $\pm 1.3\%$.

The response against electrons with various incident energies was also measured in 1985 test beam. Longitudinal leakage of the electromagnetic shower and gain saturation of the gas proportional tubes result in non-linear response of the calorimeter. Data points were fitted as a function of energy by a quadratic form. The quadratic term becomes about 16% at 200 GeV, 4% of which is accounted for by the longitudinal leakage. The correction function is given by

$$E_{corr} = \frac{E_{in}}{1.01 + 0.013\eta_{cl}} + \frac{0.75 + 1.3\eta_{cl}}{1.01 + 0.013\eta_{cl}} \frac{E_{in}^2}{10^4}, \tag{5.2}$$

where E_{corr} is the corrected electron energy and E_{in} is the uncorrected electron energy, and η_{cl} is the pseudo-rapidity coordinate of the cluster centroid. The function gives $E_{corr} = 100$ GeV for the input E_{in} of 100 GeV. A size of the non-linearity correction is less than 1% for the electrons from W decays.

We exposed all the plug calorimeter modules in the test beam. During the transportation from the assembly hall to the test beam, some anode wires were accidentally cut which caused 10 dead planes. Dead planes found during the 1988-1989 run are listed in Table A.1. Firstly the calorimeter tower energies are corrected by the factors

given in Table A.1 to calibrate missing E_T measurement and jet energy measurement. These correction factors are based on 50-GeV pions in the test beam. Electron energy is corrected as follows. Electron energy loss in a dead plane is calculated using a formula of the longitudinal shower development,

$$\Delta E/\Delta t = At^{\alpha}e^{-\beta t} \tag{5.3}$$

with parameters A, α, and β of the following energy dependence:

$$\begin{aligned} A &= E\beta^{\alpha+1}/\Gamma(\alpha+1), \\ \alpha &= 1.91 + 0.484 \ln E, \\ \beta &= 0.582 - 0.014 \ln E, \end{aligned}$$

where E is electron energy and t is depth of the calorimeter in radiation length. A correction of the i-th dead layer is made by multiplying the factor C_{DL} defined by

$$C_{DL}(E) \equiv 1/(1-\epsilon), \tag{5.4}$$

here

$$\epsilon = \int_{t_i}^{t_{i+1}} (\Delta E/\Delta t)dt / \left(\int_{t_1}^{t_{34}} \Delta E/\Delta t dt\right) \tag{5.5}$$

where the integration in the denominator extends over entire 34 layers. The maximum size of the correction is about 5%, when a layer near shower maximum is dead. Even if we used uncorrected energy for the calculation, the error wound be less than 1%.

An ideal gain M in Equation 5.1 was measured on quadrant by quadrant basis. A gain of the plug calorimeter varies with temperature and pressure of gas in the chamber. The gas-gain monitoring system in 1985 test beam had not successfully measured the absolute energy scale. But the relative gas-gain was monitored and traced during the

mapping of one quadrant. The tower-map correction by Equation 5.1 has been made by ignoring a relative gain difference among eight quadrants, that is, by assuming eight gain constants $M_\ell\,(\ell = 1,8)$ for eight quadrants are equal. The quadrant gain constants are determined using the transverse energy spectra of W electrons and the invariant mass spectra of the Z candidates. The W and Z samples used here are selected from the inclusive electron sample of the *Spin Cycle* data (see Section 3.3). The W sample is splitted into eight samples according to a quadrant number where the electron cluster exists. The transverse mass spectra are fitted by the distribution obtained from a Monte Carlo for each quadrant and compared between the quadrants. The Z sample is a subset of the Z candidates that has one electron in the central region and another in the plug region. It is splited into eight samples by a quadrant number where the plug electron cluster exists. The mean values of their invariant mass spectra are compared between the quadrants. The quadrant gain constants determined using W and Z samples are given in Tabel A.1. These are the relative gains to the reference quadrant, the Top-North-East quadrant, which was exposed in the test beam to determine the absolute energy scale.

The electron cluster energy in the plug is corrected as follows. The coarse dead-layer correction based on 50 GeV pion shower and the quadrant gain correction are made in the calorimeter tower reconstruction (see Section 3.2.3) during the event reconstruction process. The electromagnetic clusters (see Section 3.2.5) are reconstructed among the calorimetry towers. Then the tower map correction, the non-linearity correction and the dead-layer correction based on Equation 5.3 are applied on each plug electron cluster. An invariant mass distribution of the central-plug Z sample is shown in Figure 5.2, where the distribution of the central-central Z sample is overlaid. A transverse mass distribution of the plug W sample is shown in Figure 5.3, where the distribution of a Monte Carlo simulation is overlaid. A distribution of the energy to momentum ratio (E/p) for the plug electrons was already shown in Figure 4.4.

5.2 Electron identification efficiency

Electron identification efficiencies are measured for electrons and positrons. Equal efficiencies for electrons and positrons will ensure the asymmetry measurement without artificial biases. In order to estimate a charge-dependent efficiency, we first estimate the offline reconstruction efficiency of the CTC track in Section 5.2.1. Trigger efficiencies are measured for the electrons reconstructed in the off-line. Efficiencies for the identification parameters we used are estimated in Section 5.2.3 for the electron objects where the CTC track successfully reconstructed.

5.2.1 Off-line track finding efficiency

In order to estimate the track finding efficiency of the central tracking chamber in the offline event reconstruction, W candidates extracted from the missing E_{T} sample from the *Spin Cycle* data are used. Since the missing E_{T} trigger relies only on the transverse energy measurement in the calorimeter, it is independent of a track measurement. One is interested in the electrons where the CTC track is not successfully reconstructed by the offline reconstruction process. We select W candidates with an electron-like object which have failed a cut of the energy-momentum ratio (E/p).

These candidates are visually scanned on an event display. The transverse plane picture is displayed, which contains the CTC wire hits, the reconstructed tracks and the electromagnetic cluster position. In order to estimate a track finding efficiency, an unreconstructed trajectory of the CTC hits which points an electromagnetic cluster are searched.

Track finding efficiency for central electrons

Event selection criteria are shown in Table 5.1. Note again that we require E/p to be greater than 1.5 in order to find unreconstructed tracks.

Variable		Cut value
Trigger requirements		
$\not{E}_T$	$>$	25 GeV
Electron cuts:		
Lshr	$<$	0.2
E_{EM}/E_{Had}	$<$	$0.055 + 0.045E/100(\text{GeV})$
VTPC-hit-occupancy	$>$	0.5
E/p	$>$	1.5
Kinematical cuts:		
Electron E_T	$>$	20 GeV (25 GeV)
$\not{E}_T$	$>$	20 GeV (25 GeV)
No other jet with E_T greater than 5 GeV		

Table 5.1: Selection parameters for the central Ws for the track finding efficiency analysis. The trigger is based on the missing E_T trigger.

Out of 2978 W candidates with missing E_T and a central electron, we found 245 candidates which passed the selection cuts. They were visually scanned on an event display. No unreconstructed high p_T tracks points to an electromagnetic cluster was found. We conclude that the track finding efficiency for the central electrons is more than 99.9%.

Most of the 245 candidates seems to come from cosmic-ray muons, which coincide with the event trigger and lose their energy in the calorimeter. Many of them are associated with a CTC trajectory, one end of which points to a cluster but the other end does not point to the beam axis. We found 41 events with a positive track and 26 events with a negative track, which failed an E/p cut. They could be real W events with an emission of high energy photon and a low p_T electron. Transverse mass distributions for $41 + 26 = 67$ events and the rest of 178 events are shown in Figure 5.4. We have 563 W^+ candidates and 558 W^- candidates passing the E/p cut, $E/p < 1.5$. The E/p cut efficiencies for electrons and positrons are estimated using these numbers:

$$\epsilon^-_{E/p} = (95.5 \pm 0.85)\%,$$

Variable		Cut value
Trigger requirements		
$\not{E}_T$	$>$	25 GeV
Electron cuts:		
χ^2_{PEM}	$<$	15
E_{EM}/E_{Had}	$<$	0.05
VTPC-hit-occupancy	$>$	0.5
R_{exit}	$>$	62.2 cm
Kinematical cuts:		
Electron E_T	$>$	25 GeV
Electron Isolation($I(R = 0.4)$)	$<$	0.1
$\not{E}_T$	$>$	25 GeV
M_{tr}	$>$	60 GeV/c^2
No other jet with E_T greater than 10 GeV		

Table 5.2: Selection parameters for the plug Ws for the track finding efficiency analysis. The trigger is based on the missing E_T trigger.

Variable		Cut value
E/p	$>$	2.5
$\Delta\phi$	$<$	0.04 radian
ΔR	$<$	10.0 cm

Table 5.3: Track selection parameters for the plug electrons.

$$\epsilon^+_{E/p} = (93.2 \pm 1.02)\%,$$

where $\epsilon^-_{E/p}$ represents the efficiency for electrons and $\epsilon^+_{E/p}$ represents the efficiency for positrons. The efficiencies show a slight discrepancy of 1.73σ significance.

Track finding efficiency for plug electrons

Selection criteria for the plug W candidates used for this study are shown in Table 5.2. We find 340 candidates which passed the selection criteria. Out of the 340 candidates, 262 candidates have passed the track selection criteria, given in Table 5.3. The CTC

track finding efficiency in the plug region is estimated to be

$$\epsilon_{\rm CTC}^{\rm PLUG} = \frac{262}{340} = (77.1 \pm 2.3)\%, \tag{5.6}$$

ignoring a small background contamination of $(2.4 \pm 1.3)\%$ estimated in Section 6.1. In the plug region, an electron track pass one to four innermost super-layers in the CTC. High track density and a distortion of the wire signals make the track reconstruction difficult. These conditions make the track finding efficiency lower than the central region. Either events with unsuccessful reconstruction of an electron track or background events would fail the W selection criteria. The track reconstruction efficiency could have a charge dependence though the CTC track is radially (i.e. high $p_{\rm T}$) enough to allow us a charge-independent track reconstruction. The events failed the track selection criteria are carefully studied using an event display and an "on-screen" manual track reconstruction program, which is detailed in Appendix A.3. Out of 78, 12 events are found to have a CTC track pointing to the cluster but fail the track selection criteria given in Table 5.3. For 31 events, a CTC track pointing to the cluster is manually recovered by picking up the wire hits by hand. The charge distribution of the $12 + 31 = 43$ candidates, shown in appendix A.3, shows same pattern as the 262 candidates indicating charge-independent reconstruction of electron tracks. For 10 events out of 78, no visible CTC wire hits has been found. These events could be background possibly due to photon or neutral pion productions. Adding the 43 candidates, 92.7% of electron tracks are reconstructed. Background candidates of 10 events give a background level $(3.0 \pm 1.4)\%$, which compares to $(2.4 \pm 1.3)\%$ estimated in Section 6.1.

We observe no indication of a charge-dependent track reconstruction. A track associated with the plug electron from W decay is straight enough to allow us find a track with equal efficiency for both electron and positron. We conclude that the CTC

Variable		Cut value
Trigger requirements:		
$\not\!\!E_T$	>	25 GeV
Electron cuts:		
E/p	<	1.5
Kinematical cuts:		
Electron E_T	>	20 GeV
$\not\!\!E_T$	>	20 GeV
M_{tr}	>	50 GeV/c^2
No other jet with E_T greater than 10 GeV		

Table 5.4: Selection parameters for the central Ws for the trigger efficiency analysis. The trigger condition is based on the missing E_T trigger.

track reconstruction has no significant charge dependence even in the plug region.

5.2.2 Trigger efficiency

Estimation of on-line trigger efficiencies is described.

Trigger efficiency for central electrons

The final W sample we use for the asymmetry analysis relies on the central electron trigger whose parameters are given in Table 4.1. The central electron trigger uses a track momentum information from the central fast tracker (CFT), which could have a charge dependence. In order to estimate the trigger efficiencies for electrons and positrons, we use a W sample triggered by the missing E_T trigger, whose selection criteria is given in Table 5.4. In this sample, we look at a charge of the track and a status of the central electron trigger. The sample contains 870 electrons and 845 positrons. We find that 27 electrons have failed the electron trigger and 27 positrons have failed the electron trigger. A trigger efficiency curve againt the electron E_T is shown in Figure 5.5. The trigger efficiencies are estimated to be $(96.9 \pm 0.58)\%$ for electrons and $(96.8 \pm 0.60)\%$ for positrons in an E_T range of the $W \rightarrow e\nu$ signal. They

Variable		Cut value
Electron cuts:		
$\chi^2_{\rm PEM}$	$<$	15
$E_{\rm EM}/E_{\rm Had}$	$<$	0.05
Kinematical cuts:		
Electron Isolation($I(R = 0.4)$)	$<$	0.1

Table 5.5: Selection parameters for the plug electromagnetic clusters for the trigger efficiency analysis.

are almost flat in the W signal range.

Trigger efficiency for plug electrons

Trigger requirements for plug electrons are shown in Table 4.3. The plug electron trigger does not use any track information. On the other hand, the lepton charge asymmetry measurement in the $W \rightarrow e\nu$ decay is influenced by a transverse mass threshold, as we mentioned in the beginning of this chapter. If the trigger efficiency is not flat above an off-line $E_{\rm T}$ threshold of 25 GeV, it could distort the transverse spectrum and change the asymmetry value. We measure the trigger efficiency curve versus the transverse energy of electron.

The sample is selected from the lepton inclusive sample extracted from the *Full production* based on the trigger information of the event type. Events which fired one of the lepton triggers other than the plug electron trigger are selected in this analysis. Since the electron $E_{\rm T}$ and the missing $E_{\rm T}$ has strong correlation in the $W \rightarrow e\nu$ event, the missing $E_{\rm T}$ trigger is also removed from the selection criteria in order to measure a trigger efficiency for the plug electron independent from the missing $E_{\rm T}$ trigger. One plug electromagnetic cluster which satisfies the criteria in Table 5.5 is required for the sample.

Trigger efficiencies as a function of the offline cluster $E_{\rm T}$ are shown in Figure 5.6

Variable		Cut value
Trigger requirements:		
central electron trigger		
Electron cuts:		
E/p	$<$	1.5
Kinematical cuts:		
Electron E_{T}	$>$	20 GeV
$\not{E}_{\mathrm{T}}$	$>$	20 GeV
M_{tr}	$>$	50 GeV/c^2
No other jet with E_{T} greater than 5 GeV		

Table 5.6: Selection parameters for the central Ws for the trigger efficiency analysis.

for the west and east plug modules. They are fitted by a function:

$$\epsilon_{trg}(E_{\mathrm{T}}) = \frac{1+b}{e^{a/E_{\mathrm{T}}}+b} \tag{5.7}$$

where E_{T} denotes the cluster E_{T} and a and b are fitting parameters.

The west module shows lower efficiency near the E_{T} threshold of 23 GeV than the east module. It is due to dead layers and quadrant gain constants described in Section 5.1.3. The west module had more dead layers and larger quadrant gain constants than the east module, which had not been corrected in the trigger. Discrepancy between the transverse energy measurements of the trigger cluster (see Section 3.1.3) and the offline cluster (see Section 3.2.5) causes slow saturation of the trigger efficiency versus the offline cluster E_{T}. The trigger cluster E_{T} is calculated with respect to $z = 0$ whereas the off-line cluster E_{T} uses a true event vertex reconstructed by the VTPC.

5.2.3 Electron identification cut efficiencies

Efficiencies for the identification parameters are estimated for electons and positrons individually. The parent sample is selected on a basis of the W kinematical cuts, which are coarse electron cuts, a missing E_{T} cut and a no-jet cut. The sample mostly

Parameter	ϵ^- (%)	ϵ^+ (%)
Conversion Cut	$100.0 - 0.17$	$100.0 - 0.17$
Isolation	97.2 ± 0.68	97.0 ± 0.71
Lshr	99.0 ± 0.42	98.4 ± 0.52
χ^2_{strip}	98.6 ± 0.48	97.4 ± 0.67
$E_{\rm Had}/E_{\rm EM}$	99.5 ± 0.30	99.1 ± 0.39
ΔX	99.6 ± 0.24	99.5 ± 0.30
ΔZ	99.5 ± 0.30	98.8 ± 0.46
All above	94.3 ± 0.96	91.1 ± 1.19

Table 5.7: Efficiencies for the identification parameters of the central electron.

Variable		Cut value
Trigger requirements:		
Plug electron trigger		
Electron cuts:		
R_{exit}	$>$	62.2 cm
E/p	$<$	2.5
Kinematical cuts:		
Electron $E_{\rm T}$	$>$	25 GeV
$\not{E}_{\rm T}$	$>$	30 GeV
M_{tr}	$>$	60 GeV/c^2
No other jet with $E_{\rm T}$ greater than 5 GeV		

Table 5.8: Selection parameters for the plug Ws for the trigger efficiency analysis.

contains W candidates and is almost independent from the electron identification cuts. Efficiencies estimated here are the fractions of the events which pass an identification cut value for individual identification parameters.

Electron identification cut efficiencies for central electrons

Efficiencies for the central-electron identification parameters are estimated with respect to the electrons which passed an E/p cut. The sample is selected from the inclusive electron sample extracted from the *Spin Cycle* data. The central electron trigger, described in Section 4.2.1, is required for this sample. The selection criteria are summarized in

Parameter	ϵ^- (%)	ϵ^+ (%)
Isolation	99 ± 1.4	98 ± 1.6
$\chi^2_{\rm PEM}$	93 ± 3.1	94 ± 2.5
$E_{\rm Had}/E_{\rm EM}$	$100 - 1.4$	99 ± 1.1
$\Delta\phi$	$100 - 1.4$	$100 - 1.1$
ΔR	94 ± 2.8	$100 - 1.1$
VTPC-hit-occupancy	94 ± 2.8	94 ± 2.5
All above	83 ± 4.6	86 ± 3.7

Table 5.9: Efficiencies for the identification parameters of the plug electron.

Table 5.6. The sample contains less than 0.7% background by virtue of a tight no jet cut of $E_{\rm T} > 5$ GeV. Efficiencies for the individual identification cuts are summarized in Table 5.7, where ϵ^- (ϵ^+) represents the efficiency for electrons (positrons).

Conversion cut, ΔX and ΔZ parameters could be charge dependent because they rely on the CTC track measurement. None of them shows significant difference between electrons and positrons. The total efficiencies for electrons and positrons show a slight discrepancy of 1.6σ significance.

Electron identification cut efficiencies for plug electrons

Efficiencies for the plug-electron identification parameters are estimated with respect to the electrons those passed an E/p cut of 2.5. The sample is selected from the inclusive electron sample extracted from the *Spin Cycle* data. The selection criteria are summarized in Table 5.8. The efficiencies for the individual identification parameters are estimated in Table 5.9, where ϵ^- (ϵ^+) represents the efficiency for electrons (positrons).

The parameters $\Delta\phi$ and ΔR could be charge dependent because they rely on the CTC track measurement. The efficiency of ΔR parameter for positrons is 2σ higher than that for electrons. This result is discussed in Chapter 7 focusing on the asymmetry measurement. The total efficiencies for electrons and positrons show a discrepancy of 0.5σ significance.

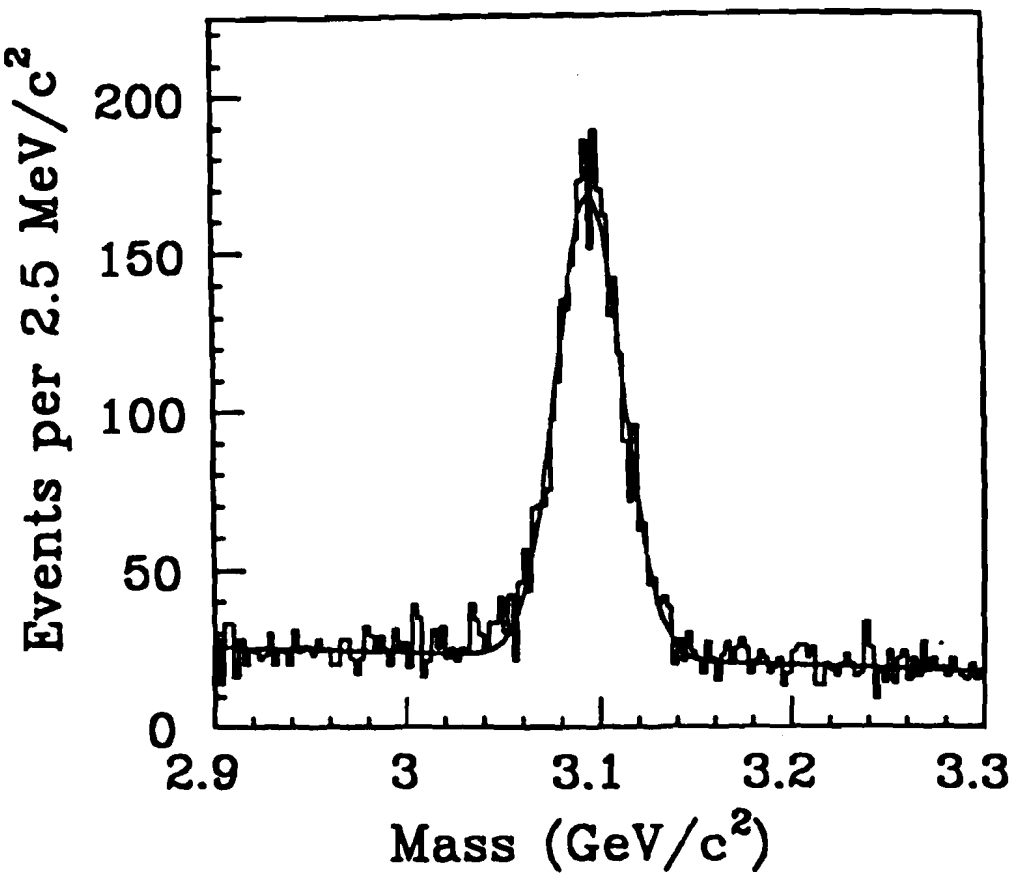

Figure 5.1: An invariant mass distribution for two-muon system near the J/ψ mass.

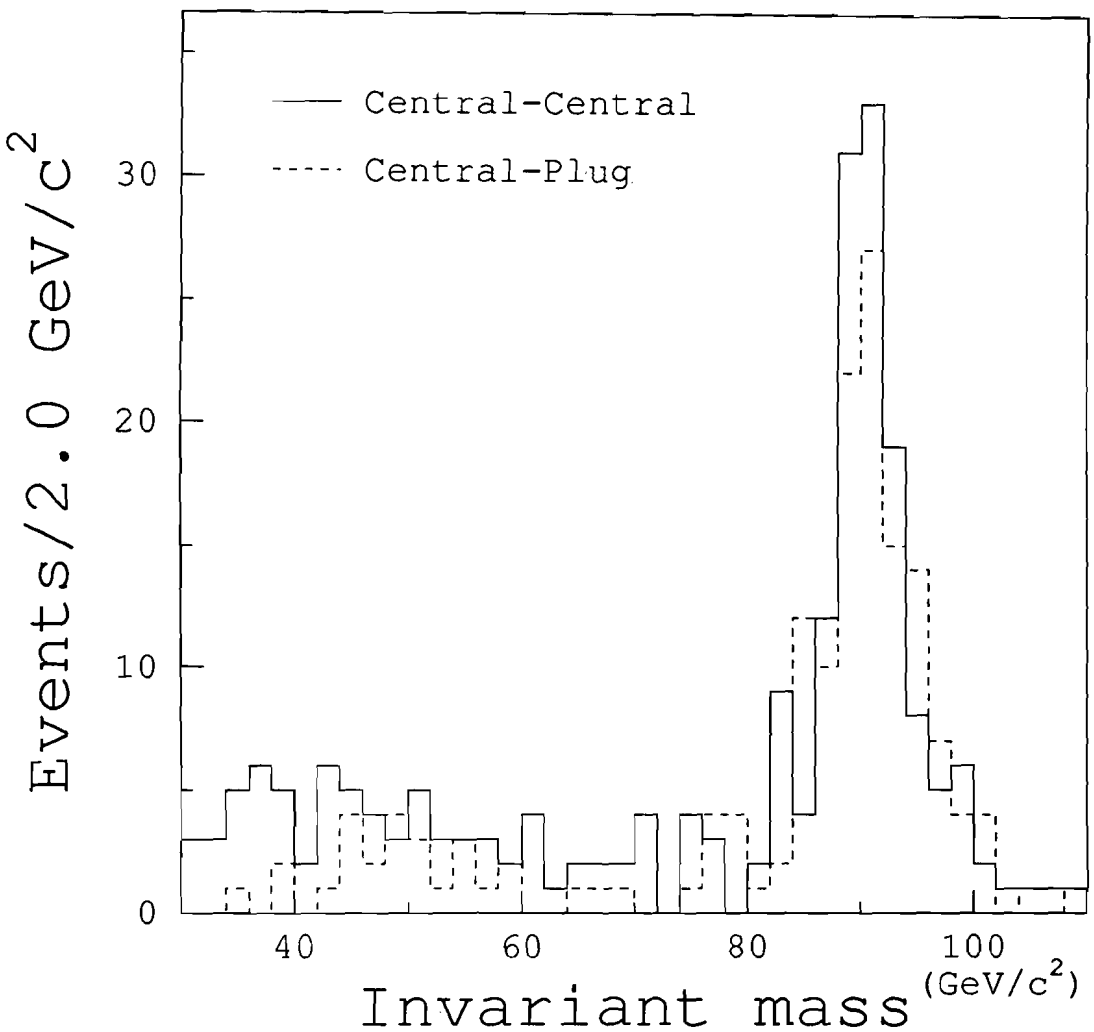

Figure 5.2: An invariant mass distribution for the central-plug Z candidates (solid). The distribution for the central-central Z candidates (dotted) is overlaid.

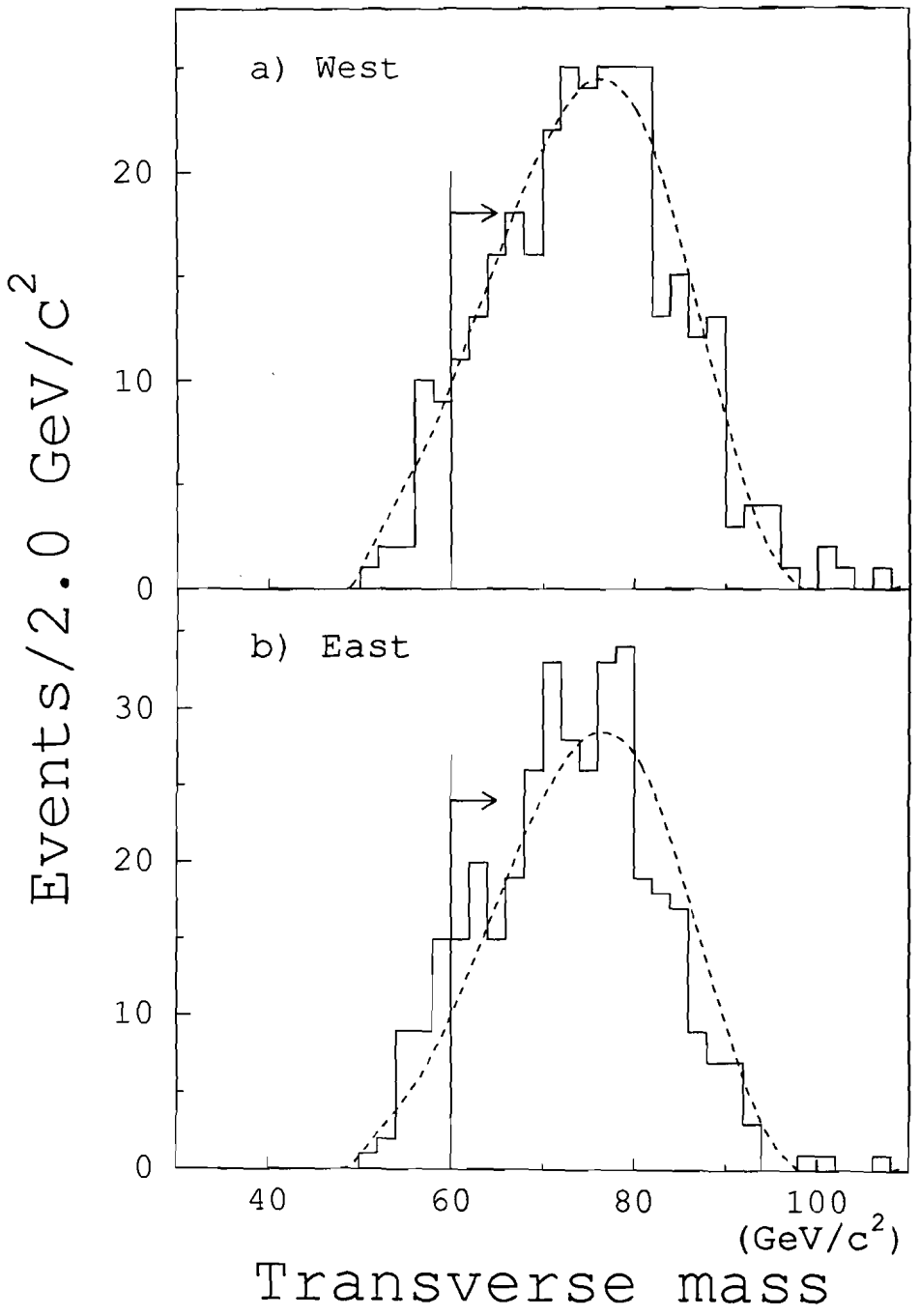

Figure 5.3: A transverse mass distribution for the plug W candidates (solid). The distribution from Monte Carlo simulation (dotted) is overlaid.

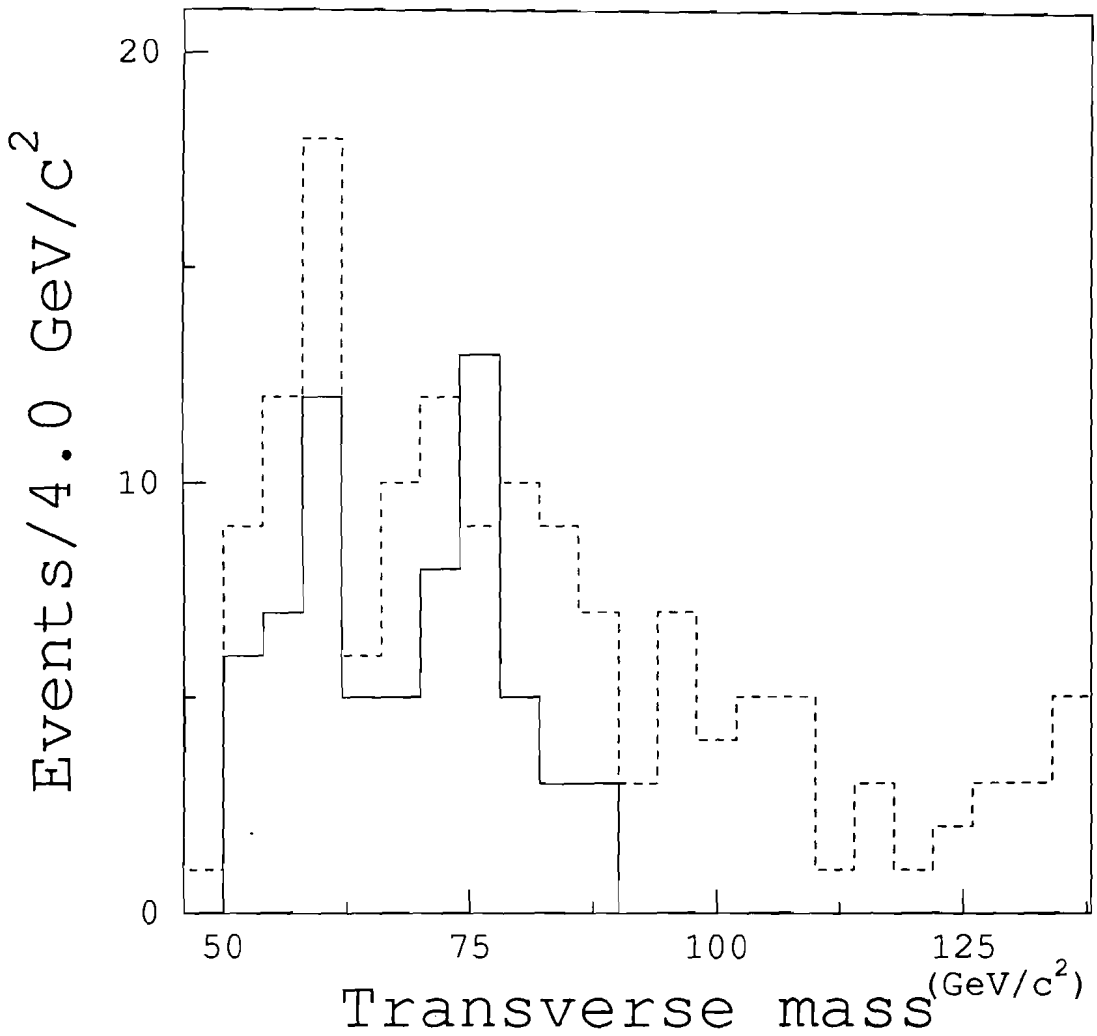

Figure 5.4: A transverse mass distribution for 67 W candidates (solid) with a low p_T electron. The distribution for the background candidates (dotted) is overlaid.

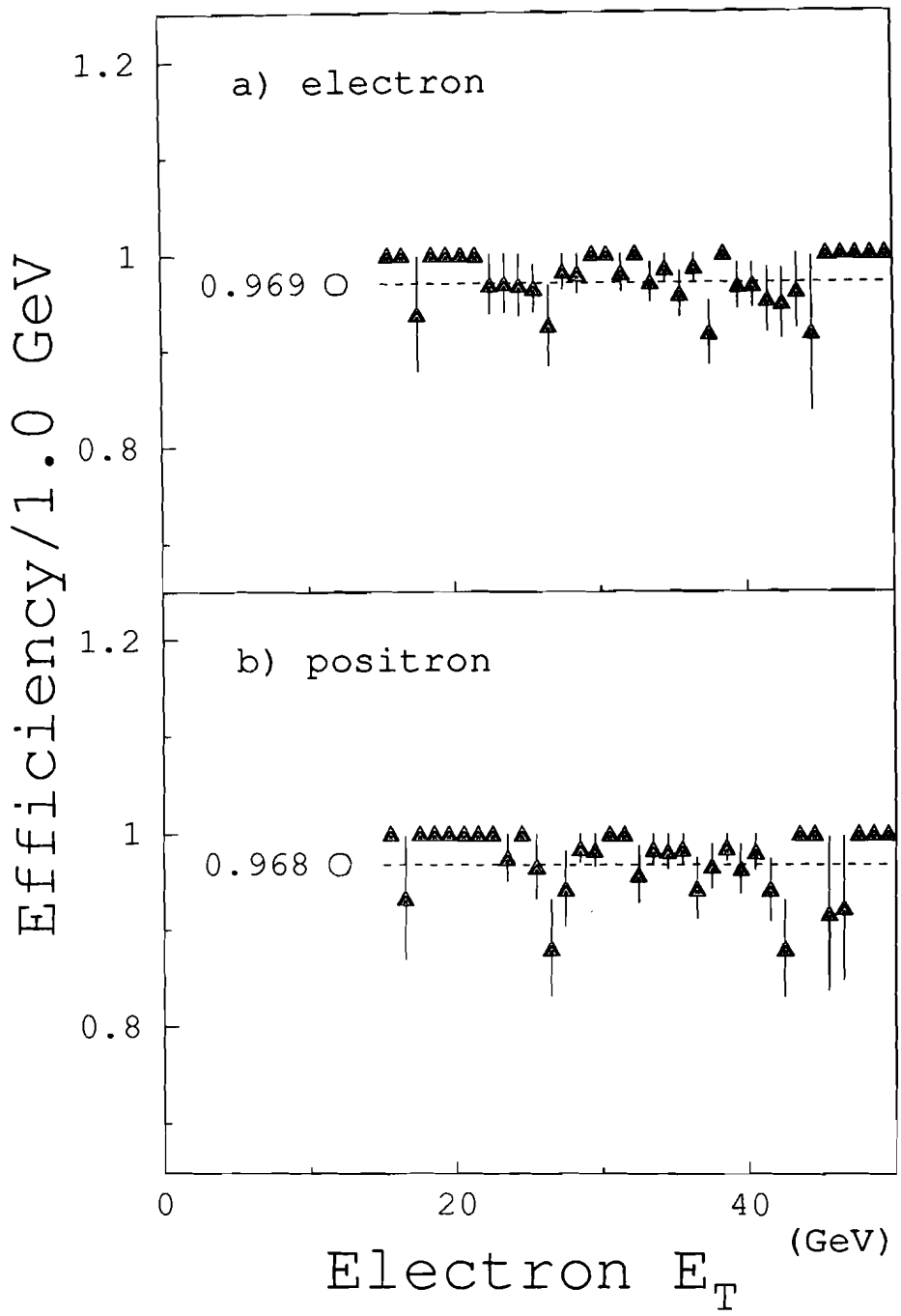

Figure 5.5: Trigger efficiency curves for central (a) electrons and (b) positrons as a function of cluster E_T. They are measured with respect to the offline electrons in the inclusive electron sample $E_T > 15$ GeV.

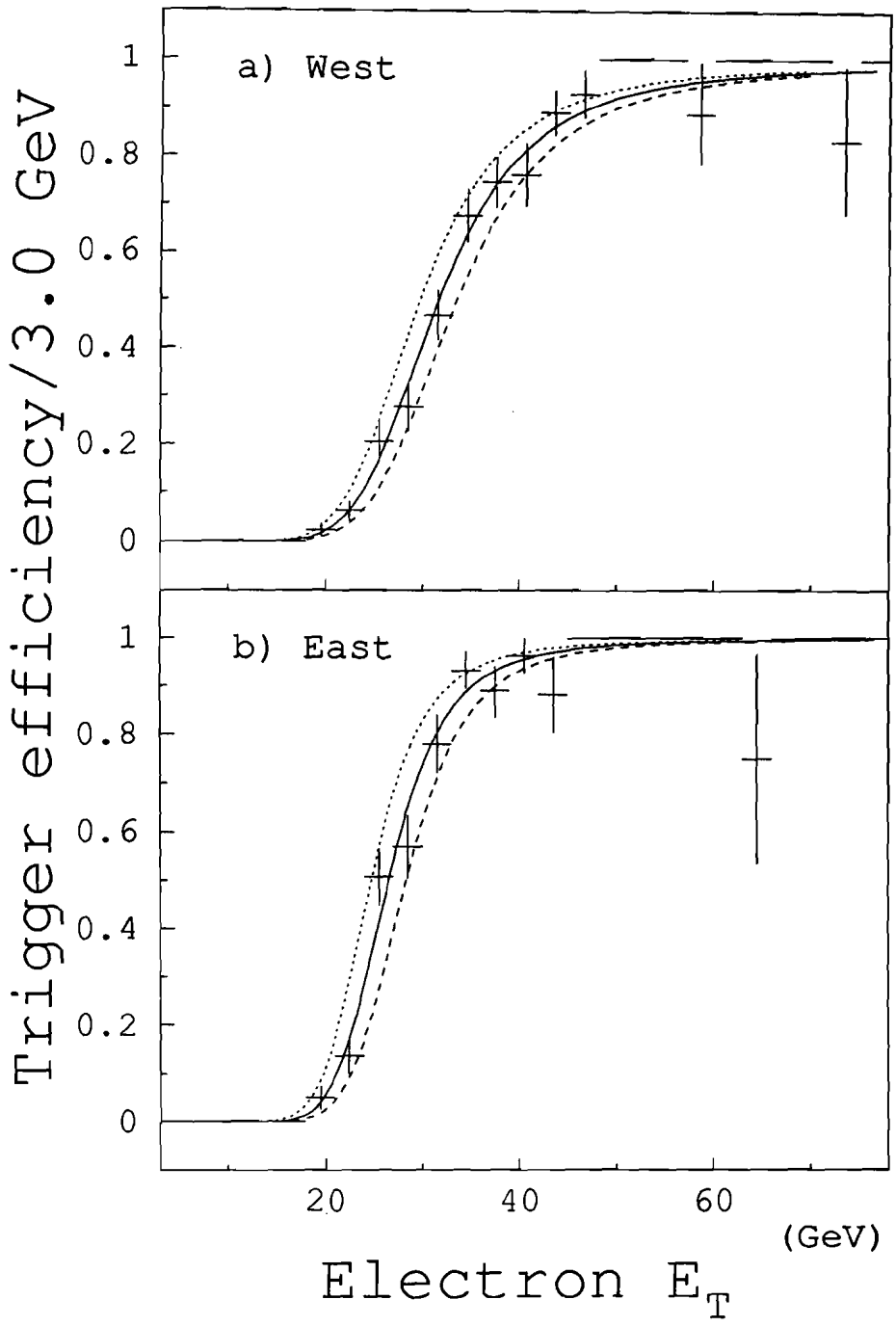

Figure 5.6: Trigger efficiency curves for plug electrons as a function of cluster E_T. (a) is for the west module and (b) is for the east module. One sigma band for the parameter a in Equation 5.7 is shown.

Chapter 6

Background

Two types of background, QCD jet and heavy quark production, contaminate a signal region of $W \rightarrow e\nu$ event. They are estimated in Section 6.1 followed by an estimation of the background from the other electroweak processes: $W \rightarrow \tau\nu \rightarrow e\nu\nu\nu$, $Z \rightarrow ee$, and $W \rightarrow \tau\tau \rightarrow e\nu X$.

6.1 Background from QCD jet and heavy flavour production

Many two-jet events from the QCD process are produced in $\bar{p}p$ collisions. QCD jets variously fluctuates in the fragmentation process. Electron misidentification occurs when a trajectory of a neutral pion overlaps with that of a charged pion inside a jet. The charged pion leaves a track in the CTC, whereas the neutral pion deposits most of its energy in the electromagnetic calorimeter, thus exhibiting an electron-like signature. A substantial amount of missing transverse energy can be generated when a part of jet escapes unseen through cracks in the detector, or simply due to a fluctuation in an amount of energy they deposit in the calorimeter. A signal region of the $W \rightarrow e\nu$

Variable		Cut value
Trigger requirements:		
Electron trigger		
Electron cuts:		
Electron identification cuts		
One jet with the cuts:		
E_{T}^{jet}	$>$	10 GeV
$E_{\mathrm{EM}}/E_{\mathrm{Tot}}$	$<$	0.85
Kinematical cuts:		
Electron E_{T}	$>$	20 GeV(25 GeV)
$\not{E}_{\mathrm{T}}$	$<$	10 GeV
No other jet with E_{T} greater than 10 GeV		

Table 6.1: Selection parameters for two-jet background sample

event also includes contributions from the $b\bar{b}$ production, since the semileptonic decay of the b-quark produces a real electron and a neutrino.

6.1.1 Method

The isolation variable introduced in Section 4.1 characterizes event kinematics where an electron is produced. An electron from the $W \rightarrow e\nu$ event is well isolated from the other particle activities, so that the isolation value is small. On the contrary, an electron-like object from a QCD jet and an electron from the b-quark decay are usually accompanied with some particle activities around the cluster, which make the isolation value large. Our background estimation relies on the distributions of the isolation variable for the W events and backgrounds.

A two-jet background sample is selected by the criteria shown in Table 6.1, where E_{T}^{jet} is the transverse energy of a jet and $E_{\mathrm{EM}}/E_{\mathrm{Tot}}$ is the electromagnetic energy fraction to the total cluster energy. The $E_{\mathrm{EM}}/E_{\mathrm{Tot}}$ is required to be smaller than 0.85 to select hadronic jets. We require $\not{E}_{\mathrm{T}}$ be smaller than 10 GeV to suppress the contamination of the real $W \rightarrow e\nu$ event. We select the events containing one electron-

like object which pass all the identification cuts, one hadronic jet and no other jet. Note that the isolation cut is not required on the electron-like object.

The W sample is selected by the criteria described in Section 4.3. The isolation cut is not required for this background estimation.

The background events and the W events are plotted on a scatter plot of the isolation variable (Iso) versus the missing transverse energy ($\not{E}_T$). A schematic diagram is shown in Figure 6.1. We define four regions:

A: $Iso < 0.1$ and $\not{E}_T < 10.0$ GeV

B: $Iso < 0.1$ and $\not{E}_T > 20.0$ GeV

C: $Iso > 0.3$ and $\not{E}_T < 10.0$ GeV

D: $Iso > 0.3$ and $\not{E}_T > 20.0$ GeV

The regions A, C, and D are signal regions for background candidates. Our $W \rightarrow e\nu$ sample selected in Section 4.3 corresponds to the region B. We make two assumptions. One is that the isolation variable and the missing transverse energy are uncorrelated for background events, in other words, the isolation variable for background events has the same distribution in regions of $\not{E}_T < 10$ GeV and $\not{E}_T > 20$ GeV. Another assumption is that all the events found in region D are background. Those assumptions allows us to estimate the background contamination in the sample region B by:

$$N_{BG} \sim \frac{N_A \cdot N_D}{N_C} \tag{6.1}$$

where N_X is the number of events found in the region X and N_{BG} is the number of background events in the region B.

6.1.2 Background in the central W sample

Figure 6.2 shows isolation distributions for two missing E_{T} regions: $0 < \not{E}_{\mathrm{T}} < 5$ GeV and $5 < \not{E}_{\mathrm{T}} < 10$ GeV, for the two-jet background sample. No significant correlation is found between these two distributions. We find $N_A = 405$, $N_B = 1721$, $N_C = 226$ and $N_D = 7$, yielding $N_{BG} = 13 \pm 4$. A faction of the background (f_{BG}) is then: $f_{BG} \equiv N_{BG}/N_B = (0.7 \pm 0.27)\%$. If we raise the E_{T}^{jet} threshold from 10 GeV to 20 GeV in the two-jet background sample (see Table 6.1), a background fraction becomes $(0.4 \pm 0.16)\%$. Contamination of the real W event in the region D will work to make N_D value smaller so that f_{BG} becomes smaller. We conclude that background contamination in the central W sample should be less than $(0.7 \pm 0.3)\%$. An isolation distribution for the central W sample is shown in Figure 6.3, where an isolation distribution for the background sample is overlaid.

6.1.3 Background in the plug W sample

For the background estimation in the plug region, the CTC track dependent cuts, E/p, $\Delta\phi$ and ΔR are not required in the electron identification. The reason is described below. Figure 6.4 shows isolation distributions corresponding to two missing E_{T} regions: $0 < \not{E}_{\mathrm{T}} < 5$ GeV and $5 < \not{E}_{\mathrm{T}} < 10$ GeV, for the two-jet background sample. No significant correlation is found between these two distributions. We find $N_A = 64$, $N_B = 889$, $N_C = 14$ and $N_D = 4$, yielding $N_{BG} = 19 \pm 5$. A fraction of the background (f_{BG}) is then: $f_{BG} \equiv N_{BG}/N_B = (2.4 \pm 1.20)\%$. If we require the CTC track dependent cuts, no event is found in a region of $Isolation > 0.1$ and $\not{E}_{\mathrm{T}} > 25$ GeV, that is, $N_D = 0$. It is expected that background contamination is reduced after the track requirements. Contamination of the real W event in the region D will work to make f_{BG} smaller. We conclude that background contamination in the plug W sample should be less than $(2.4 \pm 1.3)\%$. An isolation distribution for the plug W sample is shown in Figure 6.5,

Variables	central	plug
$Acc^{W}(W \rightarrow \tau\nu \rightarrow e\nu\nu\nu)$	$7.7 \pm 0.3\%$	13/2000
$Acc^{W}(W \rightarrow e\nu)$	$34.8 \pm 0.2\%$	$12.2 \pm 0.4\%$
$Acc^{W}(Z \rightarrow ee)$	7/500	3/500
$Acc^{W}(Z \rightarrow \tau\tau \rightarrow e\nu\nu X)$	26/1700	3/1700
$Acc^{Z}(Z \rightarrow ee)$	109/500	—
N_Z	193	—
N_W	1828	799

Table 6.2: Summary of acceptances for the W, Z and background events and the numbers of the W and Z candidates

where the distribution for the background sample is overlaid.

6.2 Other background sources

Backgrounds from the $W \rightarrow \tau\nu$, $Z \rightarrow ee$ and $Z \rightarrow \tau\tau$ processes are estimated. The estimation relies on the acceptances of these background processes to pass the kinematical and fiducial cuts for the $W \rightarrow e\nu$ and $Z \rightarrow ee$ processes. These acceptances are estimated using ISAJET Monte Carlo [31] and the CDF detector simulation (CDF-SIM) [32]. We calculate the acceptance for the $W \rightarrow e\nu$ event using the Monte Carlo simulation which generates W bosons from the leading order diagram $q\bar{q} \rightarrow W$ using a variety of proton structure functions and a simple parameterization of the W boson p_T (Fast Monte Carlo) [33, 34]. The acceptance values and the numbers of W and Z candidates, which we used in this background estimation, are summarized in Table 6.2, where N_W and N_Z are the numbers of the $W \rightarrow e\nu$ and $Z \rightarrow ee$ candidates and $Acc^{W,Z}(X)$ represents the acceptance for W and Z identification cuts corresponding to the process X.

6.2.1 $W \rightarrow \tau\nu$

If the tau lepton (τ) decays into an electron and neutrinos, the $W \rightarrow \tau\nu$ event leaves identical signature on the detector to the $W \rightarrow e\nu$ event. In the Monte Carlo, one tau lepton is forced to decay through the process: $\tau \rightarrow e\nu\nu$. We use a constant of the branching ratio: $BR(\tau \rightarrow e\nu\nu) = 0.175 \pm 0.004$ [29] for the background calculation. We calculated a fraction of the background using a formula:

$$f_{BG}(W \rightarrow \tau\nu) = \frac{Acc^W(W \rightarrow \tau\nu \rightarrow e\nu\nu\nu) \cdot BR(\tau \rightarrow e\nu\nu)}{Acc^W(W \rightarrow e\nu) + Acc^W(W \rightarrow \tau\nu \rightarrow e\nu\nu\nu) \cdot BR(\tau \rightarrow e\nu\nu)}. \quad (6.2)$$

We find $f_{BG}(W \rightarrow \tau\nu) = (3.7 \pm 0.4)\%$ for the central W sample and $f_{BG}(W \rightarrow \tau\nu) = (1.0 \pm 0.4)\%$ for the plug W sample.

6.2.2 $Z \rightarrow ee$

If one electron in the $Z \rightarrow ee$ process escapes from cracks of the detector, the event is misidentified as a $W \rightarrow e\nu$ event. A fraction of the background is estimated using a formula:

$$f_{BG}(Z \rightarrow ee) = \frac{Acc^W(Z \rightarrow ee) \cdot N_Z}{Acc^Z(Z \rightarrow ee) \cdot N_W} \quad (6.3)$$

where we normalize the number of the background events to the number of the $Z \rightarrow ee$ events we observed in the data.

We find $f_{BG}(Z \rightarrow ee) = (0.7 \pm 0.3)\%$ for the central W sample and $f_{BG}(Z \rightarrow ee) = (0.7 \pm 0.4)\%$ for the plug W sample.

6.2.3 $Z \rightarrow \tau\tau$

If one tau lepton (τ) decays into an electron and neutrinos and second tau lepton is lost in the detector, the $Z \rightarrow \tau\tau$ event may fake a $W \rightarrow e\nu$ event. In the Monte Carlo,

one tau lepton is forced to decay through the process: $\tau \rightarrow e\nu\nu$. We use a formula:

$$f_{BG}(Z \rightarrow \tau\tau) = \frac{Acc^{W}(Z \rightarrow \tau\tau \rightarrow e\nu\nu X) \cdot N_Z \cdot BR \cdot (2 - BR)}{Acc^{Z}(Z \rightarrow ee) \cdot N_W} \tag{6.4}$$

where BR is the branching ratio of the process: $\tau \rightarrow e\nu\nu$. We normalize the number of $Z \rightarrow \tau\tau$ events to the number of $Z \rightarrow ee$ candidates we observed in the data.

We find $f_{BG}(Z \rightarrow \tau\tau) = (0.24 \pm 0.05)\%$ for the central W sample and $f_{BG}(Z \rightarrow \tau\tau) = (0.06 \pm 0.04)\%$ for the plug W sample.

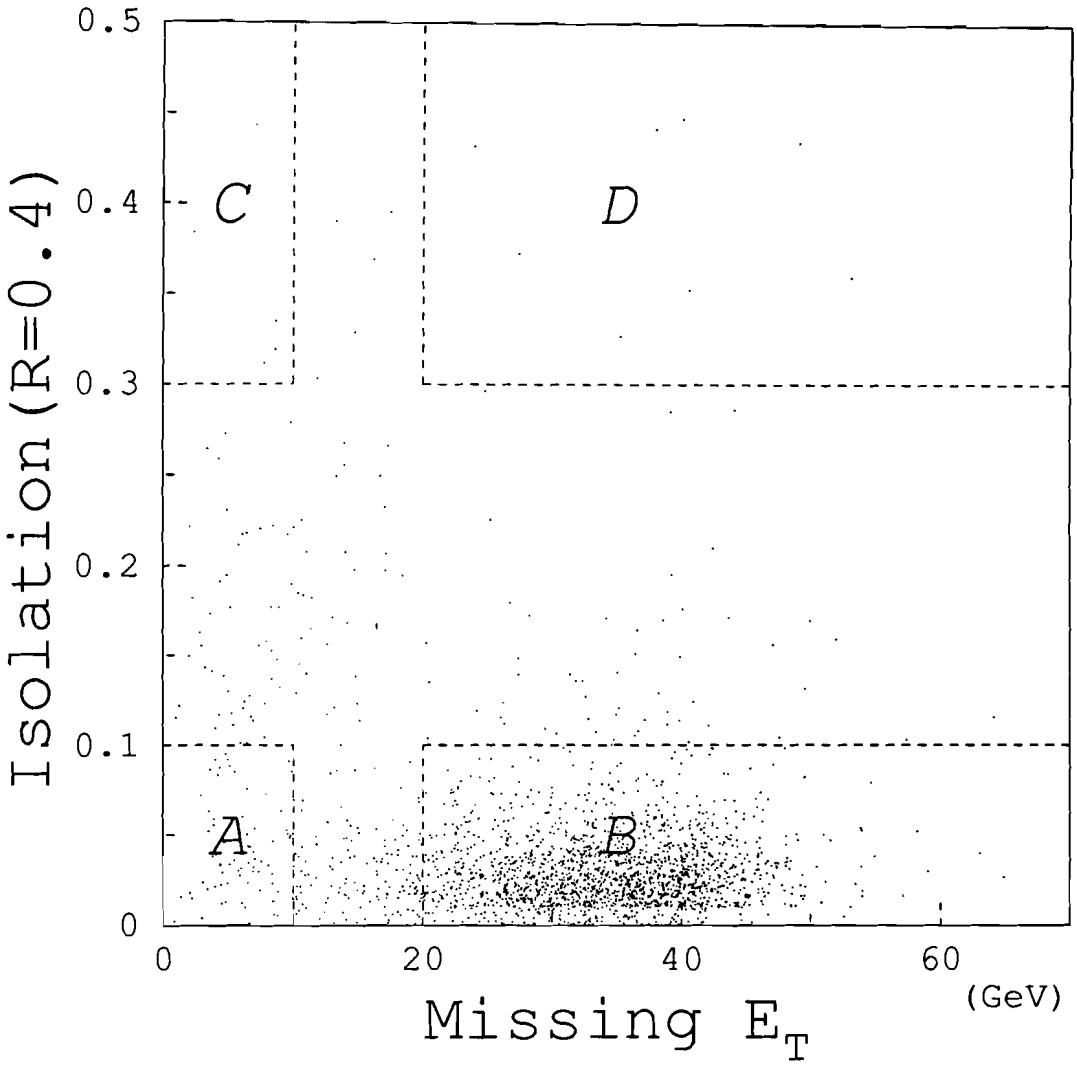

Figure 6.1: Schematic diagram of signal regions for W events and the background. The regions A, C and D contain mostly background. The region B is the W signal region.

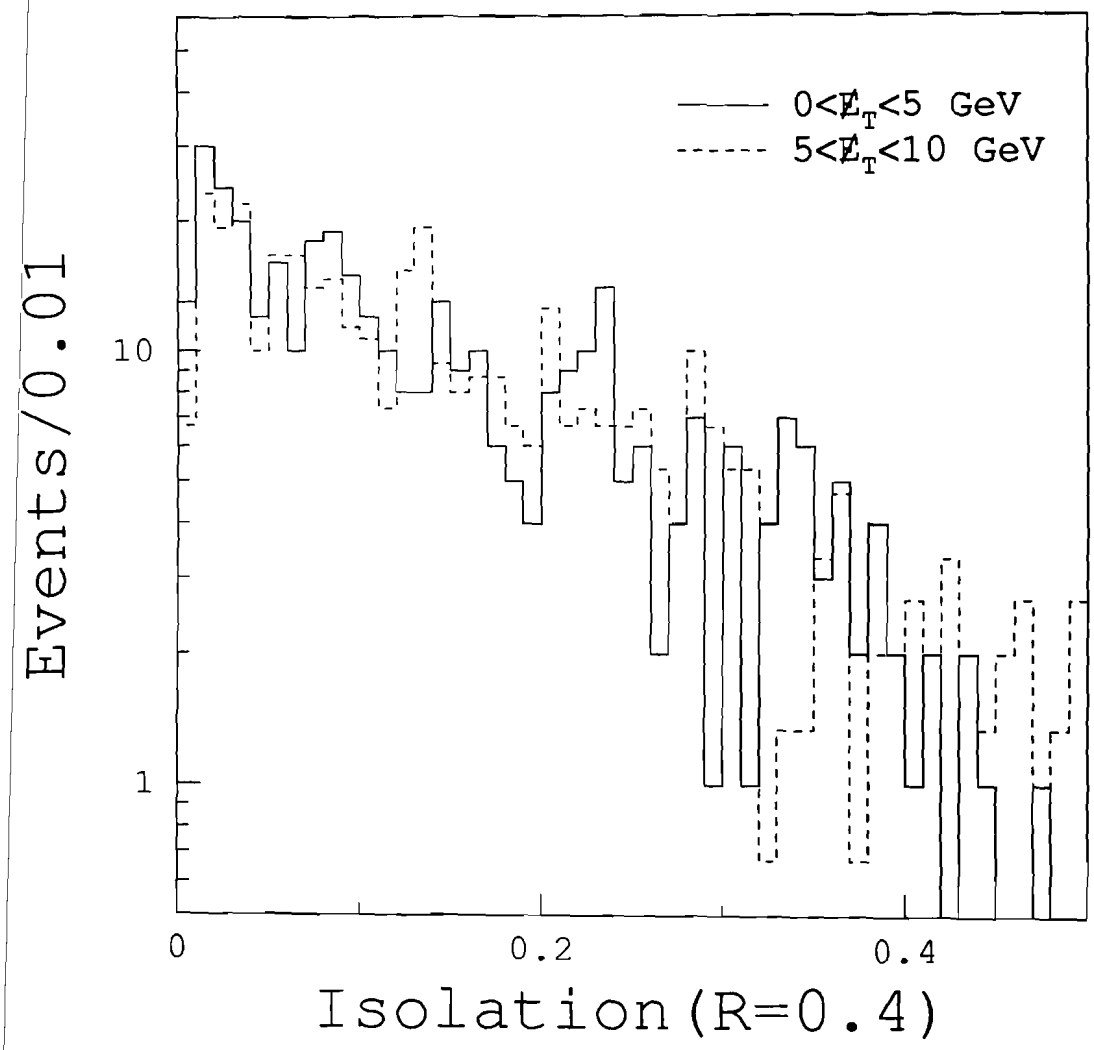

Figure 6.2: Isolation distributions for a two-jet background sample which contains a central electron-like cluster. The solid histogram crresponds to the $\not{E}_T$ region $0 < \not{E}_T < 5$ GeV and the dashed histogram corresponds to the $\not{E}_T$ region $5 < \not{E}_T < 10$ GeV.

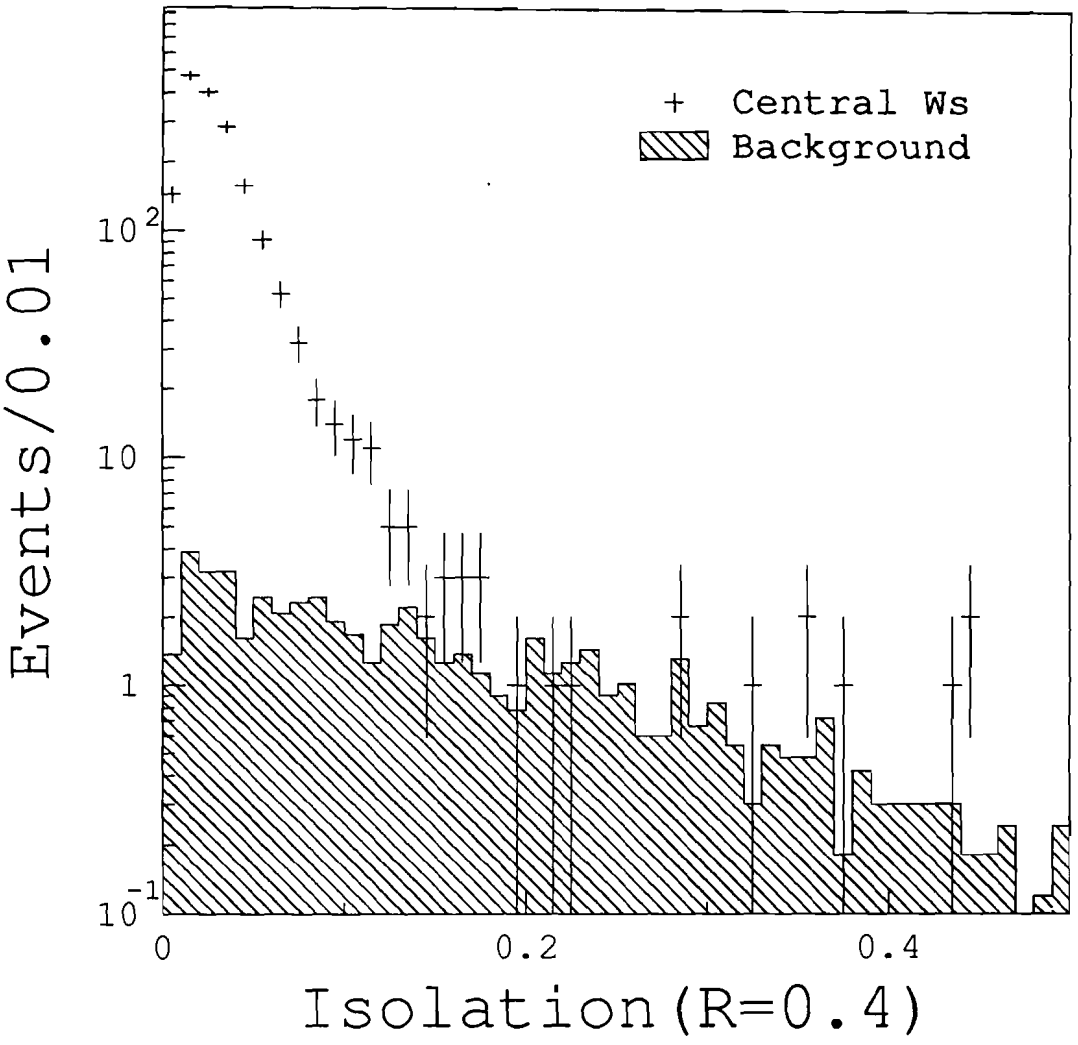

Figure 6.3: An isolation distribution for the central W sample. The distribution for the two-jet background sample is overlaid (shaded histogram), which is normalized by the number of events in the region of $Iso > 0.3$.

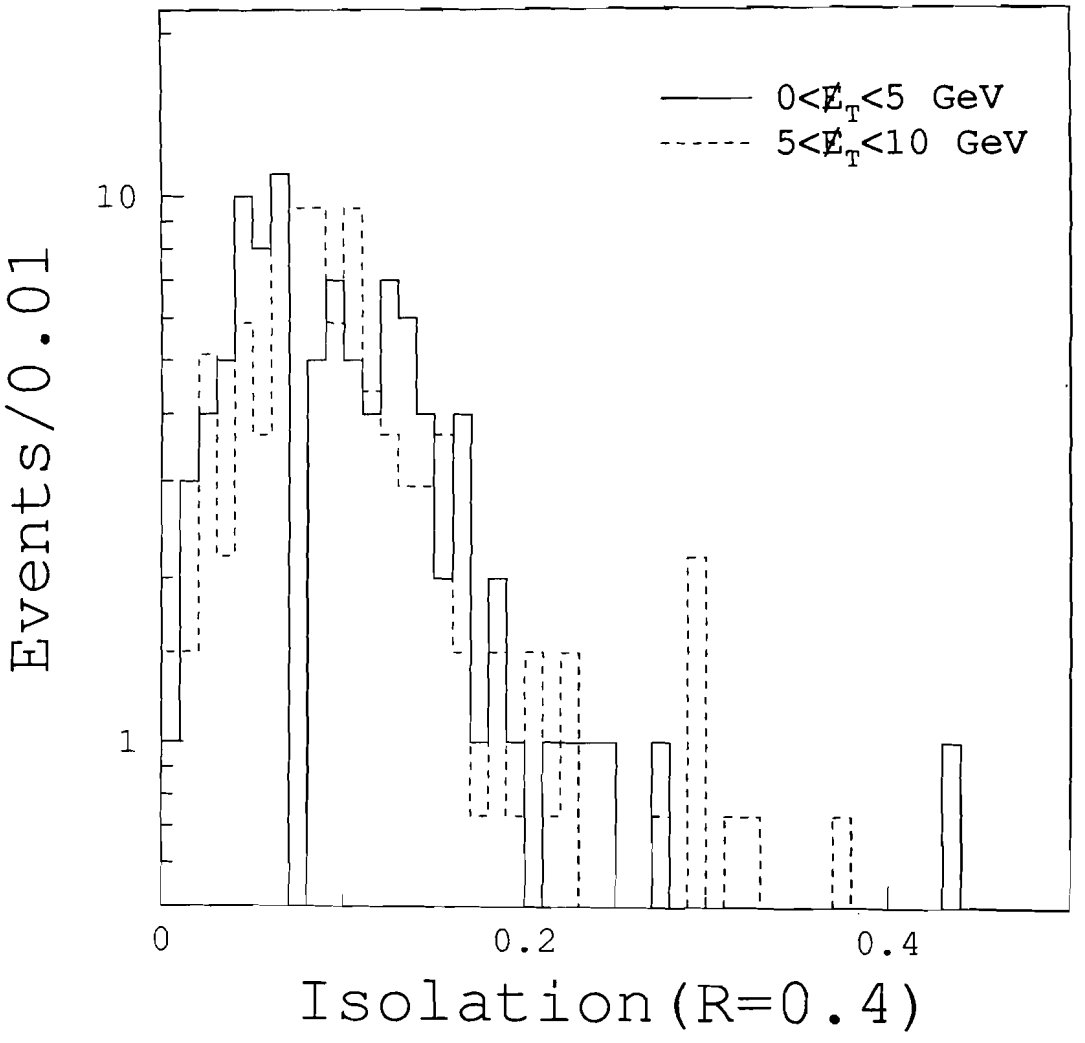

Figure 6.4: An isolation distributions for a two-jet background sample in the plug region. The solid histogram corresponds to the $\not{E}_T$ region $0 < \not{E}_T < 5$(GeV) and the dashed histogram corresponds to the $\not{E}_T$ region $5 < \not{E}_T < 10$(GeV).

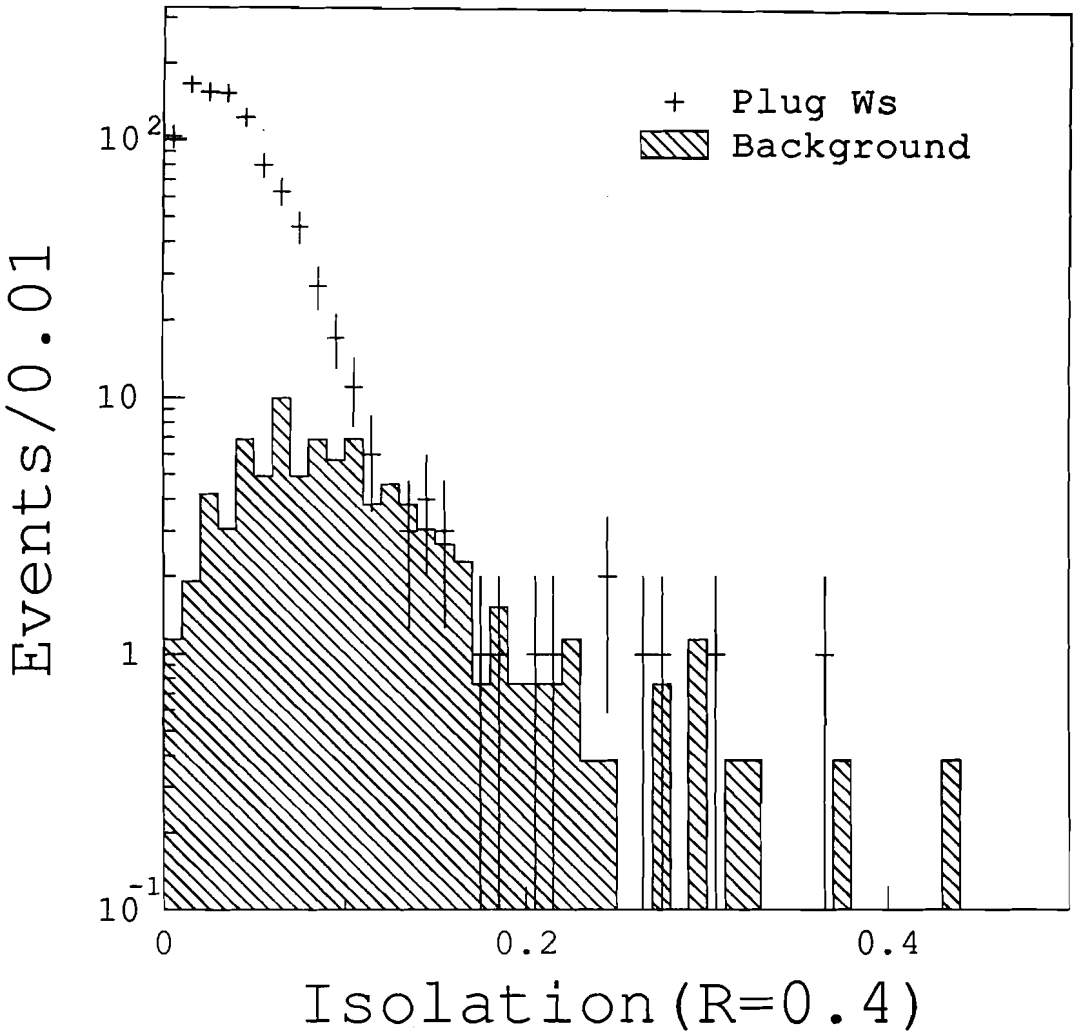

Figure 6.5: An isolation distributions for the plug W sample. The distribution for a two-jet background sample is overlaid (shaded histogram), which is normalized by the number of events in the region of $Iso > 0.3$.

Chapter 7

Asymmetry analysis

We measure lepton charge asymmetry in pseudo-rapidity distributions of leptons from W-boson decays. The samples described in Section 4.3 is used in this analysis. The analysis procedure is described in Section 7.1, together with a discussion of systematic uncertainties.

7.1 Analysis of lepton charge asymmetry

Lepton charge asymmetry is defined in Equation (1.16). Interchanging u-quark and d-quark in Equation 1.12 one obtains a pseudo-rapidity distribution for electrons in the $W^- \rightarrow e^-\bar{\nu}$ decay. Note that pseudo-rapidity distributions for electrons and positrons are anti-symmetric with respect to $\eta_\ell = 0$:

$$\frac{d\sigma^+(\eta_\ell)}{d\eta_\ell} = \frac{d\sigma^-(-\eta_\ell)}{d\eta_\ell}. \tag{7.1}$$

Using this relationship, one finds the lepton charge asymmetry (A_ℓ) is anti-symmetric with respect to $\eta_\ell = 0$:

$$A_\ell(\eta_\ell) = -A_\ell(-\eta_\ell), \tag{7.2}$$

Central Ws

η_e	-1.1	-0.9	-0.7	-0.5	-0.3	-0.1	0.1	0.3	0.5	0.7	0.9	1.1
N_+	15	50	87	78	73	66	59	89	107	106	74	17
N_-	20	80	99	116	86	75	78	89	88	67	65	18
A	-0.14	-0.23	-0.06	-0.20	-0.08	-0.06	-0.14	0.00	0.10	0.23	0.06	-0.03
ΔA	0.193	0.093	0.078	0.075	0.085	0.091	0.092	0.080	0.076	0.080	0.092	0.194

Plug Ws

η_e	-1.5	1.5
N_+	50	101
N_-	60	51
A	-0.09	0.33
ΔA	0.104	0.083

Table 7.1: Pseudo-rapidity distributions of electrons and positrons and the charge asymmetry.

and also

$$A_\ell(\eta_\ell) \equiv \frac{\sigma^+(\eta_\ell) - \sigma^-(\eta_\ell)}{\sigma^+(\eta_\ell) + \sigma^-(\eta_\ell)} = \frac{\sigma^+(\eta_\ell) - \sigma^+(-\eta_\ell)}{\sigma^+(\eta_\ell) + \sigma^+(-\eta_\ell)}. \tag{7.3}$$

In the central region, numbers of leptons are counted in a pseudo-rapidity interval $\Delta\eta = 0.2$. In the plug region, we calculate one asymmetry value using all the leptons in $1.32 < \eta < 1.7$. Numbers of leptons and the lepton charge asymmetry A_ℓ in each pseudo-rapidity bin are shown in Table 7.1, where ΔA denotes the statistical uncertainty. Using Equation (7.2), we can merge two A_ℓ values on $+|\eta|$ and $-|\eta|$ into one by taking an average:

$$A_\ell(|\eta|) = \frac{A_\ell(+|\eta|) - A_\ell(-|\eta|)}{2}. \tag{7.4}$$

where A_ℓ values are weighted by their errors. The averaged asymmetry values are plotted in Figure 7.1, where the theoretical predictions using various structure functions are overlaid.

7.2 Uncertainties

Uncertainties in the lepton charge asymmetry measurement are discussed below.

7.2.1 Charge dependence of the electron reconstruction efficiencies

We estimated the trigger efficiency, the track finding efficiency and the electron identification cut efficiency in Section 5.2. A discrepancy of the efficiencies between electrons and positrons changes the asymmetry values. For a small discrepancy of these efficiencies, $\Delta\epsilon = \epsilon^+ - \epsilon^-$, the lepton charge asymmetry defined in Equation (1.16) is written as follows:

$$\begin{aligned} A_\ell^{obs} &\equiv \frac{\epsilon^+ N^+ - \epsilon^- N^-}{\epsilon^+ N^+ + \epsilon^- N^-} \\ &= A_\ell^{true} + (1 + A_\ell^{true})\frac{\Delta\epsilon}{\epsilon^+}\frac{N^-}{N^+ + N^-} + O((\frac{\Delta\epsilon}{\epsilon^+})^2), \end{aligned} \tag{7.5}$$

where A_ℓ^{true} is an intrinsic true asymmetry and A_ℓ^{obs} is an observed asymmetry. In this case, the observed asymmetry value suffers a correction of approximately $\Delta\epsilon/\epsilon$.

If we take an average of the asymmetries at $+|\eta|$ and $-|\eta|$, the observed asymmetry is written as follows:

$$\begin{aligned} A_\ell^{obs}(|\eta|) &\equiv \frac{1}{2}\left(\frac{\epsilon^+ N_+(\eta) - \epsilon^- N_-(\eta)}{\epsilon^+ N_+(\eta) + \epsilon^- N_-(\eta)} - \frac{\epsilon^+ N_+(-\eta) - \epsilon^- N_-(-\eta)}{\epsilon^+ N_+(-\eta) + \epsilon^- N_-(-\eta)}\right) \\ &= A_\ell^{true}\left(1 + A_\ell^{true}\frac{\Delta\epsilon}{\epsilon^+} + O\left((A_\ell^{true}\frac{\Delta\epsilon}{\epsilon^+})^2\right)\right), \end{aligned} \tag{7.6}$$

where we use the relation $N_{\pm}(\eta) = N_{\mp}(-\eta)$ from Equation 7.1 to obtain the last line. By virtue of taking an average of the asymmetries at $+|\eta|$ and $-|\eta|$ a large correction term ($\sim \frac{\Delta\epsilon}{\epsilon}$) in Equation 7.5 cancels out. The asymmetry value now suffers a smaller correction of $\frac{\Delta\epsilon}{\epsilon}A^2$. The parameter ΔR for the electron identification in the plug region shows a slightly large difference 6% (2σ significant) between the efficiencies for electrons and positrons. This could be one reason we observed larger asymmetry at $\eta = +1.5$ than at $\eta = -1.5$. The asymmetry values can be corrected to -0.15 at $\eta = -1.5$ and $+0.27$ at at $\eta = +1.5$. These values are now compatible. The correction for the averaged asymmetry value (0.003) is small enough relative to the statistical uncertainty. All the other discrepancies of the trigger efficiencies and the offline electron reconstruction efficiencies between electrons and positrons are less than a few percents (see Section 5.2). We conclude that the corrections due to discrepancies between the electron and positron identification efficiencies are negligibly small relative to the statistical uncertainty.

7.2.2 Trigger efficiency in the plug

Trigger efficiencies were estimated in Section 5.2.2. The trigger efficiency for the central electron is 97% and flat in a transverse energy range where the W events are selected. For the plug electron, the trigger efficiency is not saturated enough around the transverse energy threshold of the electron identification. This is the reason why we set a higher transverse energy threshold in the plug region than in the central region. The non-flat trigger efficiency distorts the transverse mass distribution, and eventually changes the charge asymmetry value.

In order to estimate a size of the effect on the charge asymmetry measurement, we use the Fast Monte Carlo, which is described in Section 6.2. The events generated are weighted by an efficiency factor calculated from the efficiency curve, which is a function

Structure function	A_ℓ	A_ℓ^*(West/East)	correction (West/East)
HMRSB	0.157	$-0.170/+0.163$	$+0.013/-0.006$
HMRSE	0.133	$-0.150/+0.141$	$+0.017/-0.008$
EHLQ2	0.155	$-0.171/+0.162$	$+0.016/-0.007$
DFLM1	0.097	$-0.115/+0.105$	$+0.018/-0.008$
DFLM2	0.104	$-0.119/+0.111$	$+0.015/-0.007$
DFLM3	0.123	$-0.139/+0.131$	$+0.016/-0.008$
DO1	0.017	$-0.026/+0.021$	$+0.009/-0.004$
DO2	0.036	$-0.042/+0.039$	$+0.006/-0.003$
Average			$+0.016 \pm 0.003/-0.007 \pm 0.003$

Table 7.2: Asymmetry values in the plug for various structure functions. Here A_ℓ is the asymmetry for un-weighted statistics and A_ℓ^* is the asymmetry for statistics weighted by the trigger efficiency. Their discrepancies are also shown. The average and its error are for the first six structure functions.

of the transverse energy of the generated electron (see Section 5.2.2). The asymmetry values are calculated for the weighted statistics and also for the un-weighted statistics. The results are shown in Table 7.2, where A_ℓ is the asymmetry for un-weighted statistics and A_ℓ^* is the asymmetry for statistics weighted by the trigger efficiency. Since the differences between the asymmetry values for the weighted and un-weighted statistics are almost independent of structure functions, we calculated an average for the first six structure functions excluding DO1 and DO2, which show large discrepancy from our asymmetry measurement. We abtain correction constants of $+0.016 \pm 0.003$ for the west-plug point and -0.007 ± 0.003 for the east-plug point. The correction for the west plug is larger than that for the east plug, reflecting the fact that the trigger efficiency curve in the west plug is saturating more slowly than in the east plug.

7.2.3 Background contamination

Background contaminations in the $W \to e\nu$ events from QCD jet, heavy quark production and other electroweak processes were estimated in Chapter 6. We assume a symmetric background contamination for electrons and positrons. An effect of the

Central Ws

η_e	-1.1	-0.9	-0.7	-0.5	-0.3	-0.1
A_ℓ	-0.14	-0.23	-0.06	-0.20	-0.08	-0.06
bA_ℓ	-0.0010	-0.0016	-0.0004	-0.0014	-0.0006	-0.0004

	0.1	0.3	0.5	0.7	0.9	1.1
	-0.14	0.00	0.10	0.23	0.06	-0.03
	$+0.0001$	0.0	$+0.0007$	$+0.0016$	$+0.0004$	-0.0002

Plug Ws

η_e	-1.5	1.5
A_ℓ	-0.09	0.33
bA_ℓ	-0.0021	$+0.0078$

Table 7.3: Corrections for QCD jet and heavy flavor background corrections on the asymmetry measurement.

background contamination on the asymmetry measurement is written as follows:

$$\begin{aligned} A_\ell^{obs} &= \frac{N_+ - N_-}{(N_+ + N_-)(1+b)} \\ &= A_\ell^{true}(1-b) + O(b^2) \end{aligned} \tag{7.7}$$

where $b(\%)$ is a background contamination. A background contamination makes the obverved asymmetry smaller.

For a small background contamination ($b \ll 1$), the asymmetry value suffers a correction of bA. For the background from QCD jet and heavy quark production, no charge asymmetric effect is expected either in the parton process nor in the fragmentation process. Background contaminations from QCD jet and heavy quark, estimated in Section 6.1, were less than $(0.7 \pm 0.3)\%$ for the central region and less than $(2.4 \pm 1.3)\%$ for the plug region. The correction values calculated using Equation (7.7) are given in Table 7.3. The corrections for the central electrons are about 0.001 for all the pseudorapidity points, and are negligibly small compared to the statistical uncertainties. For

η	0.1	0.3	0.5	0.7	0.9	1.1	1.5
$A'_\ell(W \to \tau\nu \to e\nu\nu\nu)$	0.074	0.080	0.076	0.064	0.098	0.184	0.288
$A_\ell^{true}(W \to e\nu)$	0.015	0.043	0.070	0.093	0.109	0.117	0.159
$b(A'_\ell - A_\ell^{true})$	0.0021	0.0013	0.0002	−0.0010	−0.0004	0.0024	0.0012

Table 7.4: The asymmetry values from $W \to \tau\nu \to e\nu\nu\nu$ decays, in comparison with the asymmetry values from $W \to e\nu$ decays. The transverse mass threshold is 50 GeV/c^2 for $\eta = 0.1 - 1.1$ and 60 GeV/c^2 for $\eta = 1.5$.

the plug electrons, an uncertainty of the background estimation was discussed in Section 6.1 and the uncertainties are −0.0021 at $\eta = -1.5$ and +0.0078 at $\eta = 1.5$. These uncertainties are added to the systematic uncertainties of the asymmetry at $\eta = \pm 1.5$.

Electroweak processes $W \to \tau\nu$, $Z \to ee$, $Z \to \tau\tau$, have charge asymmetry in consequence of the standard weak coupling. Especially, tau leptons in $W \to \tau\nu$ decays, have the same charge asymmetry as electrons in $W \to e\nu$ decays. Asymmetric background contaminations affect the asymmetry measurement as follows:

$$\begin{aligned} A_\ell^{obs} &= \frac{N_+ - N_- + n_+ - n-}{N_+ + N_- + n_+ + n-} \\ &= A_\ell^{true} + b(A'_\ell - A_\ell^{true}) + O(b^2), \end{aligned} \tag{7.8}$$

where n^+ and n^- are the numbers of background positrons and electrons, $b(\%)$ is the background contamination and A'_ℓ is the asymmetry value for the background. If A'_ℓ is equal to A_ℓ^{true}, an observed asymmetry suffers no change in first order.

We calculate the charge asymmetry from $W \to \tau\nu \to e\nu\nu\nu$ decays using the ISAJET Monte Carlo of version 6.25 and the EHLQ set-1 structure function [35]. The results are shown in Table 7.4, in comparison with the asymmetry values of the $W \to e\nu$ decay. The asymmetry values for the $W \to e\nu$ decay are calculated using the cross section formulae, Equation (1.12) and the EHLQ set-1 structure function. The $W \to \tau\nu$ background was estimated to be $(3.7 \pm 0.4)\%$ for the central Ws and $(1.0 \pm 0.4)\%$ for the plug Ws. All the correction values calculated using Equation (7.8)

Z candidates with two central electrons			
	e^+	e^-	A'_ℓ
$-1.1 < \eta < 0.0$ (West)	55	51	0.04 ± 0.097
$0.0 < \eta < 1.1$ (East)	54	58	-0.04 ± 0.094

Z candidates with central and plug electrons			
	e^+	e^-	A'_ℓ
$-1.7 < \eta < -1.32$ (West)	9	5	0.3 ± 0.25
$1.32 < \eta < 1.7$ (East)	13	16	-0.1 ± 0.18

Table 7.5: A charge distribution of $Z \to ee$ events.

are negligibly small compared to the statistical uncertainties.

The $Z \to ee$ and $Z \to \tau\tau$ decays have small charge asymmetry. A charge distribution for the Z candidates of two central electrons and of a central electron and a plug electron are shown in Table 7.5. The Z candidate is required to have one good central electron which pass the electron identification cuts given in Table 4.2 and have another electromagnetic cluster and have their invariant mass within $70 < M_{inv} < 110$ GeV/c^2. Taking an average of the asymmetry values at $-|\eta|$ and $+|\eta|$, we obtain $A' = -0.04 \pm 0.067$ for the central region and $A' = -0.2 \pm 0.15$ for the plug region. From Table 7.1, the corresponding asymmetry for $W \to e\nu$ events is $A = +0.091 \pm 0.024$ for the central region and $A = +0.210 \pm 0.061$ for the plug region. The $Z \to ee$ background were estimated to be $(0.7 \pm 0.3)\%$ for the central region and $(0.7 + 0.4)\%$ for the plug region. The corrections are estimated to be -0.0009 ± 0.0005 for the central region and -0.003 ± 0.002 for the plug region, using Equation (7.8). These corrections are neglected compared to the statistical uncertainties.

The $Z \to \tau\tau$ background was estimated to be $(0.24 \pm 0.05)\%$ for the central region and $(0.06 \pm 0.04)\%$ for the plug region. These values are smaller than the $Z \to ee$ contamination. Since the electron from the tau decay follows the direction the tau momentum, the tau decay ($\tau \to e\nu\nu$) does not change the $Z \to \tau\tau$ decay asymmetry

so much. The $Z \to \tau\tau$ contamination is smaller than the $Z \to ee$ contamination. The correction due to the $Z \to \tau\tau$ background is smaller than the correction due to the $Z \to ee$ background.

7.2.4 Misidentification of the electron charge

Our charge asymmetry measurement relies on the charge determination by the central tracking chamber. If the charge misassignment occurs with probabilities p^+ and p^-, where $p^+(p^-)$ is the probability to misidentify a positive (negative) track to a negative (positive) track, the observed asymmetry is written as follows:

$$\begin{aligned} A_\ell^{obs} &= \frac{N_+ + p^- N_- - p^+ N_+ - (N_- + p^+ N_+ - p^- N_-)}{N_+ + N_-} \\ &= A_\ell^{true} - 2p^+ \frac{N_+}{N_+ + N_-} + 2p^- \frac{N_-}{N_+ + N_-} + O(p^{\pm 2}) \end{aligned} \tag{7.9}$$

If p^+ is equal to p^-, the asymmetry value suffers a correction of $2p^+ A_\ell^{true}$.

As we mentioned in Section 2.3.3, the central tracking chamber has a momentum resolution of $\delta p_T/p_T = 0.0011 p_T$ (GeV/c) in the central region and $\delta p_T/p_T = 0.005 p_T$ (GeV/c) in the plug region. For electrons with transverse energy of 40 GeV, the momentum resolution becomes 4.4% in the central region and 20% in the plug region. These resolutions correspond to widths of the E/p distributions (see Figures 4.4 and 4.9), including the energy resolution of the calorimetry. The distribution tail extrapolated beyond $E/p = 0$ gives a measure of the probability of charge misidentification.

In the central region, the mean value of the E/p distribution is more than 20σ away from $E/p = 0$. In addition to that, we find no $Z \to ee$ candidate whose electrons have samely-charged tracks. We conclude that the probability of the charge misidentification is negligibly small ($p^\pm \ll 1$) in the central region.

	Number of events	Wrong sign	Correct sign
e^+	287	3	284
e^-	319	7	312

Table 7.6: Charge misidentification probabilities in the plug region estimated using the CDF detector simulation.

In the plug region, the track momentum resolution is good enough to identify the electron charge in an ideal case. A track in the plug region tends to be obscured by neighboring tracks because the track is reconstructed using only three to four innermost CTC super-layers close to the beam axis. Pattern recognition of the tracks sometimes fails to pick up all the wire hits belonging to the track. These situations make it difficult to achieve the ideal momentum resolution. Figure 7.2 shows the number of CTC wire hits in super-layer 2 used in the track reconstruction for the plug electrons in the $W \to e\nu$ events.

In order to estimate the probability of the charge misidentification, $W \to e\nu$ events are generated by the ISAJET Monte Carlo and simulated by the CDF detector simulation (CDFSIM). The track reconstruction algorithm finds almost same number of CTC wire hits for the real and Monte Carlo $W \to e\nu$ events (see Figure 7.2). The numbers of correctly-signed and wrongly-signed electrons are given in Table 7.6. From the table, we obtain the charge misidentification probabilities p^+ and p^-:

$$p^+ = 0.010 \pm 0.006 \tag{7.10}$$

$$p^- = 0.022 \pm 0.008. \tag{7.11}$$

The charge misidentification probability is also measured using real $Z \to ee$ events where one electron is detected in the central region and another in the plug region. Both two electrons are required to pass the electron identification cuts given in Table 4.2 and 4.4 for this Z event sample. The charge of the plug electron track is compared to the charge of the central electron. We observe 27 candidates and no charge-misassignment

	$\eta = -1.5$		$\eta = +1.5$		Average	
A^{obs}	-0.091	± 0.104	$+0.329$	± 0.083	$+0.236$	± 0.066
1) Trigger efficiency	$+0.016$	± 0.003	-0.007	± 0.003		
$A^{obs'}$	-0.075	± 0.105	$+0.332$	± 0.084	$+0.232$	± 0.067
2) bA		-0.0021		$+0.0078$		
$A^{obs''}$	-0.075	$^{+0.105}_{-0.107}$	$+0.332$	$^{+0.092}_{-0.084}$	$+0.227$	$^{+0.071}_{-0.068}$
3) $2pA$	-0.0024	$^{+0.0024}_{-0.0131}$	$+0.0103$	$^{+0.0056}_{-0.0103}$		
$A^{obs'''}$	-0.077	$^{+0.105}_{-0.108}$	$+0.342$	$^{+0.093}_{-0.085}$	$+0.234$	$^{+0.072}_{-0.068}$

Table 7.7: Summary of the charge asymmetry and its uncertainties in the plug region. 1) is the correction for the unsaturated trigger efficiency, 2) is the uncertainties from the background contamination of QCD jets and heavy flavor production and 3) is the correction and the associated uncertainties from the misidentification of the electron charge. The asymmetry $A^{obs'}$, $A^{obs''}$, and $A^{obs'''}$ are successively corrected by the correction 1), 2), and 3).

is found. The charge misidentification probability is found to be

$$p^{\pm} < 0.085\,(90\%C.L.). \tag{7.12}$$

We conservatively take this limit as the errors for the probability calculated from the Monte Carlo simulation. We take an average of p^+ and p^- given by Equations (7.10) and (7.11), and obtain the error given by Equation (7.12):

$$p^{\pm} = 0.016^{+0.085}_{-0.016}. \tag{7.13}$$

7.2.5 Dead channels

Sixteen dead channels have been found during the 1988-1989 run in the plug region. They are given in Appendix A.2. Dead channels may distort the pseudo-rapidity distribution of electrons and may change the asymmetry value. The effect of the dead channels on the asymmetry measurement are simulated in the Fast Monte Carlo. We compare the asymmetry values with and without the dead-channel simulation. The

differences between the asymmetry values are estimated to be less than the statistical error of Monte Carlo of $\Delta A = 0.003$ and is negligible compared to the statistical uncertainties of the measured asymmetry values.

7.3 Summary

The asymmetry values in the central region are found to be free from any background and any systematic uncertainties within the statistical uncertainties.

In the plug region, we apply several corrections and add uncertainties to the measurement. They are summarized in Table 7.7. We first apply the correction of the unsaturated trigger efficiency, which is described in Section 7.2.2, on the asymmetry values of $\eta = -1.5$ and $+1.5$. Then we add the uncertainties from the background contamination of QCD jets and heavy quark production (bA), which are estimated in Section 7.2.3. The asymmetry values are, finally, corrected by the probability of charge misassignment ($2pA$), which is described in Section 7.2.4. We use the charge misidentification probability given by Equation (7.13) for the calculation.

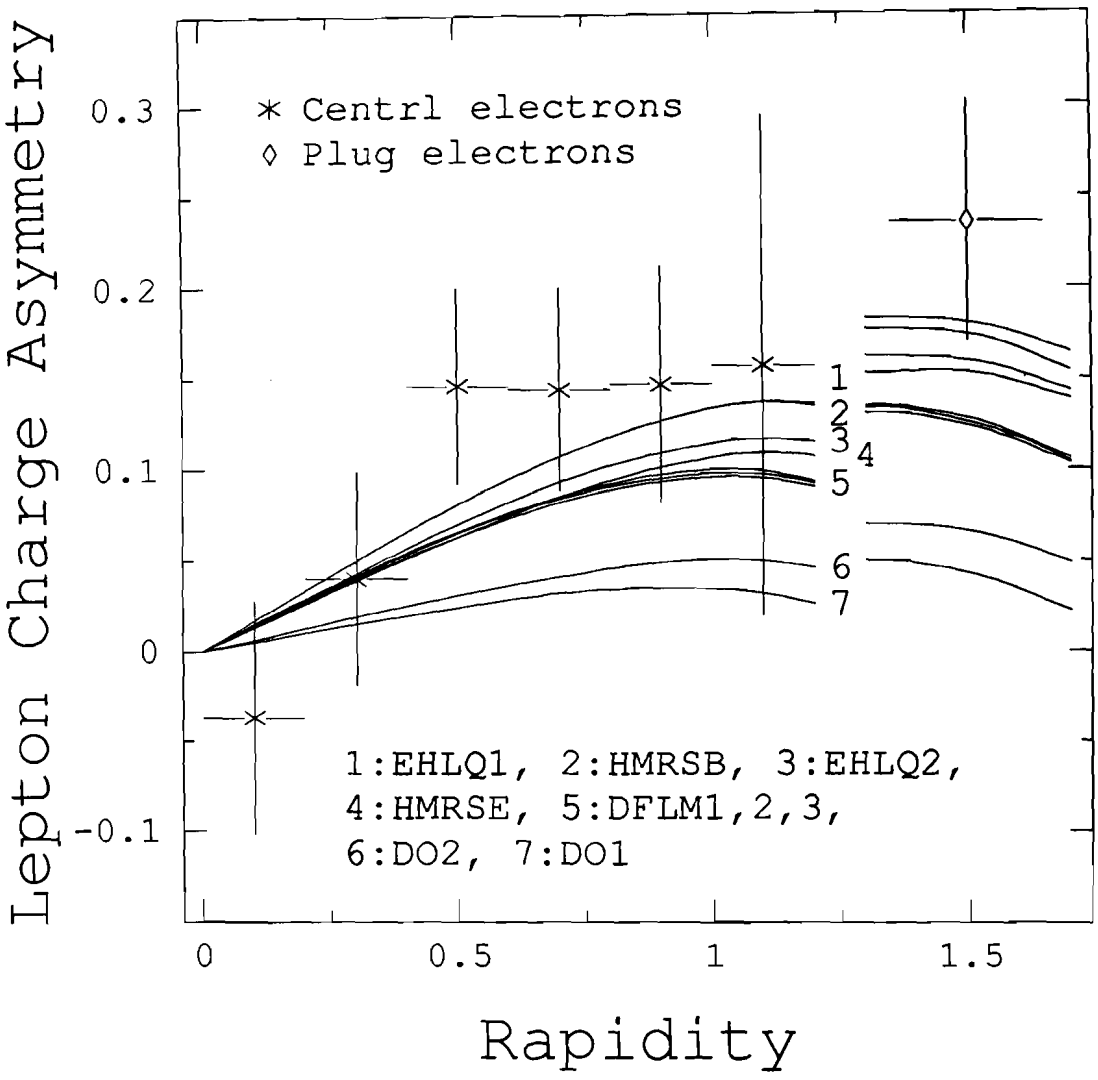

Figure 7.1: Charge asymmetry distribution without corrections. The transverse mass thresholds are 50 GeV/c^2 for the central region and 60 GeV/c^2 for the plug region.

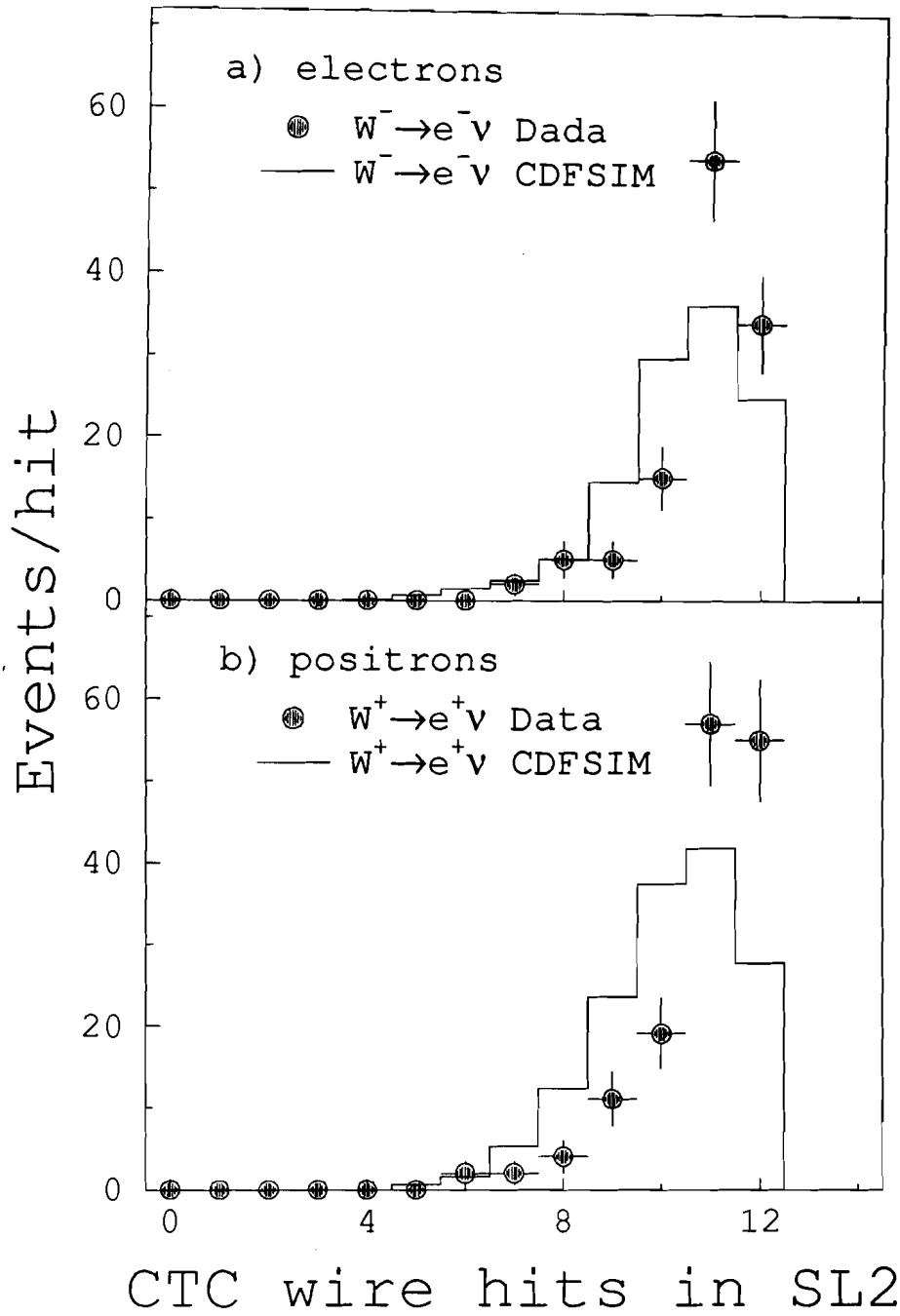

Figure 7.2: Number of CTC wire hits in super-layer 2 used for the track reconstruction in the plug region. a) is for the $W^- \rightarrow e^-\bar{\nu}$ events and b) is for the $W^+ \rightarrow e^+\nu$. Results from the CDFSIM detector simulation is overlaid (histogram). The Monte Carlo $W \rightarrow e\nu$ events were genarated by the Isajet Monte Carlo.

Chapter 8

Results and discussion

The final results of the lepton charge asymmetry measurement are shown in Table 8.1. For the central region, the asymmetry value at η is the average of the asymmetry values at $\pm\eta$ given in Table 7.1. For the plug point, we have made several corrections as summarized in Table 7.7.

8.1 Theoretical predictions

We used four kinds of input proton structure functions which are parametrized by Eichten, Hinchliffe, Lane, and Quigg (EHLQ) [35] and by Duke and Owens (DO) [36] and by Harriman, Martin, Roberts, and Stirling (HMRS) [37] and by Diemoz, Ferroni, Longo, and Martinelli (DFLM) [38]. HMRS and DFLM sets of structure functions are based on recent data from lepton deep-inelastic scattering (DIS) experiments whereas EHLQ and DO sets are based on realtively older data. Some of the parametrization are shown in Table 8.2. EHLQ firstly fit a sea quark distribution, $\mathcal{F}_2(x, Q_0^2)$ form factor, and a gluon distribution, which are given as combinations of the parton desity distributions by Abramowicz *et al.* [39]. They deduce each parton distribution so that their combinations reproduce these distributions. They provide two sets of structure

η_e	0.1	0.3	0.5	0.7	0.9	1.1	1.5
A	-0.037	0.040	0.146	0.144	0.147	0.057	0.234
ΔA	0.065	0.059	0.054	0.056	0.065	0.137	$^{+0.072}_{-0.068}$

Table 8.1: Charge asymmetry in the central and plug W events. The transverse mass thresholds are 50 GeV/c^2 for $\eta = 0.1 \sim 1.1$ and 60 GeV/c^2 for $\eta = 1.5$.

function. Set 1 (Set 2) is characterized by a $\Lambda_{\rm QCD}$ value, 180 MeV (290 MeV), which corresponds to an assummed $R(x) = \sigma_L(x)/\sigma_T(x)$ distribution, $R(x) = 0.1$ ($R(x)$ has the behavior prescribed by QCD.). DO fits various DIS data given by CDHS [39], EMC [40], and SLAC [41] experiments assuming a general parton distribution form: $Ax^a(1-x)^b(1+\alpha x+\beta x^2+\gamma x^3)$ where the parameters contain Q^2 dependence. They provide two sets of structure function which are characterized by $\Lambda_{\rm QCD}$ values 200 MeV and 400 MeV corresponding to two different gluon distributions. MRS essentially follows the DIS data treatment by Devoto, Duke, and Owens, and Roberts [42] same as DO sets. They add high statistics DIS data given by EMC and BCDMS [43] experiments. There is a serious disagreement between EMC and BCDMS experiments. They provide two sets of structure function Set E and Set B which are characterized by $\Lambda_{\rm QCD}$ values 100 MeV and 190 MeV corresponding to two different input distributions from EMC and BCDMS experiments. HMRS is a refined version of MRS parametrization by including data on the prompt photon production [44] and the Drell-Yan process [45]. DFLM analysis used DIS data given by the neutrino DIS experiments, BEBC [46], CCFRR [47], CDHS, and CHARM [48]. They provides three sets of parameters corresponding to fittings of $x\mathcal{F}_3(x,Q^2)$ to all the data and to the BEBC data and to the CHARM data. The data on a light (heavy) tartget Deutrium (Iron) in BEBC (CHARM) experiment gives a hard (soft) $x\mathcal{F}_3(x,Q^2)$ distribution, that is, the higher (lower) in the high x region. MRS and DFLM employ a next-leading order calculation for the Q^2 evolution of the parton densities. Some characteristics of the DIS experiments are given in Table 8.3.

Structure Function		Λ_{QCD}	Q_0^2	$u_v(x)$ and $d_v(x)$ expressions
EHLQ	set 1	200	5	$xu_v(x) = 1.78x^{0.5}(1-x^{1.51})^{3.5}$
				$xd_v(x) = 0.67x^{0.4}(1-x^{1.51})^{4.5}$
	set 2	290	5	$xu_v(x) = 1.78x^{0.5}(1-x^{1.51})^{3.5}$
				$xd_v(x) = 0.67x^{0.4}(1-x^{1.51})^{4.5}$
DO	set 1	200	4	$xu_v(x) + xd_v(x) = 2.345x^{0.419}(1-x)^{3.46}(1+4.40x)$
				$xd_v(x) = 2.776x^{0.763}(1-x)^{4.00}$
	set 2	400	4	$x(x) + xd_v(x) = 1.436x^{0.374}(1-x)^{3.33}(1+6.03x)$
				$xd_v(x) = 2.687x^{0.761}(1-x)^{3.83}$
HMRS	set E	100	4	$xu_v(x) + xd_v(x) = 1.216x^{0.352}(1-x)^{4.08}(1+10.6x)$
				$xd_v(x) = 1.735x^{0.607}(1-x)^{4.83}(1+1.26x)$
	set B	190	4	$xu_v(x) + xd_v(x) = 0.5469x^{0.237}(1-x)^{4.07}(1+23.8x)$
				$xd_v(x) = 0.6957x^{0.426}(1-x)^{4.82}(1+6.32x)$
DFLM	set 1,2,3	300	10	$xu_v(x) = 2.26x^{0.54}(1-x)^{2.52}[1-1.617(1-x)+$
				$3.647(1-x)^2 - 1.998(1-x)^3]$
				$d_v(x)/u_v(x) = 0.57(1-x)$

Table 8.2: Examples of the parametrization in EHLQ, DO, HMRS, and DFLM structure functions. $u_v(x)$ and $d_v(x)$ denotes the parton density functions for valence up-quark and valence down-quark. Λ_{QCD} is in MeV/c and Q_0^2 is in (GeV/c)^2.

Theoretical predictions of the lepton charge asymmetry are calculated using Equation (1.12) and (1.16). The K factor in Equation (1.4) is set to be 1 to obtain charge asymmetry predictions given by the leading order diagram. In the cross section formula (Equation (1.12)), the integration range of pseudo-rapidity is constrained by the experimental transverse-mass threshold (M_{tr}^{th}):

$$\sin\hat{\theta} > \frac{M_{tr}^{th}}{M_W} \tag{8.1}$$

where M_W is the mass of W boson. The asymmetry curves calculated for each structure function are shown in Figure 8.1, where our results are also presented.

DIS experiments	beam	target	x range	Q^2 range
SLAC [41]	e	H,D	$0.03 \leq x \leq 0.9$	$3 \leq Q^2 \leq 30$
EMC [40]	μ	H,D	$0.03 \leq x \leq 0.75$	$7 \leq Q^2 \leq 260$
BCDMS [43]	μ	H,D	$0.06 \leq x \leq 0.80$	$7 \leq Q^2 \leq 170$
CDHS [39]	ν	Fe	$0.015 \leq x \leq 0.65$	$1.1 \leq Q^2 \leq 284$
CHARM [48]	ν	$CaCO_3$	$0.015 \leq x \leq 0.8$	$1.5 \leq Q^2 \leq 80$
BEBC [46]	ν	D	$0.03 \leq x \leq 0.7$	$1.5 \leq Q^2 \leq 55$

Table 8.3: A summary of the beam, target, and probing x-Q^2 range of the deep-inelastic scattering experiments. H, D, Fe, $CaCO_3$ denote hydrogen, deutrium, Iron, and marble plate targets.

Structure function set	χ^2	$P(\chi^2)$
EHLQ1	3.65	0.82
HMRS(B)	3.79	0.80
EHLQ2	5.13	0.64
HMRS(E)	6.05	0.53
DFLM3	6.88	0.44
DFLM2	7.09	0.42
DFLM1	7.41	0.39
DO2	16.4	0.022
DO1	19.9	0.006

Table 8.4: A summary of a chi-square test on various sets of structure functions. The χ^2 quoted is for 7 degrees of freedom.

8.2 Chi-square test

We perform a chi-square test to obtain a preference of the CDF data to existing structure functions. The results are shown in Table 8.4. The probability for a chi-square distribution to take a value greater than the given chi-square values are also shown in Table 8.4. The CDF data prefer EHLQ set 1 and HMRS(B) sets of structure functions, which give the largest asymmetry predictions. All the sets of structure functions except for DO1 and DO2 sets are consistent with the data. Our data exclude DO1 and DO2 structure functions with a confidence level of 90%.

8.3 Higher order effects

In $\bar{p}p$ collisions, W bosons, some of the time, are produced together with QCD jets, which are described by higher order diagrams as shown in Figure 8.2. In the associated production, W bosons are kicked by the QCD radiation, and acquire a transverse momentum, which may change a pseudo-rapidity distribution of the decay leptons. In order to limit ourselves to the W production with a leading order approximation, we selected $W \rightarrow e\nu$ events under the condition that the event is associated with no QCD jet with $E_T > 10$ GeV. Even with this requirement, the W boson production is accompanied with some amount of transverse momentum. The effect of the transverse momentum of Ws is discussed in the following sections.

8.3.1 Method 1

QCD jet activities in the $W \rightarrow e\nu$ production (the underlying event), is measured by the calorimeter. The transverse energy vector of the underlying event ($\vec{E_T}^{UL}$) is calculated as a sum of the missing E_T vector ($\vec{\not{E}_T}$) and the electron E_T vector ($\vec{E_T}^{e}$):

$$\vec{E_T}^{UL} = -(\vec{\not{E}_T} + \vec{E_T}^{e}). \tag{8.2}$$

The transverse momentum of W is defined:

$$\vec{p_T}^{W} = -\vec{E_T}^{UL}. \tag{8.3}$$

A transverse energy distribution of the underlying event is shown in Figure 8.3. The energy scale of the underlying events suffers a correction of a factor 1.4 as a result of the non-linear behavior of the calorimeter response against low p_T hadrons. Parallel and perpendicular components of the transverse energy of the underlying event with

respect to the electron direction in the transverse plane are shown in Figure 8.4. No significant correlation between the directions of the underlying event and the electron is found.

We simulate the underlying event using a transverse energy distribution obtained from the data. A transverse energy of the underlying events is generated in accordance with the distribution shown in Figure 8.3. The azimuthal direction of the underlying event is randomly generated between $0 < \theta < 2\pi$. The $W \rightarrow e\nu$ events are generated by the Fast Monte Carlo [33, 34], the Monte Carlo simulation which generates W bosons from the leading order diagram $q\bar{q} \rightarrow W$ using a variety of proton structure functions and simple parameterizations of the W boson p_{T}. The W-rest frame is boosted into the opposite direction of the underlying event with the same size of the transverse momentum as the underlying event. The decay electrons from W decays are Lorentz boosted back into the W-rest frame. The asymmetry values are compared before and after the smearing due to the underlying event.

The results are shown in Figure 8.5, where the difference of the asymmetry values before and after the smearing is plotted against the un-smeared asymmetry values for various sets of structure function. The effect of the underlying event on the electron pseudo-rapidity distribution is shown in Figure 8.6. For the $W^+ \rightarrow e^+\nu$ ($W^- \rightarrow e^-\nu$), the number of the postron (electron) in the forward (backward) region slightly decrease while the number of the postron (electron) in the backward (forward) region slightly increase. The asymmetry value becomes small as the result, that is, the observed asymmetry value is slightly smaller than the real value. The size of the asymmetry is reduced by about $0.1A$ with respect to the true asymmetry A of the leading order calculation

8.3.2 Method 2

Monte Carlo simulations including the next-to-leading order (i.e. order-α_s) calculation are available. The next-to-leading order calculation generates one parton jet in the final state. Applying the transverse momentum threshold on the parton jet, the effect of the W transverse momentum on the lepton charge asymmetry measurement is calculated [49].

The W events accompanied with no parton jet and one parton jet are generated by Papageno Monte Carlo [51]. For the W event with one parton jet, we apply various momentum thresholds of 0 to 20 GeV on the parton jet. Figure 8.7 shows the lepton charge asymmetry integrated over $|\eta| < 1.0$ for the various transverse momentum threshold of the parton jet. With the transverse momentum threshold of the parton jet. The lepton charge asymmetry integrated over $|\eta| < 2.5$ become larger by 0.02 at the transverse momentum threshold of parton jets of 10 GeV for the structure functions available in the Monte Carlo, which are EHLQ1, MRS1, DO1 sets of proton structure functions.

8.3.3 Next-to-leading order calculation

Recently the next-to-leading order calculation with experimental cuts has been presented by H. Bear and H. Reno in [52]. The effect on the lepton asymmetry is also described in the article. The calculation includes the process of $p\bar{p} \rightarrow W^+X \rightarrow e^+\nu X$, where X is the associated parton jet given by the next-to-leading order diagrams (see Figure 8.2). It has been successfully performed by setting the finite energy cut off on the final partons. The W-boson cross section calculated with this method is almost independent of the parton energy cut-off. The kinematical cuts of the W identification used in CDF are applied on the calculation of lepton charge asymmetry. The result is shown in Figure 8.8. The inclusion of the next-to-leading order diagram reduces the

lepton asymmetry by about 0.02 at $\eta = 1.0$.

8.3.4 Summary of the higher order effects

The result of the next-to-leading order calculation in Section 8.3.3 is consistent with the Fast Monte Carlo result based on the underlying event measurement described in Section 8.3.2. According to these methods, the lepton charge asymmetry suffers a correction of about $+0.1A$, 10% of the observed asymmetry. On the other hand, the Monte Carlo study described in Section 8.3.1 gives almost no correction in the central region ($|\eta| < 1.0$) and $-0.1A$ correction in the plug region. We conclude that unknown kinematics in the W-boson production, such as the transverse motion of Ws and the parton jet activity, introduce a theoretical uncertainty of $\pm 0.1A$, $\pm 10\%$ of the observed asymmetry.

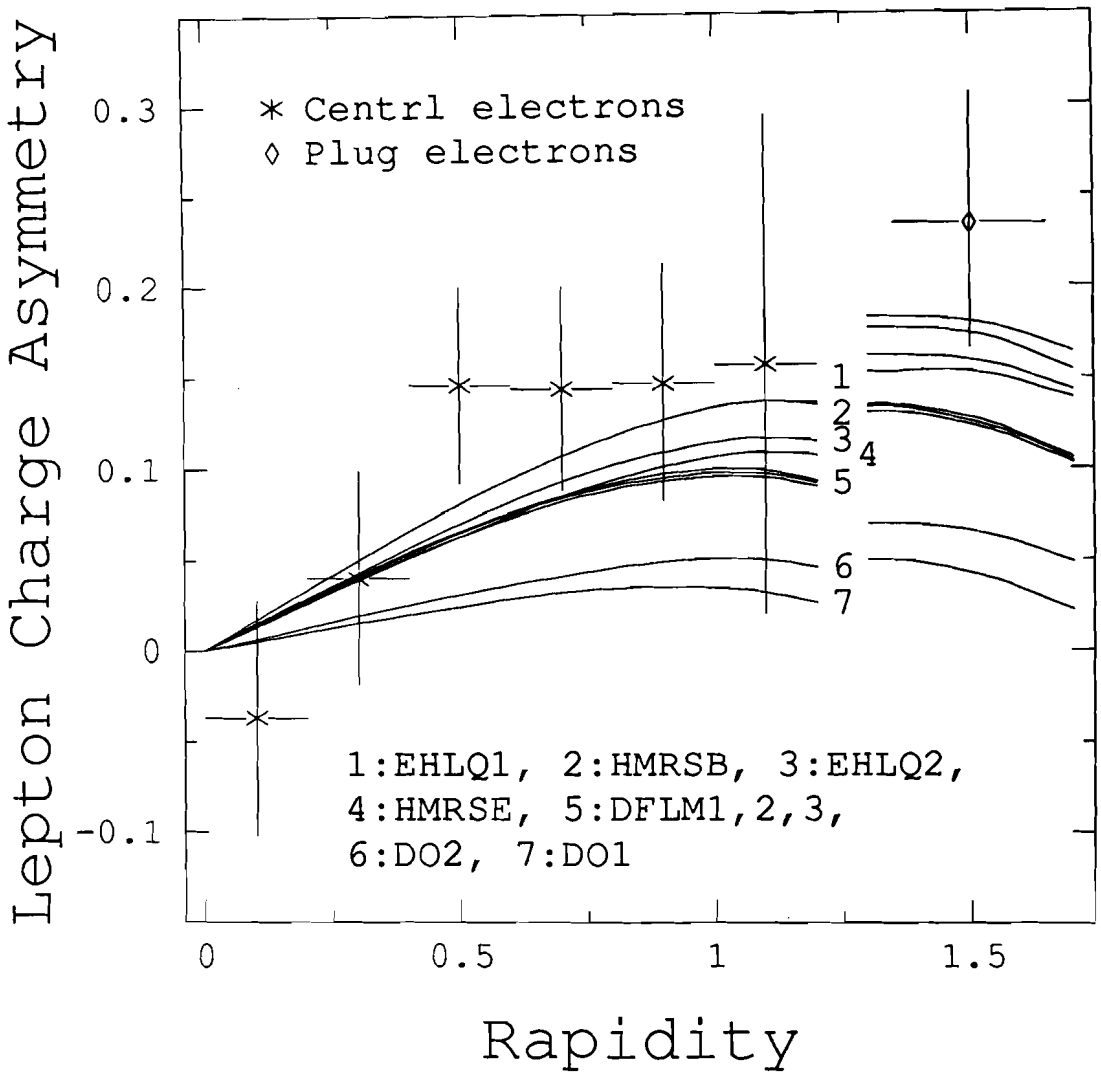

Figure 8.1: Lepton charge asymmetry distribution. The transverse mass thresholds are 50 GeV/c^2 for the central points and 60 GeV/c^2 for the plug point. The predictions from various sets of structure functions are overlaid.

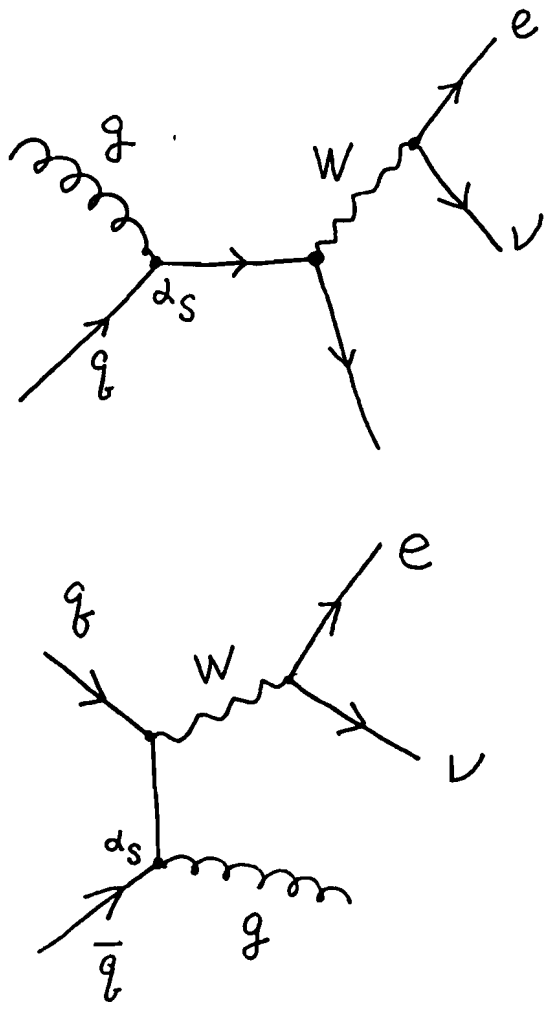

Figure 8.2: Next-to-leading order diagrams for the W boson production.

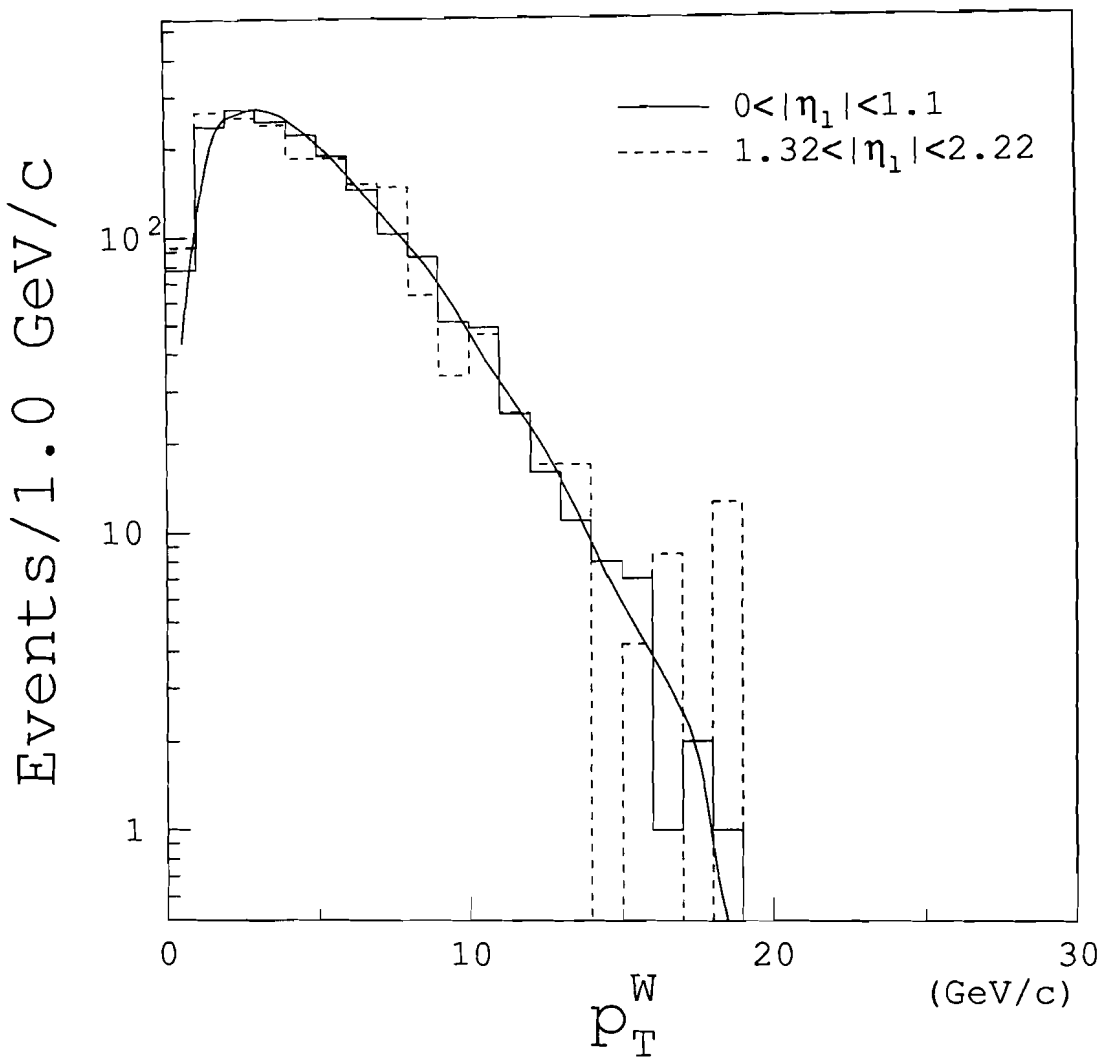

Figure 8.3: Distributions of the transverse momentum of the underlying events. The solid line is for the central Ws and the dashed line is for the plug Ws. The events are required to be associated with no QCD jet of $E_T > 10$ GeV. The size of the transverse momentum is un-corrected.

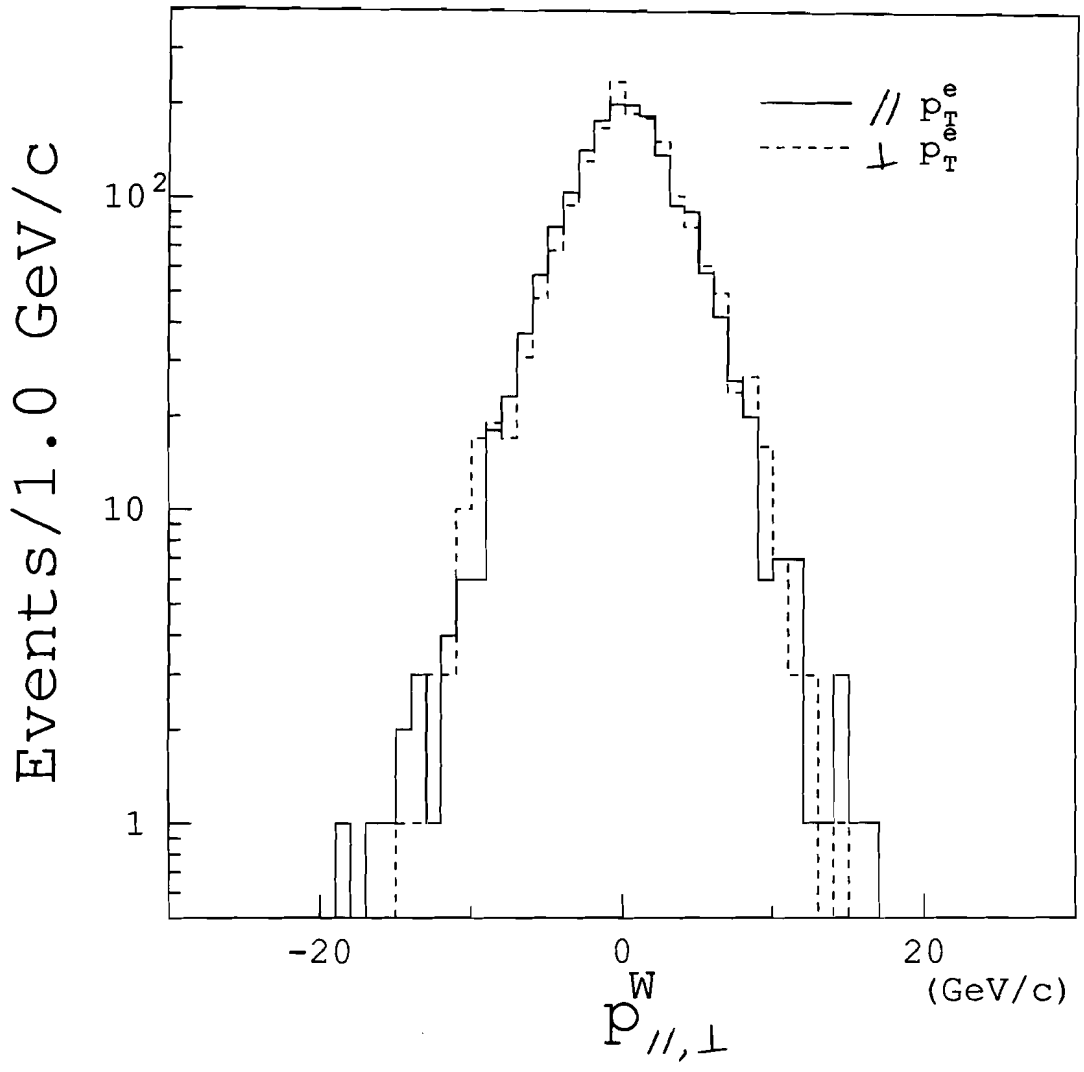

Figure 8.4: The parallel (solid) and perpendicular (dashed) components of the transverse momentum of the underlying events with respect to the electron direction. The size of the transverse momentum is un-corrected.

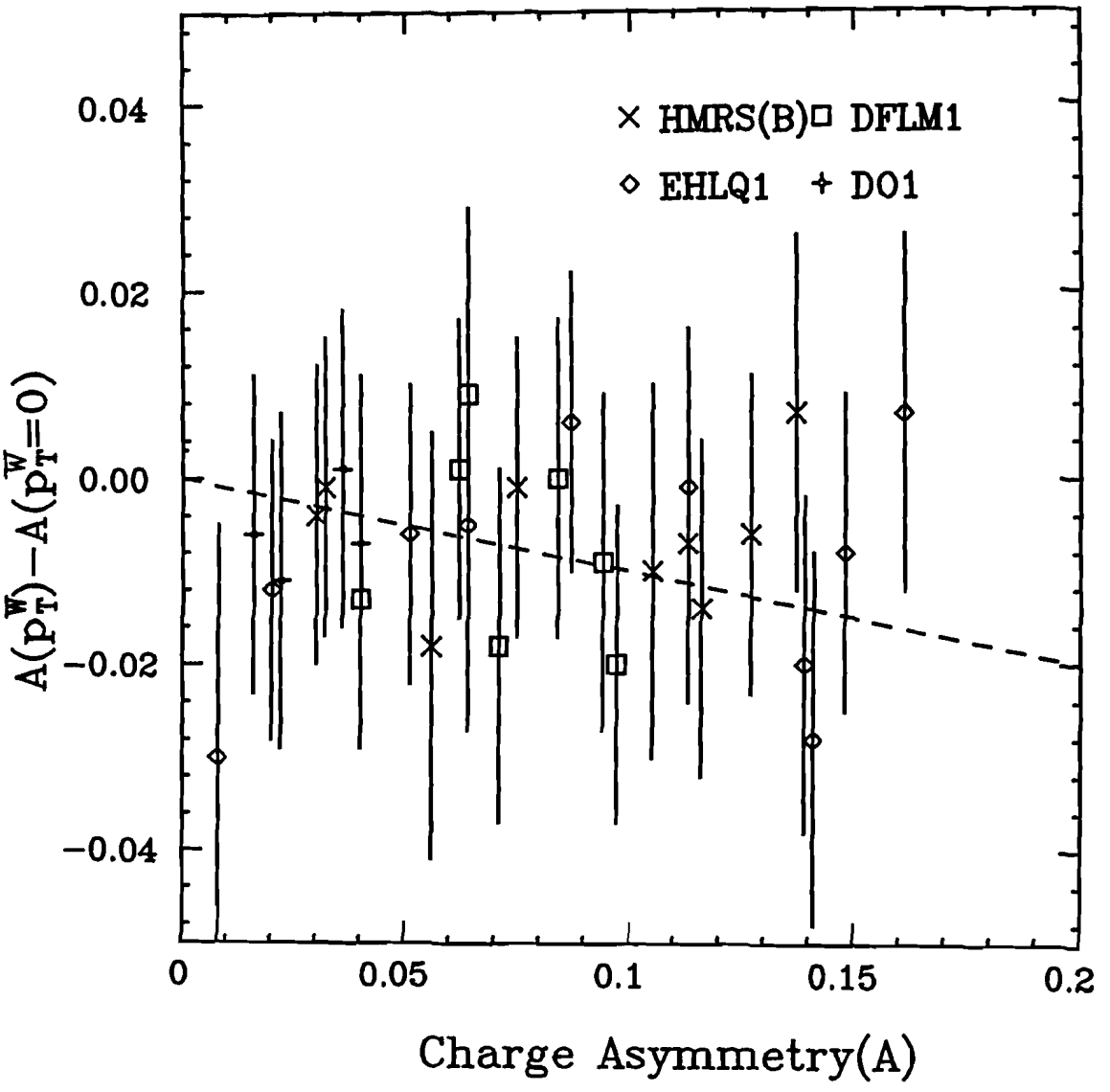

Figure 8.5: The effect of the underlying events on the lepton charge asymmetry. The differences of the asymmetry values before and after the smearing are plotted against the un-smeared asymmetry values The dashed line shows -10% difference of the un-smeared asymmetry value ($0.1A$).

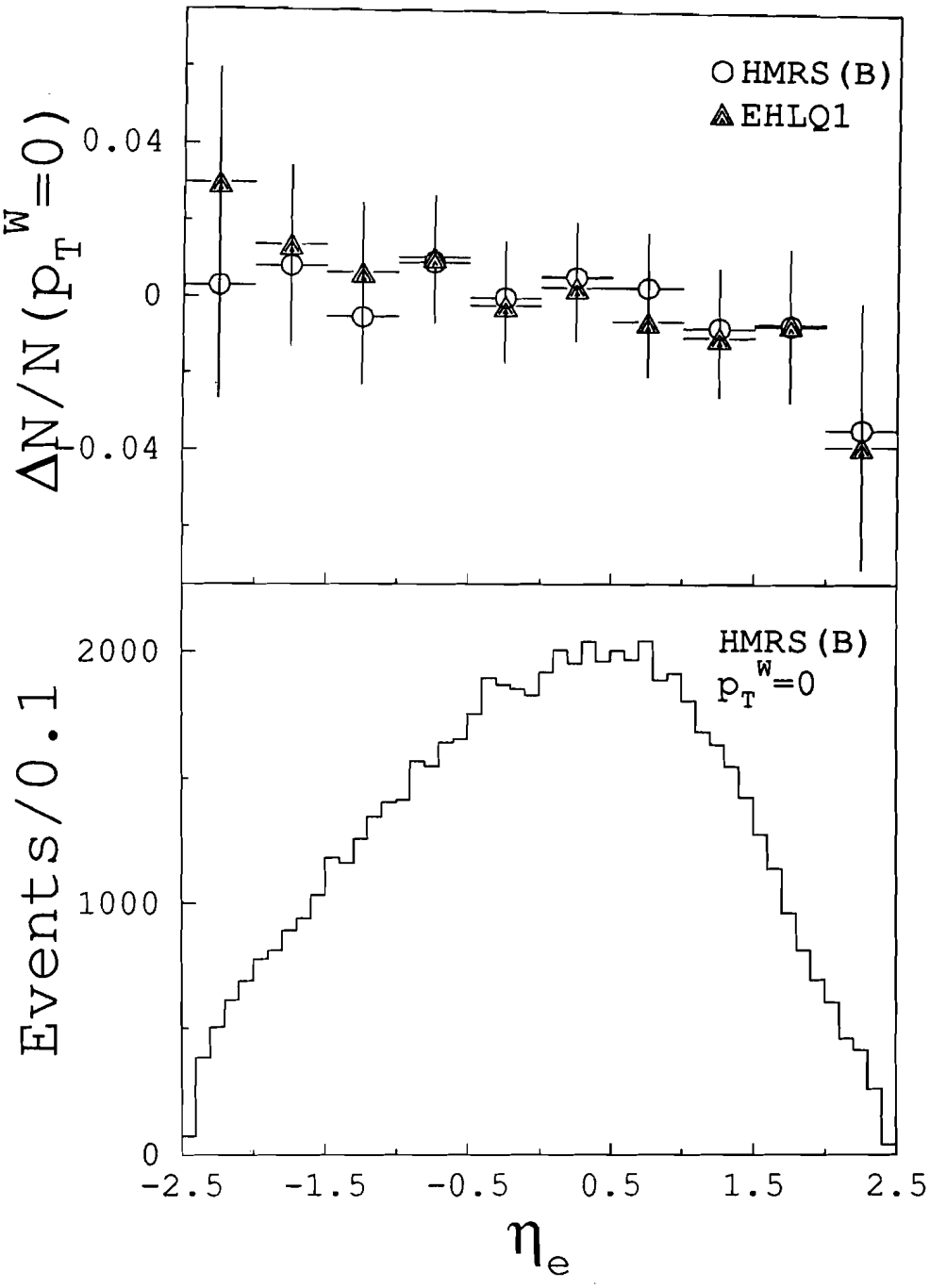

Figure 8.6: An effect of the underlying events on the electron pseudo-rapidity distribution. Fast Monte Carlo generates 100k $W^+ \to e^+\nu$ events for HMRS(B) and EHLQ1 sets of structure functions. The difference before and after the undelying event smearing is taken as $\Delta N \equiv N(p_T^W) - N(p_T^W = 0)$. The electron pseudo-rapidity distribution is shown for HMRS(B) set structure function without the underlying event smearing.

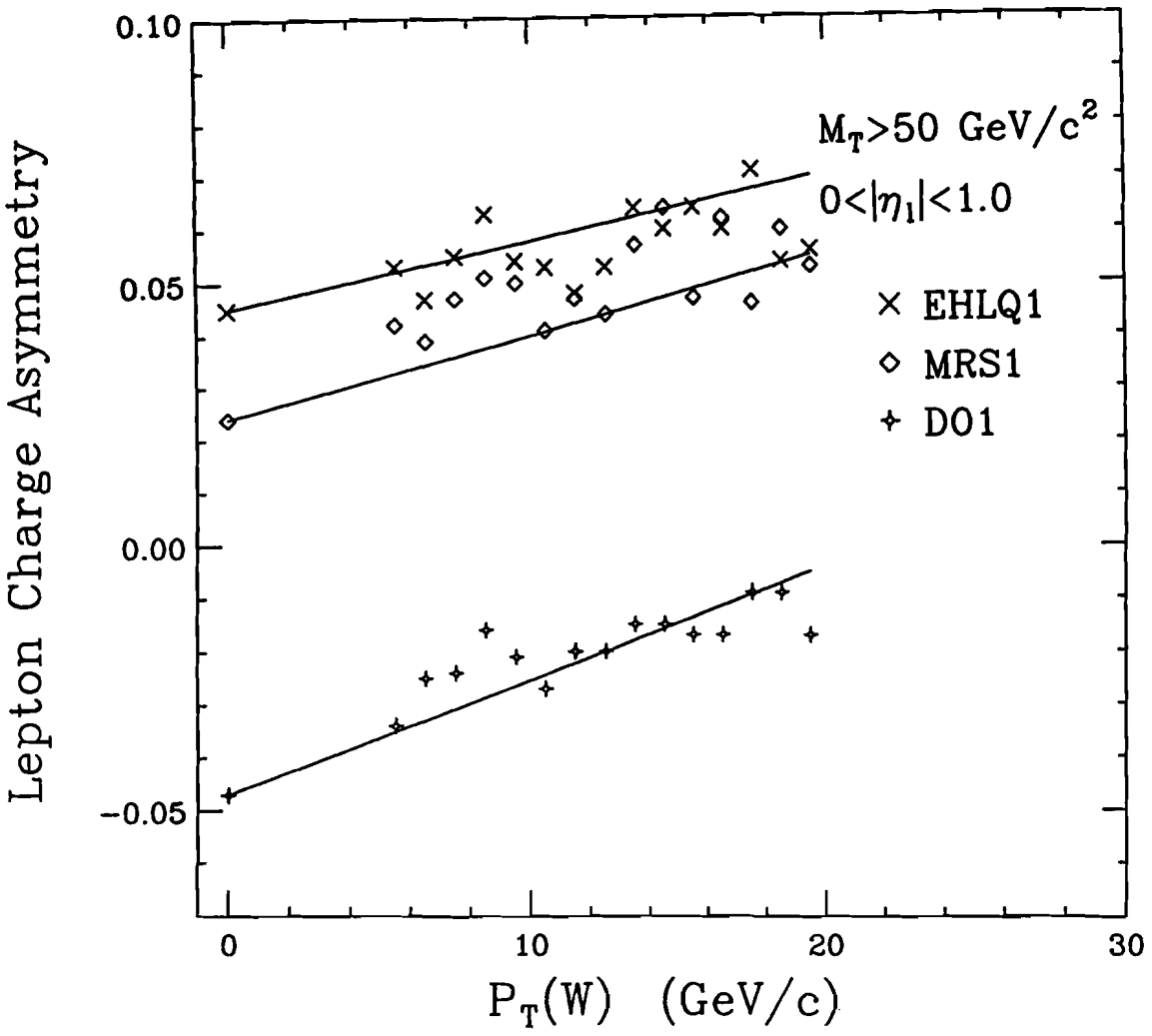

Figure 8.7: A predicted effect of the parton jet on lepton charge asymmetry by Papageno Monte Carlo.

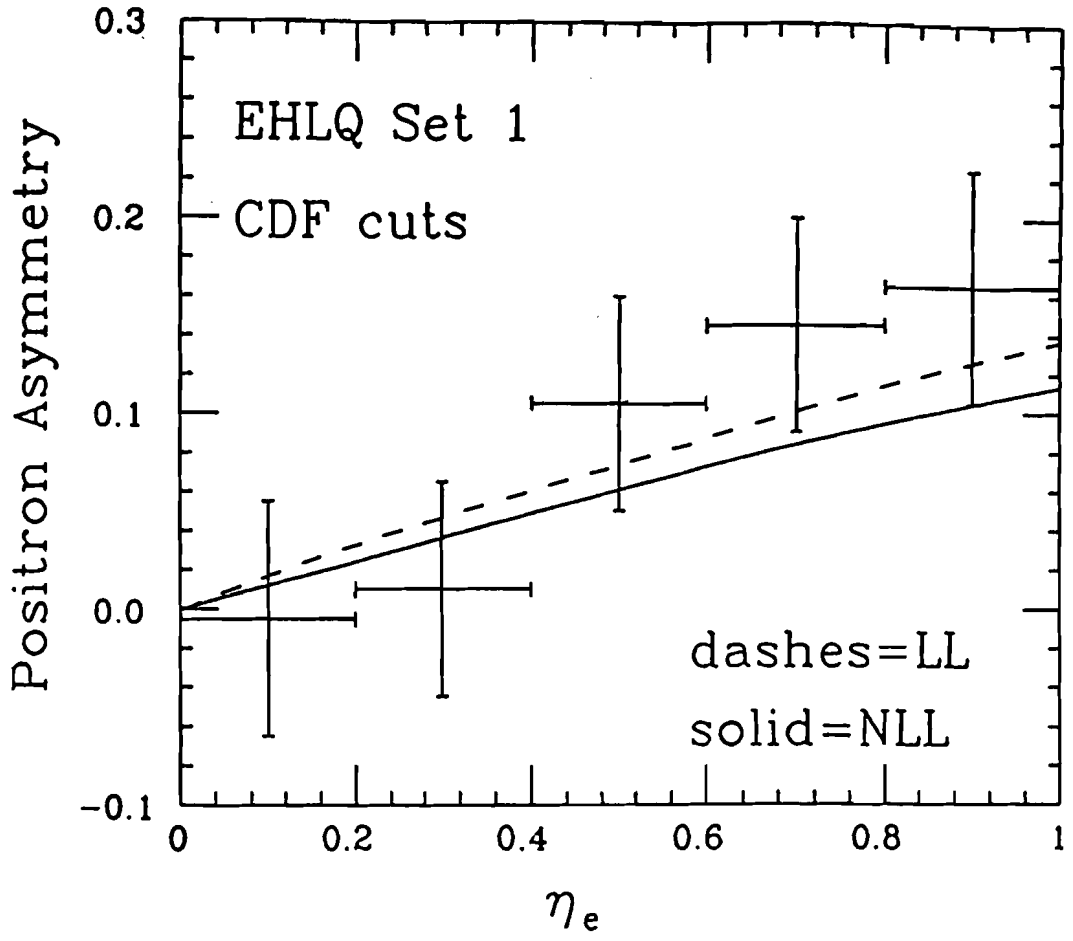

Figure 8.8: A predicted distribution of lepton charge asymmetry as a function of lepton pseudo-rapidity at next-to-leading order calculation. The plot is reproduced from Reference [52] by H. Bear and M. H. Reno. The CDF preliminary result [53] is shown for comparison.

Chapter 9

Conclusions

We have measured electron-positron charge asymmetry in the sample of $W \rightarrow e\nu$ events from 1.8 TeV proton-antiproton collisions. The charge asymmetry measurement allows us to probe the proton structure in the region of $0.01 < x < 0.2$ correcponding to the electron pseudo-rapidity range $|\eta_e| < 1.7$ and $Q^2 \sim M_W^2$. The lepton charge asymmetry is expected as a combined result of the V–A left-handed coupling and the W rapidity distribution. This indirect measurement of the W rapidity distribution has a sesitivity to the ratio $d(x, Q^2)/u(x, Q^2)$.

The $W \rightarrow e\nu$ events were subdivided into the central ($|\eta_e| < 1.1$) and plug ($1.3 < |\eta_e| < 1.7$) samples. The charge asymmetry was measured in the central and plug W samples. Our charge asymmetry measurement showed consistency with predictions of many of the available parton distribution sets (EHLQ, HMRS, DFLM), particularly those which use recent data from deep inelastic experiments (HMRS, DFLM). DO set of structure function was ruled out at a confidence level of 90%.

Various systematics were studied, which are the electron identification efficiency, the trigger efficiency, the track finding efficiency, the background contaminations, and the charge misidentification probability. Our charge asymmetry measurement was almost free from these systematic uncertainties. Higher order effect was found to be small

enough relative to the statistical uncertainties.

Bibliography

[1] G. Altarelli *et. al.*, Nucl. Phys. B246 (1984) 12.
C. Rubbia, Rev. Mod. Phys. 57 (1985) 699.

[2] CDF collaboration, Phys. Rev. D43 (1990) 2070.

[3] CDF collaboration, Phys. Rev. Lett. 63 (1989) 720.

[4] CDF collaboration, Phys. Rev. Lett. 67 (1991) 1502.

[5] UA2 collaboration, Phys. Lett. B241 (1990) 150.

[6] MARKII Collabolation, G. S. Adrams, *et. al.*, Phys. Rev. Lett. 63 (1989) 2173.
ALEPH Collabolation, P. Decamp, *et. al.*, Phys. Lett. B235 (1990) 399.
DELPHI Collabolation, P. Aarnio, *et. al.*, to be published on Phys. Lett. , CERN-EP/90-32.
L3 Collabolation, B. Adeva, *et. al.*, Phys. Lett. B237 (1990) 136.
OPAL Collabolation, M. Z. Akrawy, *et. al.*, to be published on Phys. Lett. , CERN-EP/90-27.

[7] E. L. Berger, MAD/PH/400, ANL-HEP-PR-88-12.

[8] E. L. Berger, F. Halzen, C. S. Kim, and S. Willenbrock, Phys. Rev. D40 (1989) 83.
A. D. Martin, R. G. Roberts, and W. J. Stirling, Mod. Phys. Lett. A4 (1989) 1135.

[9] C. S. Wu *et al.*, Phys. Rev. 105 (1957) 1413.
H. Frauenfelder *et al.*, Phys. Rev. 106 (1957) 386.

[10] TRIUMF collaboration, B. Blake *et al.*, Phys. Rev. D37 (1988) 587.

[11] UA2 collaboration, Phys. Lett. B194 (1987) 158.

[12] G. Appolinari *et. al.*, *A measurement of the $\bar{p}p$ total cross section at $\sqrt{s}$=1800 GeV*, CDF internal note 1438 (1991).

[13] E. L. Berger, F. Halzen, C. S. Kim, and S. Willenbrock, Phys. Rev. D40 (1989) 83.

[14] CDF collaboration, Nucl. Instrum. and Methods A271 (1988) 387.

[15] F. Snider *et. al.*, Nucl. Instrum. and Methods A268 (1988) 75.

[16] F. Bedeschi *et. al.*, Nucl. Instrum. and Methods A268 (1988) 50.

[17] G. Drake *et. al.*, Nucl. Instrum. and Methods A269 (1988) 68.

[18] L. Balka *et. al.*, Nucl. Instrum. and Methods A267 (1988) 272.

[19] G. Apollinari *et. al.*, Nucl. Instrum. and Methods A267 (1988) 301.

[20] Y. Fukui *et. al.*, Nucl. Instrum. and Methods A267 (1988) 280.

[21] G. Brandenburg *et. al.*, Nucl. Instrum. and Methods A267 (1988) 257.

[22] S. Chihanger *et. al.*, Nucl. Instrum. and Methods A267 (1988) 249.

[23] G. Ascoll *et. al.*, Nucl. Instrum. and Methods A268 (1988) 33.

[24] G. Ascoll *et. al.*, Nucl. Instrum. and Methods A269 (1988) 63.

[25] G. W. Foster *et. al.*, Nucl. Instrum. and Methods A269 (1988) 51.

[26] D. Amidei *et. al.*, Nucl. Instrum. and Methods A269 (1988) 51.

[27] E. Barsotti et .al., Nucl. Instrum. and Methods A269 (1988) 82.

[28] Y. Hayashide, *Characteristics of CDF Endplug electromagnetic calorimeter*, Ph. D thesis, UTPP_26 (1986).

[29] Particle Data Group, J. J. Hernández *et al.* Phys. Lett. B239 (1990) 1.

[30] K. Yasuoka *et. al.*, Nucl. Instrum. and Methods A267 (1988) 315.

[31] F. Paige and S. D. Protopescu, *Isajet Monte Carlo* , BNL 38034 (1986).

[32] J. Freeman, *Guide to the CDF Detector Simulation* Online Documentation, `C$DOC:SIMGUIDE.MEM`.
T. Kamon, Y. Hayashide, J. Freeman, CDF internal note 287 (1985).
Proceedings for the Workshop on Detector Simulation for the SSC, edited by L. E. Price, ANL-HEP-CP-88-51, Argonne National Laboratory (1987), p. 190.

[33] CDF collaboration, Phys. Rev. Lett. 64 (1990) 152.

[34] C. Campagnari, *A fast W and Z Monte Carlo* , CDF internal note 1025.

[35] E. Eichten, I. Hinchliffe, K. Lane, and C. Quigg Rev. Mod. Phys. 56 (1984) 579.

[36] D. Duke and J. F. Owens, Phys. Rev. D30 (1984) 49.

[37] P. N. Harriman, A. D. Martin, W. J. Stirlling, and R. G. Roberts, Phys. Rev. D42 (1990) 798.

[38] M. Diemoz, F. Ferroni, E. Longo, and G. Martinelli, Z. Phys. C39 (1988) 21.

[39] H. Abramowicz *et. al.*, Z. Phys. C 17 (1983) 283.

[40] J. J. Aubert *et. al.*, Nucl. Phys. B105 (1981) 315.
J. J. Aubert *et. al.*, Nucl. Phys. B259 (1985) 189.

[41] A. Bodek *et. al.*, Phys. Rev. D20 (1979) 1471.

[42] A. Devoto, D. W. Duke, J. F. Owens, and R. G. Roberts, Phys. Rev. D27 (1983) 508.

[43] A. C. Benvenuti *et. al.*, Phys. Lett. B223 (1989) 485.

[44] M. Bonesini *et. al.*, Z. Phys. C 38 (1988) 371.

[45] C. N. Brown *et. al.*, Phys. Rev. Lett. 63 (1989) 2637.

[46] D. Allasia *et. al.*, Z. Phys. C 28 (1985) 321.

[47] D. B. MacFarlane *et. al.*, Fermilab-Pub-83/108-Exp (1983).

[48] F. Bergsma *et. al.*, Z. Phys. Lett. 123B (1983) 269.

[49] S. Leone, *Lepton Charge Asymmetry from $W^{\pm} \rightarrow \ell^{\pm}\nu$ at the Tevatron Collider*, Ph. D thesis, INFN PI/AE 90/7 (1990).

[50] Y. Hayashide, *Characteristics of CDF Endplug electromagnetic calorimeter*, Ph. D thesis, UTPP_26 (1986).

[51] I. Hinchliffe, Private communication (1989).

[52] H. Baer and M. H. Reno, Phys. Rev. D43 (1991) 2892.

[53] CDF Collaboration, J. Hauser, in *Proceedings of the Workshop on Hadron Structure Functions and Parton Distributions*, Batavia, Illinois, 1990 edited by D. F. Geesaman, J. Morfin, C. Sazama, and W. K. Tung (World Scientific, Singapore, 1990).

Appendix

A.1 Dead layers and the quadrant gain constants in the plug

Dead layers in the plug calorimeter are surveyed and tabulated in Table A.1. Visible

Quadrant (no.)	dead plane no. (0-33)	a	b	$a \times b$
TSW (0)	27	$1.023 \pm .017 \pm .010$	1.016302	1.040
TNW (1)	1,8,17	$1.099 \pm .017 \pm .003$	1.105412	1.215
BSW (2)		$1.148 \pm .016 \pm .007$	1.000000	1.148
BNW (3)	11,15,16	$1.088 \pm .017 \pm .006$	1.184175	1.288
TSE (4)	31	$0.957 \pm .019 \pm .005$	1.008512	0.965
TNE (5)	30	1	1.010183	1.010
BSE (6)		$1.015 \pm .018 \pm .010$	1.000000	1.015
BNE (7)	33	$1.053 \pm .016 \pm .007$	1.049847	1.105

T : Top, B : Bottom, S : South, N : North, W : West, E : East
a: Quadrant gain constant
b: Dead layer correction factor

Table A.1: Dead planes and the quadrant gain constants in the plug calorimeter during 1988-89 run .

energy loss in the dead layers are calculated and corrected, as described in Section 5.1.3. The dead-layer correction factors found in Table A.1 are based on 50 GeV pion shower in the test beam. The calorimeter tower energy is corrected by those factors in order to make corrections on the missing transverse energy and the jet energy. The electron energy is corrected by a factor based on the electron shower profile. The quadrant gain constants are also given in Table A.1.

A.2 Dead channels in the plug

There were 16 dead channels which has been dead during the 1988-1989 run. These channels are listed in Table A.2. Calorimeter towers are numbered from 0 to 71 in

	1	2	3	4	5	6	7	8	9	10	11	12	13	14	15	16
West/East	W	W	W	W	E	E	E	E	E	E	E	E	E	E	E	E
$\#\phi$	15	17	59	69	0	24	24	26	30	30	31	31	32	32	32	35
$\#\eta$	1	13	9	0	2	13	9	3	0	1	0	1	0	1	1	3

Table A.2: A summary of dead channels in the plug calorimeter during the 1988-1989 run.

azimuth where the 0th tower is at the azimuthal angle of 0°, and from 0 to 13 in pseuodo-rapidity where the 0th tower is at the outermost annuli. Note that ten dead channels out of sixteen are located out of the fiducial region ($1.32 < |\eta| < 2.22$) so that the effect on the electron measurement in the plug region is very small.

A.3 A study of the CTC track reconstruction efficiency in the plug region

The CTC tracks in the plug region pass through three or four innermost super-layers. Density of tracks is higher in the inner region than in the outer region. This makes the track reconstruction in the plug region rather difficult.

Two versions of track finding algorithms are tested on the plug W sample. The sample was selected from the *Spin Cycle* data set. The selection criteria are shown in Table 5.5. We find 340 candidates in the pre-selected sample without the CTC track requirements, E/p, $\Delta\phi$ and ΔR. This sample contains 2.4% background from QCD jets and heavy flavour, as described in Section 6.1.3. Both versions of track finding algorithms individually find the CTC track associated with an electron for 239

1st version

	+	−
West	48	55
East	91	45

2nd version

	+	−
West	48	54
East	90	47

Table A.3: Charge distributions of the tracks reconstructed by two versions of track finding algorithm.

Combined sample of two versions

	+	−
West	50	60
East	101	51

Total 262 candidates

Table A.4: A charge distribution for the combined sample of two versions of track finding algorithm.

candidates. Then the CTC track finding efficiency is given by

$$\epsilon_{PLUG}^{CTC} = \frac{239}{340} = (70.3 \pm 2.5)\%. \tag{A.3-1}$$

Charge distributions of the tracks for the two versions of track finding algorithm are shown in Table A.3. For 216 candidates out of 239, the CTC track is found by both versions of track finding algorithm. Each version has 23 candidates whose electron track is not found by another version. Out of the 23 tracks, 18 tracks in the first algorithm were also reconstructed by the second algorithm. They gave relatively worse E/p values than the first version, but none of them flipped their charge. We combined those samples into one sample. The charge distribution for the combined sample is shown in Table A.4. The track finding efficiency now becomes

$$\epsilon_{PLUG}^{CTC} = \frac{262}{340} = 77.1 \pm 2.3\%. \tag{A.3-2}$$

On the remaining 78 candidates, a manual track reconstruction on screen was applied through the following procedure. For a given electron cluster position, the expected hits on the axial and stereo super-layers were examined by the eyes. The tracks for the plug electrons were mostly found as two-dimensional (2D) R-ϕ tracks. In this case, the possible stereo hits were added by hand. The three-dimensinal (3D) track was then reconstructed. The scanning results are summarized as follows.

Table A.5: A summary of the hand scanning of the unreconstructed electron tracks

1. Silver: Good quality tracks

   - A 3D track was found automatically, but the position matching with the cluster was bad.
   - A track was found as a 2D track and manually reconstructed in 3D.
   - A track was full manually reconstructed with clear axial and stereo wire hits.

	+	−
West	6	7
East	11	7

31 events

2. Bronze: Low quality tracks

   - A 2D track was found, but the stereo hits were slightly ambiguous.
   - A track was full manually reconstructed, but a part of the hits were obscured by neighboring tracks.

- A track showed bad R_{exit} matching caused by a poor stereo-wire information.

	+	−
West	3	3
East	3	3

12 events

3. Track reconstruction error

   - A row of wire hits pointing to the cluster was visible but the track reconstruction failed.

24 events

4. Complex (Background?)

   - Very dense CTC hits.
   - Wire hits were wiped out by nearby tracks.

6 events

5. Background candidates

   - No visible wire hit was pointing to the cluster.

4 events

6. No bank of the CTC wire hits

1 event

---

78 events

Adding the silver and bronze quality tracks in Table A.5, the track finding efficiency increases to

$$\epsilon_{PLUG}^{CTC} = \frac{239 + 23 + 31 + 12}{340 - 11} = \frac{305}{329} = 92.7 \pm 1.4\%. \tag{A.3-3}$$

The background level can also be estimated from this result:

$$f_{BG} = \frac{10}{340 - 1} = 3.0 \pm 1.4\%. \tag{A.3-4}$$

This value is consistent with an independent estimation of $(2.4 \pm 1.3)\%$ described in Section 6.1. We note that the silver and bronze quality tracks show a similar charge distribution as the combined sample in Table A.4. There is no evidence that the track finding algorithm has a charge dependence.